

Temperature and strain dependence of the magnetic properties of multilayers with interfacial DMI



Khulaif Alshammari

School of Physics and Astronomy

University of Leeds

Submitted in accordance with the requirements for the degree of

Doctor of Philosophy

February 2022

This thesis is dedicated to my parents and my wife.

Intellectual Property Statement

The candidate confirms that the work submitted is his own, except where work which has formed part of jointly authored publications has been included. The contribution of the candidate and the other authors to this work has been explicitly indicated below. The candidate confirms that appropriate credit has been given within the thesis where reference has been made to the work of others.

This copy has been supplied on the understanding that it is copyright material and that no quotation from the thesis may be published without proper acknowledgement.

The right of Khulaif Alshammari to be identified as Author of this work has been asserted by him in accordance with the Copyright, Designs and Patents Act 1988.

©2021 The University of Leeds and Khulaif Alshammari.

Work from the following jointly authored publication is presented in chapter five of this thesis:

Khulaif Alshammari, Eloi Haltz, Mohammed Alyami, Mannan Ali, Christopher H. Marrows, Joseph Barker, and Thomas A. Moore. "Scaling of the Dzyaloshinskii-Moriya interaction with magnetization in Pt/Co(Fe)B/Ir multilayers." *Phys.Rev. B*.104,224402 (2021).

Acknowledgements

My heartfelt appreciation goes to Dr. Thomas Moore, my supervisor, for his helpful insights, suggestions, and careful attention to detail. Without his vast knowledge and guidance in experimental physics, this research would not have been possible. His exceptional scientific skills, extraordinary compassion, and leadership helped me throughout the research process. Thank you for always being willing to discuss issues with me and allowing me the flexibility to do my own research and explore my ideas. I just do not have the words to express my sincere thanks and respect.

My thanks also go to Dr. Gavin Burnell, my co-supervisor, for his insightful words and encouragement. Special thanks to Dr. Mannan Ali for his help, training me in the lab and teaching me on a variety of the experimental techniques I've utilised. Thanks also to Dr. Joseph Barker who has been very helpful with my work, from helping me in learning Python to assisting me with continuing discussion of my work. Prof. Bryan Hickey, Prof. Chris Marrows, Dr. Oscar Cepedes, and Dr. Satoshi Sasaki, as well as the rest of the academic staff, deserve particular appreciation for their support and encouragement throughout many productive discussions during Friday meeting and forum talk.

During the early years of my PhD, I was fortunate to gain from Dr. Rowan Temple, Philippa Shepley, Dr. Risalat Khan, Dr. Adam Wells, Dr. George Stefanou, Dr. Luis Benito, and Dr. Mohammed Alyami. I would also like to thank Dr. Satam Alotibi, Dr. Kathryn Moran, Dr. Matthew Vaughan, and Alistair Walton for their help and cooperation during my PhD.

Also, I am grateful to the members of the cryogenic team, both past and present, for their continuous efforts to keep everything cool. Every member of the mechanical workshop has helped me at one time or another, and they have always done it cheerfully. Additionally, I'd want to express my gratitude to the electronics workshop, which has been very beneficial in my profession and in addressing problems. It's been a pleasure to work with the CM group, numerous

wonderful colleagues and students, who contribute to the group's interesting and friendly atmosphere.

Thank you to Jouf University in particular for their financial support and for giving me the opportunity to study in the United Kingdom.

Finally, I want to express my gratitude to my parents, my wife, and my beautiful children, as well as to my sisters and brothers, for their constant support and encouragement.

Abstract

Magnetic multilayers with perpendicular anisotropy and an interfacial Dzyaloshinskii-Moriya interaction contain chiral domain walls and skyrmions that are promising for applications. Here we measure the temperature dependence of the Dzyaloshinskii-Moriya interaction (DMI) in Pt/CoFeB/Ir and Pt/CoB/Ir multilayers by means of static domain imaging. First, the temperature dependences of saturation magnetisation (M_S), exchange stiffness (A) and intrinsic perpendicular anisotropy (K_u) are determined independently, and scaling laws for K_u and D with the magnetisation are established. We then image the demagnetised domain pattern in each multilayer by wide-field Kerr microscopy in the temperature range 9-290 K. We calculate the DMI constant D from an analytical expression for the domain wall energy density that treats the multilayer as a uniform medium.

Also, we measure the temperature dependence of the DMI and observe the domain pattern in Pt/CoFeB/Ir and Pt/CoB/Ir multilayers deposited on barium titanate, BaTiO₃, (BTO). At room temperature, stripe domains in the Pt/CoFeB/Ir film are tilted along the length of the BTO a-domains, perpendicular to the in-plane tensile strain. The BTO undergoes structural phase transitions at ~ 180 K and ~ 270 K and these introduce further in-plane strain which we deduce to be responsible for increasing the domain width in the Pt/CoFeB/Ir, as the temperature is increased over the range 13-320 K.

The magnetic anisotropy field ($\mu_0 H_k$) of Pt/CoFeB/Ir and Pt/CoB/Ir multilayers is measured under application of strain. The samples are grown on glass substrates and glued to biaxial piezoelectric transducers. A method based on the extraordinary Hall effect (EHE) is used

to measure the magnetic anisotropy field. The strain effects on the anisotropy field, through coupling the films to the piezoelectric transducers, is described and the magnetostriction constant subsequently is measured.

Abbreviations

STT	Spin transfer torque
MTJ	Magnetic tunnel junction
MRAM	Magnetic random access memory
DWs	Domain walls
DC	Direct current
PMA	Perpendicular magnetic anisotropy
HDD	Hard disk drives
BTO	Barium titanate
PMN-PT	Lead magnesium niobate-lead titanate
PZT	Lead zirconate titanate
RF	Radio frequency
DMI	Dzyaloshinskii-Moriya interaction
XMCD	X-ray magnetic circular dichroism
Ta	Tantalum
Ir	Iridium
Co	Cobalt
CoFeB	Cobalt-Iron-Boron
CoB	Cobalt-Boron
Pt	Platinum
IP	In-plane
OOP	Out-of-plane
SiO _x	Silicon oxide
SOC	Spin-orbit interaction
EHE	Extraordinary Hall effect
MR	X-ray magnetic circular dichroism
MR	Magnetoresistance
RGA	Residual Gas Analyser
XRR	X-ray reflectivity
MOKE	Magneto-Optical Kerr Effect
SQUID	Superconducting quantum interference device

Contents

1	Introduction	1
1.1	Thesis overview	4
2	Theoretical Background	5
2.1	Introduction	6
2.2	Magnetic anisotropy	6
2.2.1	Magnetocrystalline anisotropy	6
2.2.2	Shape anisotropy	7
2.2.3	Magnetoelastic anisotropy	8
2.3	Stoner-Wohlfarth model	10
2.4	Perpendicular Magnetic Anisotropy	11
2.5	Magnetic domain wall	11
2.5.1	Equilibrium domain pattern	13
2.6	Magnons	15
2.7	Dzyaloshinskii-Moriya interaction	18
2.8	Multiferroics	19
2.9	Strain Mediated Control	22
2.9.1	Ferromagnets with in-plane magnetic anisotropy under piezo- electric strain	22
2.9.2	Ferromagnets with PMA under piezoelectric strain	23
2.10	Domain Walls and Magnetisation Reversal	25
2.10.1	Perovskite Ferroelectrics	26
2.10.2	Ferroelectric Domains and Domain Walls	27
2.10.3	Strain Transfer	28
2.10.4	Ferroelectric Substrates	28

3	Experimental methods	30
3.1	Introduction	31
3.2	Magnetron sputtering	32
3.3	X-Ray Reflectivity (XRR)	33
3.4	Magneto-optical techniques	36
3.4.1	Magneto-Optical Kerr Effect (MOKE)	36
3.4.2	Laser MOKE magnetometer	38
3.4.3	Wide-field Kerr microscopy	39
3.5	Domain width method with image J	42
3.6	SQUID VSM	46
3.7	Magneto-resistance measurement technique	47
3.7.1	Extraordinary Hall Effect (EHE)	48
3.7.2	Anisotropy Measurements of Pt/Co(Fe)B/Ir	50
3.8	Piezoelectric transducers	52
3.8.1	Strain characterisation	53
3.8.2	Biaxial transducers	55
3.9	Summary	57
4	Sample characterisation	59
4.1	Introduction	60
4.2	Sample structure	60
4.3	Polar Laser MOKE	62
4.3.1	Ta(3nm)/[Pt(2.3nm)/Co ₆₈ Fe ₂₂ B ₁₀ (0.51nm)/Ir(0.5nm)] _n /Pt(2.3nm)	62
4.3.2	Ta(3nm)/[Pt(2.3nm)/Co ₆₈ B ₃₂ (0.66nm)/Ir(0.5nm)] _n /Pt(2.3nm)	63
4.4	Kerr microscopy domain imaging	65
4.5	XMCD domain imaging	67
4.6	Anisotropy field measurements	68
4.7	Magnetisation (M_s)	72
4.8	Effective anisotropy (K_{eff})	75
4.9	Exchange stiffness (A)	78
4.10	Domain Period (d)	80
4.11	Interfacial Dzyaloshinskii-Moriya interaction (DMI)	85
4.12	Summary	87

5	Temperature dependence of Dzyaloshinskii-Moriya interaction in magnetic multilayers (in SiOx substrate)	88
5.1	Introduction	89
5.2	Samples	89
5.3	Magnetic characterisation	90
5.4	The scaling of K_u , A and D with M_s	98
5.5	Summary	102
6	Temperature dependence of Dzyaloshinskii-Moriya interaction in magnetic multilayers (in BTO substrate)	103
6.1	Introduction	104
6.2	Samples	104
6.3	Magnetic characterisation	105
6.4	Discussion	113
6.5	Summary	118
7	Anisotropy Measurements under Strain	119
7.1	Introduction	120
7.2	Multilayer system	120
7.3	Anisotropy Measurements	121
7.4	Anisotropy Measurements with strain	124
7.4.1	Pt/CoFeB/Ir and Pt/CoB/Ir on biaxial transducer	124
7.4.2	Magnetostriction of Pt/CoFeB/Ir and Pt/CoB/Ir	127
7.5	Summary	130
8	Conclusions	132
	References	155

List of Figures

2.1	a) Schematic of PMA geometry in a thin film (e.g. Pt/Co/Pt). Energy landscapes of magnetic anisotropy for b) an isotropic system, c) a single easy axis, and d) an easy plane. Taken from Ref [1][2]	7
2.2	Effective anisotropy multiplied by the individual cobalt thickness of the different Co sample plotted against individual thickness of Co, in Co/Pd multilayers. The gradient gives the volume contribution K_v and the intercept equals twice the interface anisotropy K_s [3].	9
2.3	Domain wall structure takes the form of 180° in systems with perpendicular magnetic anisotropy, which are the Bloch-type and the Néel-type DWs. In the Bloch-type DW, the magnetisation rotation occurs perpendicular to the domain magnetisation plane. In the Néel-type DW, the magnetisation rotates along the plane of the domain magnetisation. Δ refers to the domain wall [4].	12
2.4	MFM images of domain patterns for a multilayer of Pt/Co/Al ₂ O ₃ (a) A maze domain structure when an out-of-plane field is applied. (b) A stripe domain structure when an in-plane field is applied [5].	14
2.5	Schematic of the Dzyaloshinskii-Moriya interaction at the interface between a magnetic layer and a heavy metal with a strong spin-orbit coupling.	20

LIST OF FIGURES

2.6	A comparison of multiferroic and magnetoelectric materials. Ferromagnets (ferroelectrics) are a subcategory of magnetically (electrically) polarisable materials that include paramagnets and antiferromagnets (paraelectrics and antiferroelectrics). The intersection (shown with red hatching) denotes multiferroic materials. Magnetoelectric coupling (blue hatching) is a self-contained phenomena that may occur in any material that is magnetically and electrically polarisable. In reality, it is likely to occur in any of these materials, either directly or indirectly via strain, taken from reference [6].	21
2.7	Above represents a centrosymmetric cubic perovskite ABO_3 structure with unit cells having a large A (Ba) cations whereas the centre of the body has a small B (Ti) cation. Oxygen anions takes the face centres [7].	26
2.8	The in-plane unit cell surface area of BTO is shown as a function of temperature for various domain orientations. The dashed lines indicate the BTO c-domain surface area, taken from [8].	27
3.1	Schematic of magnetron sputtering uses to grow high quality. High energy ions are used to bombard on a target to eject atoms which gets deposited on a substrate.	33
3.2	XRR from a Ta/[Pt/CoB/Ir] $_{n=10}$ /Pt multilayer on a Si/SiO _x substrate is shown (black line) along with a fit to the data (red line) performed with the Bede fitting.	34
3.3	MOKE can be further classified by the direction of the magnetisation vector with respect to the plane of incidence and the reflecting surface. Where the red arrows are incident laser light.	37
3.4	Pictorial representation of polar MOKE measurement system. It consists of main optical and electronic components which causes rotation of a polarised light on reflection from perpendicularly magnetised thin film. Both the polariser and the analyser are maintained at 90° to each other.	39

LIST OF FIGURES

3.5	Light path and image formation in Kerr microscope. a) Light travelling from LED lamp is passed through a polariser to get reflected via objective lens and then fall on the sample. The Aperture diaphragm is monitored for selecting the polarisation region needed for polar, longitudinal and transverse Kerr measurement. b) The reflected light from the sample reaches the CCD camera for detection after passing [9].	40
3.6	Domain pattern in a [Pt/CoFeB/Ir]x2 superlattice imaged by a wide-field Kerr microscope at room temperature, following AC demagnetisation.	41
3.7	Magnetic domain of CoFeB image was edited, image J, to produce the FFT. a) A raw image inserted and cut 300x300 pixels with 8 bit, converted the image from 8 bit to 32 bit to increase threshold sensitivity, subtracted the background to improve contrast. b) Convolve and Gaussian blur filters were applied to remove any grainy textures, threshold image to increase the efficiency of the FFT, Fourier transform of the domain image.	43
3.8	An area is spanned across the transformed image to plot intensity peaks for all sides of the ring. b) The intensity peaks of the Fourier transform for greyscale value against distance.	44
3.9	Gaussian fit to the radial peaks intensity of the Fourier transform to extract the domain size.	45
3.10	The configuration of the detection coils principle of a SQUID-VSM. The signal generated in the detection coils which are inductively coupled to the SQUID [10].	47
3.11	A diagram of the set-up for EHE measurements. The new system has been automated such that the measurement software is able to rotate the sample and collect whole measurements. b) The raw resistance before normalisation and as the magnetisation follows cosine law on rotation the resistance has normalised[11]. c) Normalising the data and fitting a parabola to obtain the anisotropy field.	48

LIST OF FIGURES

3.12	Thin film of Pt/Co(Fe)B/Ir deposited on glass substrate and attached with epoxy resin on biaxial piezoelectric transducers. . . .	54
3.13	The diagram shows the effect of the biaxial piezoelectric transducer. When the voltage is increased, the transducer contracts in the x-y plane and expands in the z-direction, perpendicular to the plane of the thin film. The transducer reaches a maximum compression biaxial strain at 150V.	55
3.14	a) and b) show the resistance of Pt/CoFeB/Ir and Pt/CoB/Ir with different repeats against transducer voltage. c) and d) present the strain calculated from the change in resistance of Pt/CoFeB/Ir and Pt/CoB/Ir on biaxial transducers plotted against transducer voltage. The voltage was swept from 0 V then to 150 V and back to 0 V.	57
4.1	Schematic of sample structure and dimensions of the Ta/[Pt/CoFeB/Ir] _n /Pt and Ta/[Pt/CoB/Ir] _n /Pt magnetic thin films were grown on SiO _x substrates. Here, the layer thicknesses are displayed in nm and ‘n’ is the number of Pt/CoFeB/Ir or Pt/CoB/Ir layers in the thin film.	61
4.2	Polar MOKE hysteresis loops for Ta/[Pt/CoFeB/Ir] _n /Pt with different repeats. a) At (n ≤ 2) shows square hysteresis loop and sharp switching. b) As the number of layers increases (2 < n ≤ 12) the hysteresis loops have a wasp shape due to changes in magnetic layers. c) As the number of repeat increases further (15 ≤ n ≤ 20) the saturation field increases, which leads to decrease of remanence. d) The remanent magnetisation and the coercive field, which shows high coercive fields and less remanent magnetisation when the repeats are increased.	63
4.3	Out of plane MOKE for Ta/Pt/CoB/Ir/Pt structures with different repeats. a) The hysteresis loops are square and exhibit sharp switching until n ≤ 5 repeats and started a wasp like from n ≥ 7. b) Above n ≥ 10 repeats the hysteresis loops are no longer switching in a single steps. c) Change of coercive field and remanent magnetisation of Pt/CoB/Ir structures with different repeats. . . .	64

LIST OF FIGURES

- 4.4 Kerr microscopy shows that the demagnetised domain patterns of CoFeB is a function of ‘n’. At the small repeat, $n \leq 2$, the domains show a maze domain and get smaller when the repeats, $5 \leq n \leq 7$, are increased. The bright and dark regions represent out of-plane magnetisation pointing up and down. 66
- 4.5 Kerr microscopy shows that the demagnetised domain pattern of CoB is a function of ‘n’. At the small repeat, $n \leq 2$, the domains show bubbles domain. At $5 \leq n \leq 10$ the domains become small and form as maze domain. Further increase, $12 \leq n \leq 20$, the domains become too small and hard to see. The bright and dark regions represent out of-plane magnetisation pointing up and down. 67
- 4.6 Maze domain pattern in a [Pt/CoB/Ir]_{n=10} superlattice imaged by XMCD-PEEM at room temperature, following ac demagnetisation. a) [Pt/CoB/Ir]_{n=10} on SiOx substrate. b) [Pt/CoB/Ir]_{n=10} on BTO substrate. The scale bar = 1 μm for both images. c) Polar MOKE hysteresis loops for [Pt/CoFeB/Ir]_{n=10} onto SiOx and BTO substrates. 68
- 4.7 Normalised resistance against the sweeping angle in a constant external field of 500mT before improvement. A polynomial fit was applied to the data to extract the quadratic function. a) [Pt/CoFeB/Ir] with (n=10). b) [Pt/CoB/Ir] with (n=10). 70
- 4.8 Normalised resistance against the sweeping angle in a constant external field of 500mT after improvement. A polynomial fit was applied to the data to extract the quadratic function. a) [Pt/CoFeB/Ir] with (n=10). b) [Pt/CoB/Ir] with (n=10). 71
- 4.9 Normalised resistance against the sweeping angle in a constant external field of 500mT. a) A polynomial fit was applied to the data to extract the quadratic function for CoFeB with different repeat. b. A polynomial fit was applied to the data to extract the quadratic function for CoB with different repeat. c) Anisotropy field decreased as the number of repeat increased for both CoFeB and CoB and the solid line is a guide to the eye. 72

4.10 In-plane hysteresis loop of [Pt/CoFeB/Ir]_{x2} with out-of-plane anisotropy deposited on SiO_x. Parameters that can be extracted from experimental data are shown. The red lines are linear fits to data. 73

4.11 Saturation magnetisation (M_s) of Pt/CoFeB/Ir and Pt/CoB/Ir with different repeats. The saturation magnetisation slightly changed with different repeat due to the amorphous nature of the films, which means the atoms have no long-range order and the nearest neighbour atoms change from sample to others. For the Co₆₈Fe₂₂B₁₀ the estimate expected is a little high ~ 1.2 MA/m and for Co₆₈B₃₂ is in the same range ~ 0.95 MA/m 74

4.12 The anisotropy field (H_k) of CoFeB with different repeats. Using three different methods (fitting a parabola, straight line and integrate the area). For fitting a parabola and integrate the area methods, it's shown that the anisotropy field decreases when the number of repeats increases. However, for straight line method the real material behaves in a more complicated and complex, non-linear way and the approximating of straight-line is a less accurate. The integrate the area methods is used to find the K_{eff} as linear response method assumes the work to magnetise the material along the easy axis as zero. The second method, fitting a parabola, is used to investigate the effect of strain with stressor using MR-rig, since we can not use the stressor in SQUID. Also, the MR-rig and MOKE have not enough field to saturate the sample. 76

4.13 The effective anisotropy (K_{eff}) of CoFeB and CoB with different repeats. It's shown that the effective anisotropy decreases when the number of repeats increases due to the surface roughness such as nanocrystalline misorientation, a non-smooth Ta layer and defects. 77

4.14 Temperature dependence of saturation magnetisation for [Pt/CoFeB/Ir] with n=1 and 2, and [Pt/CoB/Ir] with n=5,7 and 10. The red line is Bloch law fit for thin film using Equation 4.2. b) The exchange stiffness at room temperature for CoFeB n=1 and 2 (black point), and CoB with n=5,7 and 10 (red points). 80

LIST OF FIGURES

4.15	a) Magnetic domain of [Pt/CoFeB/Ir] _{x2} imaged by Kerr microscopy and edited using, image J, to produce the FFT. a) A raw image inserted and cut 300x300 pixels. b) Threshold image to increase the efficiency of the FFT. c) A fast-Fourier transform of the domain image.	81
4.16	An area is spanned across the transformed image to plot two intensity peaks for all sides of the inner ring. b) Gaussian fit to the radial average peak intensity of the Fourier transform to gives the average of the domain period.	82
4.17	Typical demagnetised domain patterns at room temperature for CoFeB (n=1 and 2) and CoB (n=5,7 and 10).	82
4.18	Magnetic domain period for the multilayer [Pt/CoFeB/Ir] (n=1 and 2) and [Pt/CoB/Ir] (n=5,7 and 10) grown on SiO _x substrate at room temperature. The domain period for both system decreases when the number of repeats increases.	83
4.19	Domain wall energy for the multilayer [Pt/CoFeB/Ir] (n=1 and 2) and [Pt/CoB/Ir] (n= 5,7 and 10). The domain wall energy of CoFeB and CoB has increased with number repeats and after CoB n=5 slightly decreased at CoB n=10.	84
4.20	DMI constant D for the multilayer [Pt/CoFeB/Ir] (n=1 and 2) and [Pt/CoB/Ir] (n=5,7 and 10). The resulting DMI of CoB is less than what we can get with CoFeB and the number of stacking does not influence the DMI.	86

LIST OF FIGURES

5.1	a) Hysteresis loops measured at room temperature by magneto optic Kerr effect with field applied out of plane. b) Hysteresis loops measured at room temperature by SQUID with field applied in-plane. c) The saturation magnetisation was measured from SQUID-VSM hysteresis loops in in-plane (hard-axis) configuration in the temperature range 9-290 K. d) Temperature dependence of saturation magnetisation normalised to the low temperature value and the solid lines are fits to the data using Equation 4.2 in (Chapter 4). e) The effective anisotropy (K_{eff}) and intrinsic perpendicular anisotropy (K_u) in the temperature range 9-290 K.	91
5.2	The Exchange stiffness for CoFeB n=2 and CoB n= 5 and 7, using Bloch's law for thin films in the temperature range 9- 290 K. Exchange stiffness decreases with increasing temperature due to renormalisation of the magnon spectrum by the thermal magnons.	92
5.3	Demagnetised domain patterns imaged by Kerr microscopy at different temperature for (a) CoFeB (n = 2), (b) CoB (n = 5) and, (c) CoB (n=7). The images have been adjusted to display maximum contrast between up/down domains.	94
5.4	An area is spanned across the transformed image to plot two intensity peaks for all sides of the inner ring for CoB (n=7). b) Gaussian fit to the radial average peak intensity of the Fourier transform to extract the domain period. (c) Domain period vs. temperature for all three samples. Error bars are smaller than the data points. . .	95
5.5	Domain wall energy density for the multilayer [Pt/CoFeB/Ir] n=2 and [Pt/CoB/Ir] n=5 and n=7.	96
5.6	The temperature-dependence of DMI constant D for the multilayer [Pt/CoFeB/Ir] (n=1 and 2) and [Pt/CoB/Ir] (n=5 and 7).	97
5.7	Scaling of the intrinsic perpendicular anisotropy K_u with MS. The solid red line represents the Callen-Callen scaling law $K_u \sim m^2$. . .	99
5.8	Scaling of A with M_s , normalised by the low temperature values. The solid red line represents $A \sim m^{1.8}$	100
5.9	Scaling of D with M_s , normalised by the low temperature values. The solid red line represents $D \sim m^{1.8}$	101

6.1	a) Measurement of hysteresis loops at room temperature using the magneto optic Kerr effect with an out-of-plane field. b) In the temperature range 13-320 K, the saturation magnetisation was determined using SQUID-VSM hysteresis loops in an in-plane (hard-axis) configuration. c) Temperature dependence of saturation magnetisation normalised to the low temperature value and the solid lines represent fitted data using Equation 4.2 in (Chapter 4). d) Effective anisotropy (K_{eff}) and e) intrinsic perpendicular anisotropy (K_u) for temperatures ranging from 13 to 320 K.	106
6.2	: The exchange stiffness for CoFeB (n=2) and CoB (n= 4) onto BTO and SiOx substrates, using Bloch's law for thin films in the temperature range 13-320 K. Exchange stiffness decreases with increasing temperature due to renormalisation of the magnon spectrum by the thermal magnons.	107
6.3	a) Kerr microscopy images of demagnetised domain patterns for CoFeB (n = 2) sample across the temperature range on BTO, with three from CoFeB (n = 2) sample on SiOx for comparison. The BTO domains of CoFeB (n=2) appears as stripes of approximately equal width in the rhombohedral phase and as stripes of unequal width (but identical direction) in the tetragonal phase. Adjustments have been made to the images to maximise contrast between the up/down domains.	109
6.4	Kerr microscopy images of demagnetised domain patterns for CoB (n = 4) sample across the temperature range on BTO, with three from CoB (n = 4) sample on SiOx for comparison. The BTO domains of CoB(n=4) and SiOx CoB (n=4) approximately are the same size and no effect from the temperature. Adjustments have been made to the images to maximise contrast between the up/down domains.	110

6.5	a) An area is spanned across the transformed image to plot two intensity peaks for all sides for CoFeB (n=2) in BTO and due to the stripe domains the FFT pattern is not any more a ring. substrate and . b) Gaussian fit to the radial average peak intensity of the Fourier transform to extract the domain period. c) Domain period vs. temperature for CoFeB (n=2) and CoB (n=4) in BTO substrates with phase transitions of BTO as functions of temperature. d) Domain period vs. temperature for CoFeB (n=2) and CoB (n=4) in SiOx substrates. Error bars are smaller than the data points.	111
6.6	Domain wall energy density for the multilayer [Pt/CoFeB/Ir] n=2 and [Pt/CoB/Ir] n=4 in BTO and SiOx substrates.	112
6.7	Exhibits the temperature-dependence resulting DMI constant D of CoFeB (n=2) and CoB (n=4) into BTO and SiOx substrates. .	113
6.8	Kerr microscopy images of demagnetised domain patterns for CoFeB (n = 2) sample across the temperature range on BTO. a) The first image of CoFeB (BTO) was taken at room temperature before we went down to low temperature. b) Three images of CoFeB (n=2) at different phase transition for BTO.	114
6.9	a) and b) Scaling of the intrinsic perpendicular anisotropy K_u with M_s for CoFeB and CoB into BTO and SiOx. The solid red line represents the Callen-Callen scaling law $K_u \sim m^2$	116
6.10	a) Scaling of D with M_s , normalised by the low temperature values with a separate fit to different phase transitions for CoFeB/BTO. The solid red line represents $D \sim m^{1.8}$ for all the samples. b) Scaling of D with M_s , normalised by the low temperature values for CoB (n=4) in BTO and SiOx.	118

7.1	a) A $[\text{Pt}/\text{CoFeB}/\text{Ir}]_n$ Polar MOKE hysteresis loops with different repeats (these samples were grown on glass) . At ($n < 2$) displays a square hysteresis loop and sharp switching. With an increasing number of layers, ($2 \leq n \leq 10$)), the hysteresis loops develop a wasp shape due to changes in magnetic layers. b) A $[\text{Pt}/\text{CoB}/\text{Ir}]_n$ Polar MOKE hysteresis loops with different repeats. The hysteresis loops are square and sharp switching until $n = 5$ repeats and started a wasp-like from $5 \leq n \leq 10$). c) Saturation magnetization (M_s) of Pt/CoFeB/Ir and Pt/CoB/Ir with various repeats.	121
7.2	A schematic representation of measurement geometry and a sample on a transducer.	122
7.3	Normalised resistance against the sweeping angle in a 500mT constant external field and the inset in <i>a</i> and <i>b</i> are one sweep between -180° to 180° . a) A polynomial fit was applied to the data to help in extracting the quadratic function for CoFeB on a glass substrate with different repeat. b. A polynomial fit was applied to the data to help in extracting the quadratic function for CoB on a glass substrate with different repeat. c) Anisotropy field reduced with an increasing number of repeats for both CoFeB and CoB, and the solid line is a guide to the eye.	123
7.4	Plots of the magnetic anisotropy field against biaxial transducer voltage for $[\text{Pt}/\text{CoFeB}/\text{Ir}]_n$ multilayers ($n = 1,2,5,7,10$). Three measurements are averaged to give each data, and the error bars are standard errors on the mean values.	126
7.5	Plots of the magnetic anisotropy field against biaxial transducer voltage for $[\text{Pt}/\text{CoB}/\text{Ir}]_n$ thin films ($n = 1,2,5,7,10$). Three measurements are averaged to give each data, and the error bars are standard errors on the mean values.	127
7.6	a) and b) are the change in the anisotropy field of Pt/CoFeB/Ir and Pt/CoB/Ir with different repeats due to out-of-plane strain ϵ_z induced by biaxial transducers. The solid line is a fit of the data to Equation 2.	128

LIST OF FIGURES

- 7.7 The magnetostriction constant of Pt/CoFeB/Ir and Pt/CoB/Ir with different repeats . The solid line is a guide to the eye. 129

CHAPTER 1

Introduction

There is a constant desire to increase the amount of data we can store on ever-smaller devices. As these devices shrink, so do the power supplies, and now more than ever we need devices that can work efficiently. Arrays of magnetic elements are used to store information as the magnetisation of each element can be put in one of two directions. Today the spin configuration in magnetic memory devices can be changed by the spin transfer torque (STT) or by using a magnetic field [12]. Also, using electric fields, in two different kind of devices: 1) Hybrid ferroelectric-FM structures where strain-induced spin switching can be achieved based on the magnetoelastic coupling and 2) in voltage controlled magnetic tunnel junction (MTJ) based on the magneto-electric coupling [13][14].

Decreasing the size of the storage elements enables increasing the density of stored data. As the thickness of the magnetic layer decreases, the current density required to switch the magnetic state also generally decreases. This is good but it isn't intrinsically the lowest-energy method of switching a nanomagnet, because there is still significant current flow. The ideal situation would be switching a nanomagnet via an electric field which has lower energy consumption. This electric field control would be helpful in many applications such as the magnetic tunnel junction (MTJ), used in current hard disks and magnetic random access memory (MRAM) technology [15]. It is not hard to imagine that these methods will also find use in the manipulation of domain walls (DWs) in racetrack memory, and other emerging solid state memory devices [16] and many other new types of solid state memory.

For a successful switch of magnetisation [17][18][19][20], effect on domain wall motion [21][22] and change of magnetic anisotropies [23][24], electric fields are used and implemented widely in various types of magnetic structures. There are often preferable in plane magnetic directions for the systems researched. Nevertheless, structures with out of plane magnetisation or so called perpendicular magnetic anisotropy (PMA) are essential for many data storage applications and new spintronic applications. In general, more efforts need to be exerted for deeper and further studies of the concept of electric field control of PMA [17] [22][23][24].

Perpendicular magnetic anisotropy (PMA) has proved to be important in technological applications involving the use of devices that store data. Out-of-plane anisotropy is considered strong hence resulting into a high energy barrier to

magnetisation. In addition, data that is encoded as up and down magnetisation states will have good stability. High anisotropy enables the domain walls to remain narrow hence allowing for higher density in terms of storage for both the hard disk drive platters [25] and domain wall racetrack devices [16], where PMA materials also offer efficient current-induced domain wall motion [26].

High anisotropy has both challenges and benefits. The reversal of magnetic states is paramount for the writing of data. This calls for the need for large amounts of energy that are necessary to overcome the energy barrier resulting from high anisotropy. Large amounts of energy are obtained from switching fields or currents. A large PMA limits the threshold current density [27] in technological applications that employ the knowledge of current-induced domain wall motion. The control of magnetisation reversal or modification of PMA by use of electric fields enables the lowering of the energy barrier against magnetisation reversal, reduction of undesirable heating effects, and lowering the amount of energy required [28].

MRAM technology is mainly used with the intention of decreasing the energy consumed during writing. Insufficient experiments that can satisfy the three criteria for an ideal voltage-controlled memory device simultaneously exist. The three criteria include high storage capacity, room temperature operation, and low power consumption [29]. One way to reduce power consumption is to replace ferromagnetic materials with multiferroic materials that exhibit PMA, since this requires less energy to electrically reverse the magnetisation [22]. Application of strain to a thin film containing PMA that results in the reduction of anisotropy is another preferred method. It further reduces the required magnetic fields in observing domain wall motion [30]. The methods grant the satisfaction of the three criteria; thus, it improves the storage potential of the MRAM that can be used without any disadvantage as compared to random access memory (RAM) as well as the memory devices.

The purpose of this research is to investigate the effect of strain on magnetic thin films with Dzyaloshinskii-Moriya interaction (DMI) and understand the process of controlling magnetisation. We open with a short literature review into current advances in magnetic anisotropy and how the magnetic anisotropy and so the energy needed to switch a magnetic element can be controlled by

strain. It is advisable to use a ferroelectric to understand the effect of strain on the DMI and the influence on magnetic spin structures which are domain walls, skyrmions, and vortices in a film.

1.1 Thesis overview

The experiment measuring magnetic properties of Pt/Co₆₈Fe₂₂B₁₀/Ir and Pt/Co₆₈B₃₂/Ir thin films and how the properties change upon application of the strain by changing the temperature and from a piezoelectric transducer is described in this thesis. At the same time, the immediate chapters expand on it by describing the theoretical background (Chapter 2) that are required, alongside the methods needed to experiment on the issue (Chapter 3). Chapter 4 describes Samples characterisation of multilayers of Pt/CoFeB/Ir and Pt/CoB/Ir. Chapter 5 and 6 gives details of temperature dependence on the DMI measurements in Pt/CoFeB/Ir and Pt/CoB/Ir using thermally oxidised Si (SiOx) and barium titanate (BTO) substrates. In Chapter 7, the measurements of magnetic anisotropy will be described in Pt/CoFeB/Ir and Pt/CoB/Ir under strain from biaxial piezoelectric transducers. Chapter 8 summarises these results together with suggestions on how this project might continue.

CHAPTER 2

Theoretical Background

2.1 Introduction

This section will outline the physical basis upon which the experiment relies. Sections 2.2 discusses magnetic anisotropy, and is divided into three parts with a focus on the two major ones related to PMA in the samples measured: magnetocrystalline anisotropy in section 2.2.1 and the second one is magnetoelastic anisotropy in section 2.2.3. The Stoner-Wohlfarth model will also be discussed in section 2.2. The Dzyaloshinskii-Moriya interaction and observation using domain width will be described.

2.2 Magnetic anisotropy

Magnetic materials are often preferred one specific direction to magnetise than others, with a small applied field needed to saturate the magnetisation along its easy axis rather than the hard axis. This effect is defined as magnetic anisotropy, and indicates the directional dependence of the magnetic properties of a material [31]. Many factors cause magnetic anisotropy, which will be described in this section. The factors are: magnetocrystalline anisotropy, shape anisotropy, and magnetoelastic anisotropy [3].

2.2.1 Magnetocrystalline anisotropy

Magnetocrystalline anisotropy depends on the material crystal structure, resulting from the spin-orbit interaction (SOI) and the interaction of the crystal field. The spin-orbit interaction is the main source of magnetocrystalline anisotropy. The definition of SOI is the interaction between the orbital angular momentum and electron spin angular momentum, causing an alteration of energy levels in the atom [32]. One example of magnetocrystalline anisotropy is uniaxial anisotropy, where the magnetic material has a single easy axis, with magnetisation in other directions that require a significantly more energy. The energy density in this case is given by the equation.

$$E_k = K_1 \sin^2 \theta + K_2 \sin^4 \theta + \dots \quad (2.1)$$

2.2 Magnetic anisotropy

where θ is the angle between the direction of the material's magnetisation and the easy axis, known as the magnetisation angle as shown in Figure 2.1. K_1 and K_2 indicate the first and second order anisotropy constants. The equation can be solely given to the first order term:

$$E_k = K \sin^2 \theta \quad (2.2)$$

representing an easy plane perpendicular to the easy axis when $K < 0$, or a uniaxial system with one easy axis when $K > 0$ [3]. The magnetic energy landscapes of isotropic (Figure 2.1.b) and uniaxial systems are shown in (Figures 2.1.c and d). Equation (2.2) can be generalised to describe a system with a main out-of-plane anisotropy axis K_z and a further in-plane anisotropy K_{ip} :

$$E_k = K_z \sin^2 \theta + K_{ip} \sin^2 \theta \cos(2\phi) \quad (2.3)$$

where ϕ is the in-plane angle, representing as the angle between the direction of the material's magnetisation and the easy plane.

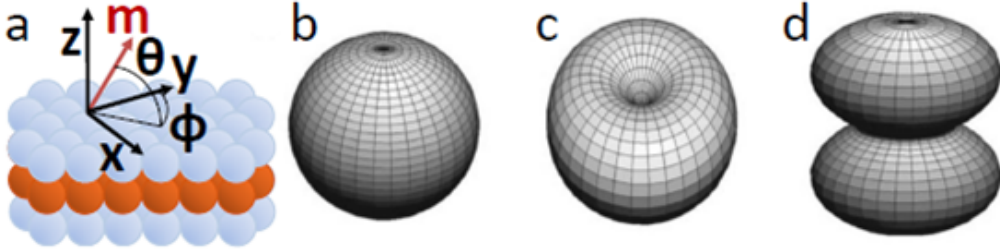


Figure 2.1: a) Schematic of PMA geometry in a thin film (e.g. Pt/Co/Pt). Energy landscapes of magnetic anisotropy for b) an isotropic system, c) a single easy axis, and d) an easy plane. Taken from Ref [1][2]

2.2.2 Shape anisotropy

Shape anisotropy results from the magnetostatic interactions between magnetic dipoles. Magnetostatic interactions are the long-range nature which means the

field inside the sample is oriented in the opposite direction of the applied magnetic field. Many shapes of magnetostatic energy can be approximated by the energy of an ellipsoid, represented by the following equation:

$$\epsilon_m = \mu_0 V D M_s^2 \quad (2.4)$$

where μ_0 is the vacuum permeability, V is the volume of magnetic material, D is the demagnetising factor, and M_s is the saturation of magnetisation [31]. $D' = \frac{1}{2}(1 - D)$ represents the factor of demagnetisation in the perpendicular, hard direction. When magnetisation is uniformly aligned on the material surface, magnetic charges will exist on the surface of the sample, costing dipolar energy Figure 2.2. This is can be represented by the shape anisotropy energy density:

$$K_{sh} = \frac{1}{4} \mu_0 M_s^2 (1 - 3D) \quad (2.5)$$

In the case of thin films, $D = 1$, so that the shape anisotropy is given by $K_{sh} = -\frac{1}{2} \mu_0 M_s^2$. Magnetic domains can be created at the cost of magnetostatic interaction energy. A demagnetising field results from the charges of magnetostatic surface in a uniformly magnetised material:

$$H_D = -\mu_0 M_s \quad (2.6)$$

The magnetisation direction is opposite direction to that of the demagnetising field. In case the thin film is divided into domains with the magnetisation pointing in different directions, the demagnetising field is decreased.

2.2.3 Magnetoelastic anisotropy

The magnetoelastic effect is caused by the SOI, which couples the spin moment to the lattice through orbital electrons. The magnetostriction determines the magnetoelastic coupling of a thin film [33]. In addition, a small strain of the thin film is found to induce to a significant change to the coupling coefficient of magnetoelastic. In case the magnetoelastic coupling in CoFeB is large, it is expected to have a significant effect on magnetic properties, such as domain wall velocity and anisotropy. This behaviour can be applied to a strain dependence of

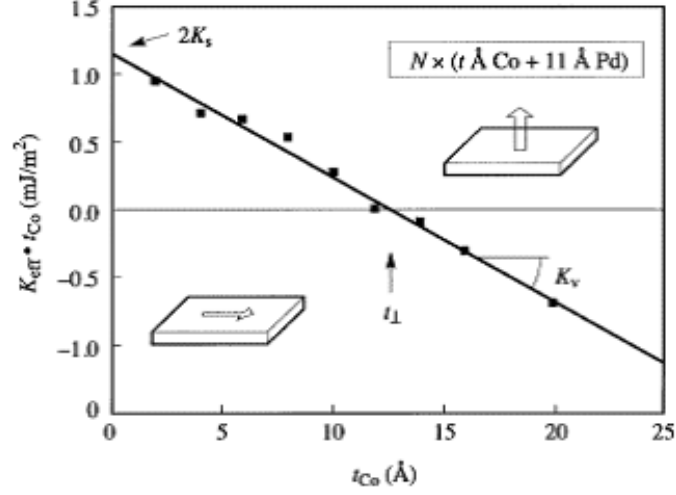


Figure 2.2: Effective anisotropy multiplied by the individual cobalt thickness of the different Co sample plotted against individual thickness of Co, in Co/Pd multilayers. The gradient gives the volume contribution K_v and the intercept equals twice the interface anisotropy K_s [3].

second-order in magnetoelastic energy density. In a polycrystalline material, the following equation represents the energy density:

$$E_{el} = \frac{\lambda \varepsilon Y}{2} (3 \cos^2 \alpha - 1) + \frac{\varepsilon^2 Y}{2} \quad (2.7)$$

where E_{el} is magnetoelastic anisotropy, λ is spontaneous magnetostriction constant, ε is the strain, Y is Young's modulus, and α is the angle between the axis of applied stress and the magnetisation. The elastic contribution to the energy of magnetic anisotropy is obtained by meeting two conditions: the strain axis and easy axis are aligned ($\theta = \alpha$), and equating the energy dependence of the elastic energy to the uniaxial anisotropy, given by Equation (2.2). This results in:

$$K \sin^2 \theta = \frac{-\lambda \varepsilon Y}{2} (3 \cos^2 \alpha - 1) \quad (2.8)$$

The following equation is reduced when compared to the equation for uniaxial anisotropy energy $E_k = K \sin^2 \theta$:

$$K_{el} = \frac{3\lambda \varepsilon Y}{2} \quad (2.9)$$

The constant of elastic anisotropy is the additional contribution to the magnetic anisotropy K_{eff} in case where the strain is applied to the magnetic material. The effect is the opposite of magnetostriction:

$$K_{eff} = \frac{K_s}{t} + K_v - \frac{1}{2}\mu_0 M_s^2 + K_{el} \quad (2.10)$$

where K_{eff} is the effective anisotropy constant, K_s is interface or surface contribution, K_v is volume contribution and t is thickness of the magnetic film.

2.3 Stoner-Wohlfarth model

The Stoner-Wohlfarth model explains the angular dependence of the energy of a magnetic particle when the magnetisation rotates simultaneously with the macroscopic spin. Based on the model particle where a uniformly magnetised ellipsoid with a uniaxial anisotropy resulting from magnetocrystalline or shape origin, the density of energy is represented as follows:

$$E = K_{eff} \sin^2 \theta - \mu_0 M_s H \cos(\phi_H - \theta) \quad (2.11)$$

where K_{eff} is the effective anisotropy constant, equal to the sum of the first-order anisotropy constant K_1 and the shape anisotropy $K_{eff} = K_1 - \frac{1}{2}\mu_0 M_s^2$ [31]. The second term is the interaction between the saturation magnetisation M_s and the applied field H . The angle between the magnetisation and the axis normal to the film is θ , while the angle between the applied field and the axis normal to the film is ϕ_H . The Stoner-Wohlfarth model can be used to derive the shape of hysteresis loops. The field that required to rotate and saturate the magnetisation in the direction of the hard axis is called anisotropy field:

$$H_k = \frac{2K_{eff}}{\mu_0 M_s} \quad (2.12)$$

The anisotropy field H_k , in films where PMA is dominant ($K_{eff} > 0$), can be measured through saturating the magnetisation along the easy axis (out-of-plane) and then applying a field H along the hard axis (in-plane). The technique of Stoner-Wohlfarth model can be applied in case where the rotation of magnetisation is coherent.

2.4 Perpendicular Magnetic Anisotropy

Perpendicular magnetic anisotropy (PMA) is a term that is used to explain the orientation of both the easy and hard axes with reference to the film surface or material. The easy axis is usually perpendicular while the hard axis is in-plane with the surface of the material. These materials have high thermal stability because of the in-plane characteristic that causes high magnetic anisotropy [34][3][35]. This is a desirable characteristic that makes them applicable in a number of technological circuits and devices [36] [37]. Thin films which have the PMA characteristics have a magnetic anisotropy that is given by the formula:

$$K_{eff} = K_v + \frac{2K_s}{t} \quad (2.13)$$

Magnetocrystalline and volume contributions are always contained in K_v , which tend to be in-plane. The surface contribution K_s , on the other hand, can be out-of-plane. This behaviour depends on the spin-orbit interactions on the base layers, together with the crystallographic properties of the magnetic material. The interaction relationship between the volume and surface anisotropies greatly determines the strength and direction of magnetic anisotropy. Also, the interface contribution is often highly linked to the perpendicular magnetic anisotropy from X-ray magnetic circular dichroism (XMCD) measurements [38] [39][40]. In the determination of band structures of X/Co interfaces, calculations show that spin-orbit coupling combined with the hybridisation of Co and non-magnetic heavy element X (for example Pt, Pd, Ir or Au) will result to PMA. PMA is desirable because it reduces the current density by improving the efficiency during spin-switching [41]. This is evident in CoFeB films where the current density during spin-switching is greatly reduced because these films have a moderate saturation magnetisation [42] [43] and a high spin polarisation [44].

2.5 Magnetic domain wall

In order to reduce the energy of particles, uniformly magnetised materials are often broken into sections called domains. A domain wall (DW) is the region

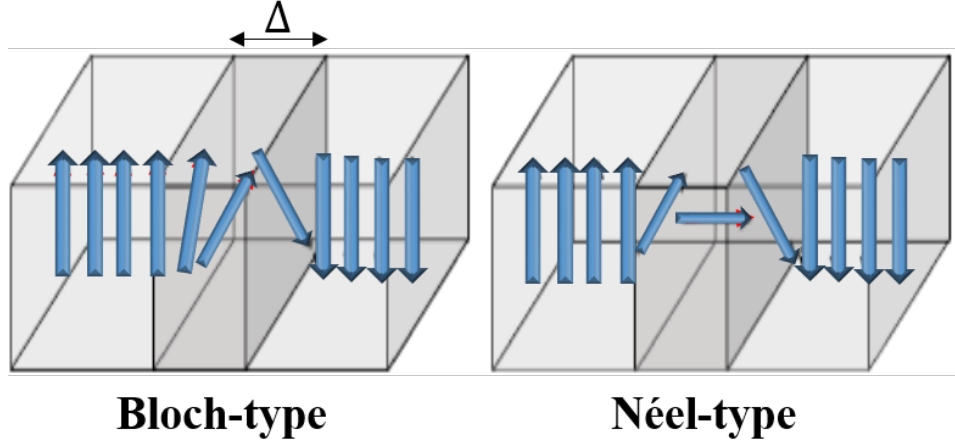


Figure 2.3: Domain wall structure takes the form of 180° in systems with perpendicular magnetic anisotropy, which are the Bloch-type and the Néel-type DWs. In the Bloch-type DW, the magnetisation rotation occurs perpendicular to the domain magnetisation plane. In the Néel-type DW, the magnetisation rotates along the plane of the domain magnetisation. Δ refers to the domain wall [4].

of interface between two domains of different orientation, as illustrated below Figure 2.3 using perpendicular anisotropy systems. The domain width (d) refers to the length within which the rotation of domain wall takes place. However, the degree or rate of rotation is dependent on the strength of the coupling and the anisotropy. For perpendicular anisotropy in magnetic systems, the spins rotate 180° up to and down within the directions of magnetisation.

There are two types of domain walls for systems with PMA, i.e the Bloch-type DW and the Néel-type DW. These differ with reference to the direction of magnetisation rotation. In the Bloch-type DW, the magnetisation rotation occurs perpendicular to the domain magnetisation plane resulting into a helical spin spiral [45]. In the Néel-type DW, the magnetisation rotates along the plane of the domain magnetisation resulting into a cycloidal spin spiral.

However, the Néel walls can be stabilised by a process called the Dzyaloshinskii-Moriya interaction so as to fix their sense of rotation.

2.5.1 Equilibrium domain pattern

When PMA materials are demagnetised, their structure is a complex domain pattern formed by labyrinthic structures of domains that pointing either up or down. This is the case for all materials, including very thin films. The example in Figure 2.4 shows typical patterns for a multilayer of Pt/Co/Al₂O₃ [5]. The resulting pattern after demagnetisation will largely depend on the history of the applied field and its direction. The precise demagnetised pattern is dependent on the direction and history of the applied field: when an out of plane field is applied, a labyrinth domain (maze) structure forms (Figure 2.4 (a)), however when an in plane field is applied, domains stay parallel and form a typical stripe pattern (Figure 2.4 (b)). Here, the domain wall energy can be estimated by using the density and width of the domains. The theory of infinite parallel stripe domains [46] suggests that the domain width is a function of the domain wall energy, and the research includes other terms like the Zeeman, magnetostatic, anisotropy, and the exchange. Due to the fact that DMI-favored Néel walls have a lower energy, the DMI interaction has a significant effect on the equilibrium domain width. PMA materials have domain widths that are larger than the width of the domain wall. Here, the magnetostatic contribution is caused by the charges at the top and bottom surfaces, and the DW energy can be obtained using the formula:

$$\sigma_{DW} = 2A/\Delta + 2K_{\text{eff}}\Delta - \pi \cos(\phi)|D| \quad (2.14)$$

where A is the exchange stiffness, $|D|$ is the DMI constant and ϕ is angle of projection of the internal DW magnetisation. The value of the equilibrium domain width can be obtained by minimising the energy with respect to the domain width Δ and core angle ϕ . This results in a critical value D_c . When $D \leq D_c$, the configuration is a Bloch wall. But when $D > D_c$, it is a Néel wall. This technique was initially used for Néel wall configuration only, with $\cos(\phi) = 1$ thus making the DW energy density to simplify to: $\sigma_{DW} = -\pi|D|$. The angle of projection in $\cos(\phi) = 1$ removed such limitation and improved the results by simplifying the dipolar configuration in the internal structure of DW [47][48]. This makes sense in thicker samples where the dipolar energy varies the internal magnetisation along the thickness with or without DMI. The above model was

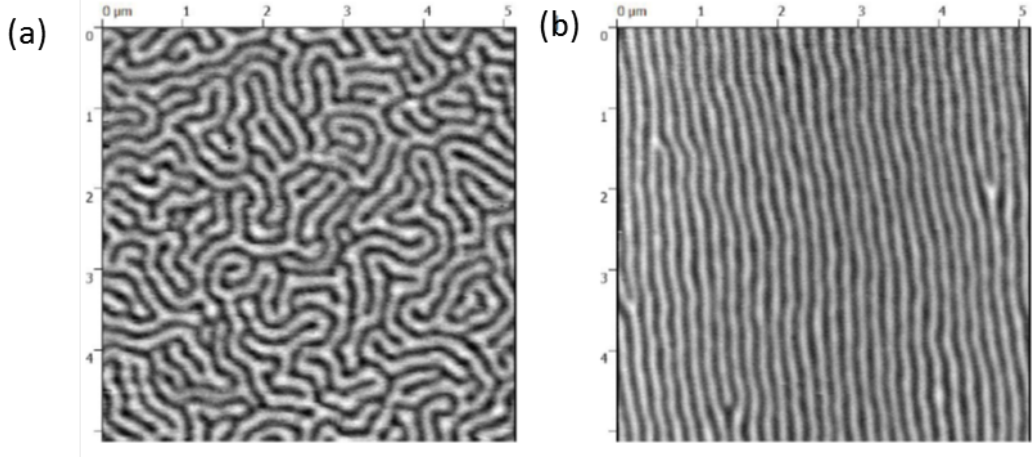


Figure 2.4: MFM images of domain patterns for a multilayer of Pt/Co/Al₂O₃ (a) A maze domain structure when an out-of-plane field is applied. (b) A stripe domain structure when an in-plane field is applied [5].

then extended so as to allow variations of angle ϕ for each layer of the samples [49].

This resulted in the analytical expression below which gives the DW energy (σ_{DW}) as a function of the domain width d :

$$\sigma_{DW} = \frac{\mu_0 M_s^2 f d^2}{Nt} \sum_{\text{odd } k=1}^{\infty} \frac{1}{(\pi k)^3} \left(1 - \left(1 + \frac{2k\pi Nt}{d} \right) \left(e^{-\frac{2k\pi Nt}{d}} \right) \right) \quad (2.15)$$

where μ_0 is the vacuum permeability, M_s is the saturation of magnetisation, f is the magnetic volume ratio of full stack, d is the periodicity of the magnetic domain, N is the number of repeats layers, and t is the thickness one layer. Using the domain width obtained experimentally, the domain wall energy can then be calculated and the DMI constant estimated. This method has previously been applied in three different ways like: analytical estimations [50] [51] [52] [53] comparisons with micromagnetic simulations [54][55][12, and scaling of the energy of an experimental image [56].

2.6 Magnons

When the temperature of a material exceeds its Curie temperature, ferromagnetism does not occur because of the critical thermal fluctuations. Also, very low temperatures causes spinwave excitations which affect the ferromagnetism of the material. This is because there is not enough energy to flip the individual spins and the atoms just oscillate periodically through the spin orientation. Spin wave is a term used with reference to a lattice. In solids, it is referred to as magnons, with its energy given as $\varepsilon_k = \hbar\omega_k$. Equation (2.16) below shows the relationship between energy and wave vector, k , given a chain of one-dimensional isotropic spins.

$$\varepsilon_k = Dk^2 \quad (2.16)$$

where D is spinwave stiffness $D = 2\mathcal{J}Sa^2$, \mathcal{J} is the nearest-neighbour exchange interaction, S is the spin quantum number of each atom, and a is lattice constant [31]. During thermal equilibrium, magnons which are excited in the mode k , $\langle n_{\mathbf{k}} \rangle$, can be given in the Planck distribution given below [2.17]: [57]

$$\langle n_{\mathbf{k}} \rangle_T = \frac{1}{e^{\hbar\omega_k/k_B T} - 1} \quad (2.17)$$

Distribution of magnons is represented by $\langle n_{\mathbf{k}} \rangle$ with the existence of the wave vector within the first Brillouin zone. Equation (2.18) below gives the saturation magnetisation of a sample at zero kelvin, $M_s(0)$:

$$M_s(0) = \frac{g\mu_B N S}{V} \quad (2.18)$$

Where V is volume, g is g-factor, and $N = 1$ for SC lattice, 2 for BCC lattice, 4 for FCC lattice. When we combine equations (2.17) and (2.18), we obtain an equation for the magnetisation at temperature T , $M_s(T)$:

$$\frac{M_s(T)}{M_s(0)} = 1 - \frac{a^3}{NS} \sum_k \langle n_k \rangle_T \quad (2.19)$$

where a is the lattice parameter which comes from the volume term.

When the sample is bulk, the total number of magnons excited at temperature T , $\sum_k \langle n_k \rangle_T$ can be given as three integrals in the x, y, and z directions.

Thermal occupation is independent of the Brillouin zone, and this can be transformed into cylindrical coordinates. This allows all the angular parts to be solved trivially, resulting to:

$$\sum_k \langle n_k \rangle_T = \frac{4\pi}{(2\pi)^3} \int_{k=0}^{\sqrt{k_{max}}} \frac{1}{e^{\frac{\hbar\omega_k}{k_B T}} - 1} k^2 dk \quad (2.20)$$

$$\sum_k \langle n_k \rangle_T = \frac{1}{4\pi^2} \left(\frac{k_B T}{D} \right)^{\frac{3}{2}} \int_0^\infty dx \frac{x^{\frac{1}{2}}}{e^x - 1} \quad (2.21)$$

A substitution can be made with Equation (2.16) and $x = Dk^2/k_B T$, and the result is shown in Equation (2.21). After the replacement of the standard integral $\left(\int_0^\infty \frac{x^{1/2}}{e^x - 1} dx \right)$ for the gamma function as well as the $\left(\Gamma\left(\frac{3}{2}\right) \xi\left(\frac{3}{2}\right) \right)$ for the function of Riemann's zeta, The Bloch's law is estimated in Equation (2.22) and (2.23) [57].

$$\frac{M_s(T)}{M_s(0)} = 1 - \frac{a^3 \eta}{NS} \left(\frac{k_B T}{D} \right)^{\frac{3}{2}} \quad (2.22)$$

$$\eta = \frac{\Gamma\left(\frac{3}{2}\right) \xi\left(\frac{3}{2}\right)}{4\pi^2} = 0.0587 \quad (2.23)$$

where η is a dimensionless constant equal to 0.0587 for a bulk ferromagnet. For thin film, evaluating Bloch's law requires some modifications, because the number of k-points in the thickness is few, we can no longer integrate in this direction. This reduction in volume is because of the less thermally excited magnons which in turn cause a reduction in the number of spinwave modes along the axis. Therefore, $\langle n_{\mathbf{k}} \rangle$ has negligible effect. The lowest order of excitation in a solid is the FMR mode in which there is no effect of the reduction in the sample volume. This mode is highly occupied, meaning that $\langle n_{\mathbf{k}} \rangle$ is inversely proportional to the sample thickness. Choosing z as the axis perpendicular to the film we must evaluate Equation (2.19) similarly to bulk films, though the sum of components in the z -axis will be constant, and the transformation is noticed in cylindrical coordinates. This results in the equation below:

$$\sum_k \langle n_k \rangle_T = \frac{1}{4\pi} \frac{1}{n_z a_z} \sum_{k_z=0}^{\pi/a} \int_{k_\rho=0}^{\sqrt{k_{\rho,max}}} \frac{1}{e^{\frac{\hbar\omega_k}{k_B T}} - 1} k_\rho dk_\rho \quad (2.24)$$

where n_z is number of atomic layers in the z direction a_z is distance between atomic layers in the z direction [58] [59]. To obtain Equation (2.25) below, Equation (2.16) was substituted with $x = \frac{Dk_x^2}{k_B T}$, and $y = \frac{Dk_z^2}{k_B T}$, with the assumption of an isotropic ferromagnet.

$$\sum_k \langle n_k \rangle_T = \frac{1}{4\pi} \frac{1}{n_z a_z} \frac{k_B T}{2D} \sum_{k_z=0}^{\pi/a} \int_0^{x_{\max}} \frac{1}{e^{x+y} - 1} dx \quad (2.25)$$

Further improvements include the substitution for the definite integral $\int_0^{x_{\max}} \frac{1}{e^{x+y} - 1} dx = -\ln(1 - e^{-y})$ and $k_z = \frac{n\pi}{n_z a_z}$.

An applied magnetic field or anisotropy is required for ferromagnetism to occur in thin film materials. This means that an additional energy term $\hbar\omega$ should be added to the equation, as shown in Equation (2.26). In case the FMR measurement is taken, it is in the form of $\hbar\omega_{FMR}$. It can also take the form of $\hbar\omega_0 = g\mu_B\mu_0 H_{K_{eff}}$ if the taken measurements are in the absence of an external field. Equation (2.27) is from the equation of Kittel [57].

$$\sum_k \langle n_k \rangle_T = -\frac{1}{4\pi} \frac{1}{n_z a_z} \frac{k_B T}{2D} \sum_{n=0}^{n_z} \ln \left(1 - e^{-\left(D\left(\frac{n\pi}{n_z a_z}\right)^2 + \hbar\omega_0\right)/k_B T} \right) \quad (2.26)$$

$$\omega_0 = \frac{g\mu_B}{\hbar} \mu_0 (H' - H_d + H_k) \quad (2.27)$$

where is H' the external field, H_d is the demagnetising field, and H_k is the anisotropy field [57]. Using the equation, $\eta = \sum \langle n_k \rangle_T / \left(\frac{k_B T}{D}\right)^{\frac{3}{2}}$, η becomes proportional to the density of the magnon in the thermal equilibrium. Substitution can be done to Equation (2.26) by Equation (2.22) for further description of the Bloch's law in a thin film [58] [59].

$$\frac{M_s(T)}{M_s(0)} = 1 + \frac{a^3}{NS} \frac{1}{4\pi} \frac{1}{n_z a_z} \frac{k_B T}{2D} \sum_{n=0}^{n_z} \ln \left(1 - e^{-\left(D\left(\frac{n\pi}{n_z a_z}\right)^2 + \hbar\omega_0\right)/k_B T} \right) \quad (2.28)$$

This equation can then be fitted into the magnetisation against temperature data so as to get an output for the zero temperature spinwave stiffness D . Given that $D = 2\mathcal{J}Sa^2$, it is possible to calculate the exchange stiffness, A , of a ferromagnet using Equation (2.29) and by substituting for \mathcal{J} . The term exchange stiffness refers

2.7 Dzyaloshinskii-Moriya interaction

to the amount of energy which is needed to rotate or turn the magnetisation away from the main magnetisation direction[59].

$$A = \frac{N\mathcal{J}S^2}{a} \quad (2.29)$$

This gives the zero-temperature value for the exchange stiffness. However, to obtain the value for exchange stiffness at different temperature, the value will need to be renormalised. For example, the bulk value for the exchange stiffness of Co is 31 pJm⁻¹ [31][58]. Mohammadi et al. proved that when the thickness of a magnetic material decreases, η increases and D decreases, thus resulting to an increase in A [59]. Also, Nembach et al. proved that the value of η decreases until it plateaus at the value of 0.0587 after 10 nm when the thickness of the material increases [58].

2.7 Dzyaloshinskii-Moriya interaction

W.Heisenberg [60] and P. Dirac [61], in 1926, discovered quantum mechanical exchange interaction, which is at the base of magnetic characteristics of materials. It is made up of both strong symmetric and weak antisymmetric contributions. The symmetric component, otherwise referred to as the Heisenberg interaction, favours the collinear orientation of neighbouring spins. However, the antisymmetric component, otherwise referred to as the Dzyaloshinskii-Moriya interaction (DMI) prefers canted orientation of adjacent spins. It was originally proposed by I. Dzyaloshinskii [62] in 1958. Later, it was proposed by T. Moriya [63] in 1960. The existence of DMI requires spin-orbit interaction [63] and the crystal environment, which lacks the central symmetry. Several materials that have properties like homochiral (single-handed) spin spirals [64][65] and skyrmion (particle-like spin configuration) lattices [66][67] are considered as the magnetic ground states. DMI can also exist in thin film heterostructures that lack structural inversion symmetry. In 1980 A. Fert and P. M. Levy [68] proposed that symmetry breaks at the interface of the magnetic and non-magnetic layer in such a case, if the spin-orbit coupling of a non-magnetic atom is large, a Dzyaloshinskii-Moriya-type exchange interaction between two atoms of the magnetic layer can be mediated.

Dzyaloshinskii-Moriya interaction is an important mechanism in metals for various magnetic properties. It is basically an anisotropic exchange interaction between two neighbouring magnetic spins. These interactions enhance chiral spin structures such as Néel domain walls. The presence of DMI in thin magnetic films with PMA creates an effective magnetic field in-plane with the domain walls, but perpendicular to its direction. Dzyaloshinskii tensor components depend on the material and its crystal structure. DMI results in creation of complex spin structure due to favourable orthogonal alignment of spins. The energy exchange in DMI is expressed by:

$$\mathcal{H}_{\text{DMI}} = -\mathbf{D} \cdot (\mathbf{S}_1 \times \mathbf{S}_2) \quad (2.30)$$

where S_1 and S_2 are adjacent spins and D is DMI vector. Thin film heterostructures forming a major concern in this thesis have an interfacial DMI existing [68][69] because the inversion symmetry is broken at the interface. Such a condition presents the possibility that a large spin-orbit coupling of a non-magnetic atom can simplify a Dzyaloshinskii Moriya interaction between two magnetic atoms, as shown in Figure 2.5. On the other hand, the DMI generation can occur when an atom-thick magnetic layer on the layer with a large spin-orbit coupling [70][71][72]. Such systems have thin layers and employ spin-orbit coupling hence giving rise to a perpendicular magnetic anisotropy [38]. These system types were grown and studied because of their perpendicular magnetisation. This is because perpendicular magnetisation possesses useful technological applications [25][16]. The PMA in the system may become intense, thus restricting the spin spiral formation. Therefore, the DMI was overlooked in thin-film systems for more than two decades.

2.8 Multiferroics

The polarisation of a ferroelectric material is stable and switchable which can be reversed when an electric field is applied. The stable and switchable magnetisation that arise through the quantum mechanical effect of the exchange interaction

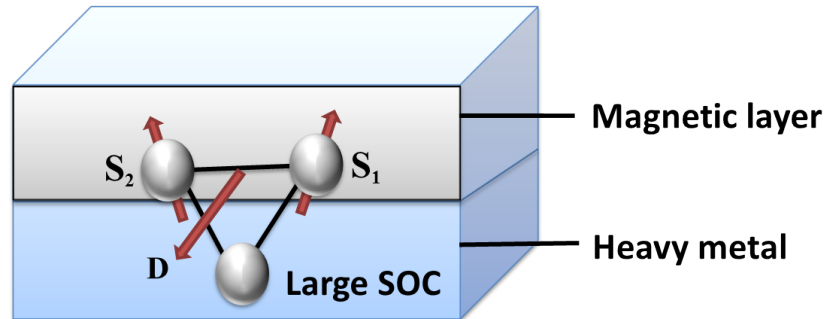


Figure 2.5: Schematic of the Dzyaloshinskii-Moriya interaction at the interface between a magnetic layer and a heavy metal with a strong spin-orbit coupling.

are exhibited by a ferromagnetic material [6]. A multiferroic can be generally described as a material that can exhibit two or three properties of ferroic [73]. This definition has recently improved to specify that includes ferromagnetism and ferroelectricity. Ferroelasticity, which is the third ferroic property, has been generally excluded in practice. The classification of the ‘multiferroic’ and ‘magnetoelectric order are shown in Figure 2.6.

Research concerning multiferroics is currently ongoing because of the possibility of altering and controlling their magnetic properties electrically. This is different from the current method of magnetisation manipulation that is done by the application of a magnetic field. In addition, the reversal of magnetisation as compared to the traditional magnetic memory for a multiferroic requires less energy [22]. It implies that the introduction of a spin-polarised current significantly reduces the writing energy in MRAMs. This leads to the diminishing of the handicap of memory technologies that are non-volatile [74][75][28]. Initially, both magnetisation and polarisation were thought to have the ability to independently alter and encode the data in a single multiferroic bit. In 2015, a demonstration of memory having four distinct stable states was introduced [76]. However, after the examination of pioneering papers, it is possible that the two order parameters have been coupled in practice [77][78]. Coupling can enable writing of data electrically and reading it magnetically. In this case, the issues that surround the generation of a large local field required for writing data is avoided.

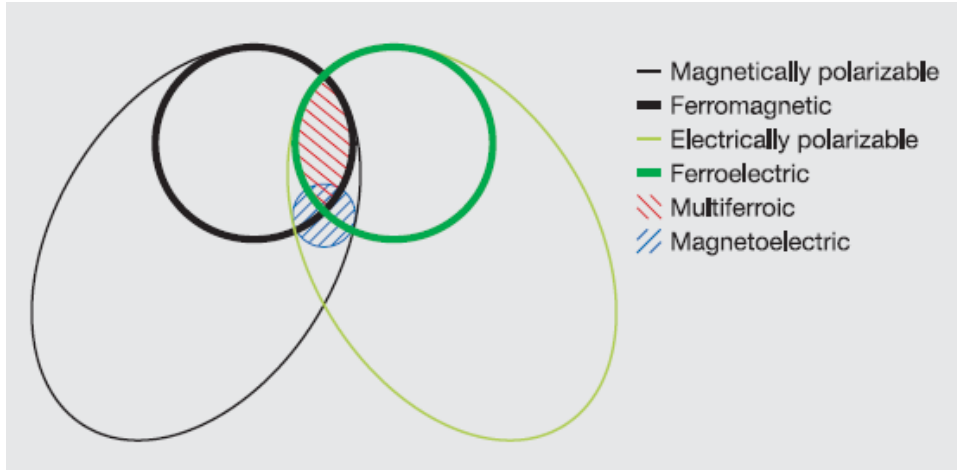


Figure 2.6: A comparison of multiferroic and magnetoelectric materials. Ferromagnets (ferroelectrics) are a subcategory of magnetically (electrically) polarisable materials that include paramagnets and antiferromagnets (paraelectrics and antiferroelectrics). The intersection (shown with red hatching) denotes multiferroic materials. Magnetoelectric coupling (blue hatching) is a self-contained phenomena that may occur in any material that is magnetically and electrically polarisable. In reality, it is likely to occur in any of these materials, either directly or indirectly via strain, taken from reference [6].

Ferroelectric materials may be referred to as pyroelectric, as a function of temperature, they facilitate a change in spontaneous polarisation. In case the polarisations of the materials are not switchable by external fields, they can be pyroelectric but not ferroelectric. However, all ferroelectrics are piezoelectric. Therefore, there is the induction of a volatile change in their polarisation upon the application of strain. Therefore, creation of charges at the piezoelectric surfaces occurs due to the induced polarisation hence it becomes possible to measure the voltage across it. The application of an electric field to a piezoelectric has a converse effect resulting in the development of strain. Ferroelectrics can also be considered to be ferroelastic because their polarisation is associated with a spontaneous lattice elongation. For this reason, the application of stress in such materials leads to a spontaneous strain that can be switched hysteretically [79][80][81].

2.9 Strain Mediated Control

The control of the properties of a ferromagnetic thin film by voltage is granted by multiferroic heterostructures that occurs with strain acting as the intermediary. There is an electric analogue that ferromagnets contain as ferromagnetic materials, which can hold a remanent polarisation. Several ferroelectrics are considered as piezoelectric. This means that a voltage will develop across them upon deformation. Conversely, the application of a voltage induces strain. Lead magnesium niobate-lead titanate (PMN-PT), barium titanate (BTO), and lead zirconate titanate (PZT) are examples of the ferroelectric materials that are usually used in multiferroic heterostructures. The common application of lead zirconate titanate (PZT) is in transducers. The exploitation of a wider range of properties is allowed by ensuring that layered structures of the materials possess various ferroic ordering. A research conducted on multiferroics and multiferroic heterostructures demonstrates [82][83] an overview of the range of approaches as well as the mechanism employed. While the majority of work on multiferroic heterostructures has employed magnets with in-plane anisotropy, strain control has also been achieved in a few cases of systems with PMA.

2.9.1 Ferromagnets with in-plane magnetic anisotropy under piezoelectric strain

Strain can be used to manipulate magnetic anisotropy alongside the domain walls in in-plane magnetic materials. The domain structure of the ferroelectric is exhibited by BTO, which changes upon the application of the electric fields. The lattice parameters of the material have changes associated with the changing domain pattern; hence, a change in the magnetic anisotropy can be achieved through the straining of a ferromagnet coupled to the BTO [84]. When the electric field is applied to BTO with CoFe grown on top, that leads to the rotation of the magnetisation with the stripe domains in the ferroelectric inducing similar pattern within the ferromagnetic domains. This action allows reinstatement and removal of the magnetic domains pattern as well as the movement of the domain walls [85]. The domain wall motion control occurring through strain coupling has

also been observed in FeGa coupled to piezoelectric transducers [86] and FeGa on BTO [87]. Through strain, electric fields were used to control the magnetisation of spin valves formed on a piezoelectric layer. The injection of a single domain wall resulted into the realisation that straining the spin-valve lead to an increase in the propagation and coercive fields of the free layer[88]. Due to the fact that the structure behaved similarly to a domain wall gate, the notion may be used to the construction of low-power magnetic logic. [88], or pinning and de-pinning of DWs that is found in the racetrack memory [16].

Strain can lead to the switching of small magnetic elements. There is a proposal made with regard to memory devices that employ multiferroic heterostructures with magnetic islands at the intersections within the meeting points of a grid of ferroelectric material [89]. The application of strain also leads to the switching of Ni nanostructures which grown on PMN-PT by 90° [90]. The control of small magnetic elements using strain may prove useful for applications of multiferroic data storage. There is tangible progress with regards to non-volatile control of magnetisation states within in-plane magnetic systems. The application of electric fields to a PMN-PT/CoFeB structure can lead to magnetisation changes with loop-shaped hysteresis that is remained after the removal of field [91]. PMN-PT/Ni reveals various changes that occur in-plane magnetic anisotropy under the circumstance of the piezoelectric operating under the system with a remanent strain-state [92]. Applications as memory and data storage devices could be found in non-volatile systems which allows a strain-induced state to persist without more voltage output applied to ferroelectric.

2.9.2 Ferromagnets with PMA under piezoelectric strain

According to the studies conducted, several multiferroic heterostructures are perceived to contain PMA. Application of voltage led to the exhibition of changes in the shapes of hysteresis loops on CoPd alloys grown on PMN-PT [23]. This shows that PMA reduction was achievable through straining the CoPd. Changes also show up in Pd/Co/CoFeB structures on PZT when subjected to strain where the measurement of the nucleation and coercive fields are taken from the hysteresis loop [88]. The measurement of changes in domain wall motion has occurred

in ferromagnetic semiconductors on piezoelectric transducers. The variation of mobility in the current-driven domain walls, is (500% in (Ga, Mn) with PMA at 90 K [93]. They reflect on the clear changes in the PMA system properties when subjected to strain from piezoelectric materials. Pt/CoFeB and Pt/CoB thin films have been chosen for this work due to their extensive use of the PMA system model for domain wall motion studies. Strains are induced by changing the temperature and piezoelectric transducers, which tunes the PMA of Pt/CoFeB and Pt/CoB, thus provide space for modifications of the domain wall motion.

2.10 Domain Walls and Magnetisation Reversal

Domains refer to regions having uniform magnetisation, while domain walls are the planar regions separating the domains. This is where the rotation of magnetisation can be rotated from one direction to the other. The minimisation of free energy results in the domain structure of ferromagnets. If a field is applied to the ferromagnet, then the total magnetisation of the sample will be altered. This is achieved by either moving the domain walls or rotating the magnetisation of the domains towards the applied field. The domain structure will be eliminated as the applied magnetic field is increased. A perfectly soft ferromagnet can adopt the most gradual variation of magnetisation direction that can ever be achieved parallel to the surface. Since no surface charge is created, its energy is reduced [31]. The orientation of the domains and the position of the domain walls dictate the magnetostatic energy to be expected. PMA material contains high anisotropy, leading to their narrow, nanosized domain walls. This separates the reversed and unreversed regions of magnetisation within thin films [94]. The reversal of magnetisation in thin films requires an application of an external field to provide the force used to drive the domain wall motion. This increases the size of the reversed regions of magnetisation. The control of domain wall motion has previously been achieved in perpendicularly magnetised materials by applying an electric field [22]. The control level achieved was over a full order of magnitude. Pt/Co and Pt/CoB thin films were used to complete the expected experiment observing intrinsic low power consumption. The experiment provided the first steps into the effects that result from the control of domain wall motion electrically in thin films. It also allowed further investigation into the same but with increased practicality. The limitation of the paper is that it presents simulation-based results since they are not extracted from the real devices.

Shepley et al. in the experiments use a strain to a Pt/Co/Pt thin film by the use of piezoelectric transducers. This experiment aimed at altering the PMA and decreasing the magnetic field needed for the induction of domain wall motion, thus it reduces the energy barrier to magnetisation reversal [30]. Expansion of this idea is possible. This can be achieved by the application of a uniaxial in-plane strain in the Pt/CoFeB/Ir as well as Pt/CoB/Ir thin films that contain a

strong PMA in contrast to the out-of-plane strain. This is because it provides an attempt to recreate a non-linear dependence of magnetic anisotropy energy that Gowtham et al; observed in 2016 [95].

2.10.1 Perovskite Ferroelectrics

The frequently studied ferroelectrics are Perovskite oxides. The Figure 2.7 below consists of a space group $Pm3m$. The corners of the unit cell has large cations A and small cation B at the centre of an oxygen octahedron. Perovskites have a variety of physical properties, depending on their composition. These include being metallic, ferromagnetic, insulating and ferroelectric, with $BaTiO_3$ becoming an example of ferroelectric perovskites. It is the first perovskite ferroelectric to be introduced with Ba^{2+} as A and Ti^{4+} as B. At 120 °C the transition of the first phase of ($P4mm$) to the tetragonal structure occurs. More transitions of orthorhombic ($Amm2$) which happens at 5°C and a rhombohedral ($R3m$) occurring at 90°C. Each phase transition has a small distortion of the crystal lattice. Besides, another view can be given to it as elongation through the edge ([001]) in the tetragonal phase. In the orthorhombic and the rhombohedral phase, it is viewed as an elongation along a face diagonal ([011]) and along a body diagonal ([111]) respectively.

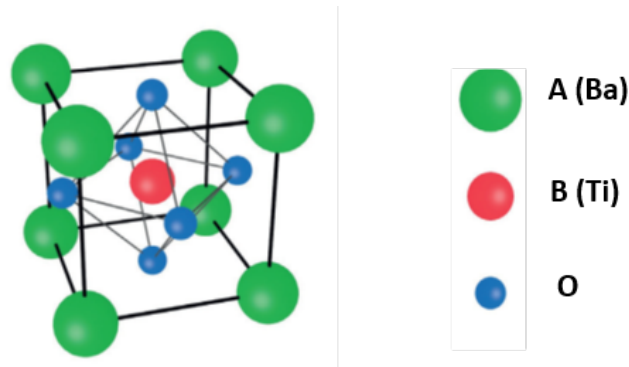


Figure 2.7: Above represents a centrosymmetric cubic perovskite ABO_3 structure with unit cells having a large A (Ba) cations whereas the centre of the body has a small B (Ti) cation. Oxygen anions takes the face centres [7].

2.10.2 Ferroelectric Domains and Domain Walls

Ferroelectrics are known to be divided into uniformly polarised regions called domains. A major difference lies in the fact that the crystal lattice's spontaneous deformation is two orders of magnitude larger than that which result due to magnetostriction in ferromagnets [96][97]. Therefore, the role of strain relaxation is more important than the depolarising effects of electrostatic energy. It is possible to minimise the latter through the splitting of the ferroelectric into domains having oppositely oriented polarisation. The ferroelastic properties ensure the presence of strain in the material, hence the domains formed are perpendicular orientations of polarisation. The manner in which the sample is grown, the mere presence of the sample surface, the strain imposed by a substrate, and crystal impurities strongly affect the domains [98][99][100].

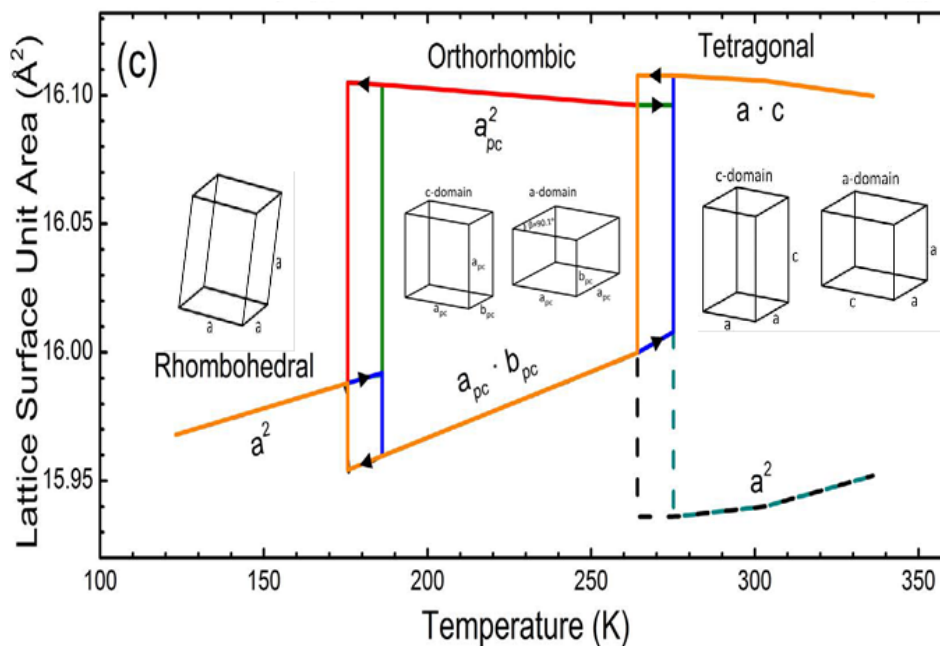


Figure 2.8: The in-plane unit cell surface area of BTO is shown as a function of temperature for various domain orientations. The dashed lines indicate the BTO c-domain surface area, taken from [8].

2.10 Domain Walls and Magnetisation Reversal

Domains of different polarisation orientation normally use a nomenclature according to Merz in plate-like crystals and thin films of a (001) orientation of the surface [81]: *c*-domains refers to the domains that contains polarisation that is normal to the surface whereas in-plane polarisation is exhibited *a*-domains as shown in Figure 2.8.

2.10.3 Strain Transfer

Imposing strain on a magnetic thin film causes magnetoelectric coupling. A piezoelectric substrate or thin-film can be used to generate the strain. Volatile strains can also be imposed by the piezoelectricity occurring in most ferroelectric materials [101][102][103]. Domains as well as various strain states at remanence are exhibited by ferroelectric-ferroelastic materials, for instance, for the tetragonal phase for the BaTiO₃, the lattice elongation pointing out-of-plane in the *c*-domains also in two in-plane directions in *a*₁- and *a*₂-domains which are orthogonal. As a result, it is possible to obtain different three-level remanence states, thus leading to bi-stable strain [104][105]. The strain state of ferromagnetic films that is in contact with piezoelectric or ferroelectric component of a heterostructure can be changed by the application of the electric field [101][106]. Ferromagnet deformation leads to changes in the saturation magnetisation, the coercive field, transitions occurring in the magnetic phase, and the Curie temperature. A more important occurrence is the possible change in the orientation, symmetry or magnetic anisotropy strength. This converse magnetoelectric effect can work if the induced strain of the electric field is larger than the ferromagnetic component's own created strain.

2.10.4 Ferroelectric Substrates

The use of ferroelectric such as BaTiO₃, which imposes strain, can change the magnetic properties to non-volatile. Several publications do not demonstrate the rotation of the anisotropy axis. it is the only reasonable explanation for the macroscopically observable effects. [104][107][108].

The previous investigations popularly involved the use of strain, which associates with the structural phase transitions of BaTiO₃ to enable changes within

2.10 Domain Walls and Magnetisation Reversal

the magnetic anisotropies of adjacent ferromagnetic thin films [109][101]. The measurement of the changes is taken as abrupt jumps within the coercivity of magnetisation as a function of temperature in magnetic films such as FeCo [110], Ni [110], Fe [107][111], and CoFe_2O_4 [112]. Demonstration of switching in epitaxial Fe/BaTiO₃ heterostructures was done between uniaxial anisotropy which are induced in the orthorhombic phase and cubic anisotropy associated with the tetragonal phase [113][114].

When an electric field is applied to ferromagnetic/ferroelectric heterostructures, it causes the non-volatile transformation of magnetic properties. A great example is the demonstration of non-volatile switching between perpendicular magnetic anisotropy and an in-plane anisotropy. However, it was only demonstrated locally using Ni films on BaTiO₃ [115]. Rationalisation of most of the macroscopic results obtained from the electric field control of magnetisation in BaTiO₃-based heterostructures can be achieved with the assumption that on a microscopic scale, various ferroelectric domains can have a different effect on the magnetisation. It is contrary to the uniform strain that piezoelectric substrates impose. The ferroelastic domains of BaTiO₃ modulate the magnetoelastic anisotropy in a ferromagnetic thin film. This occurs through interfacial strain transfer and inverse magnetostriction. Strain transfer from the tetragonal lattice of a BaTiO₃ substrate can occur during the following occurrences. These include during the cooling down process that occurs through the paraelectric-to-ferroelectric phase transition [116][117][84] and the growth of the thin film. It can also occur after the application of an electric field [84]. Domain correlations will be obtained in case the strain-induced anisotropy dominates over the magnetocrystalline anisotropy plus the exchange and magnetostatic interactions that occur between domains.

CHAPTER 3

Experimental methods

3.1 Introduction

This chapter describes the methods and equipment used for characterising the magnetic properties of the Pt/Co(Fe)B/Ir multilayers. The films in this study were deposited by dc magnetron sputtering deposition. The first characterisation of the thin films to determine layer thicknesses using X-ray reflectivity (XRR). Second, magneto-optic Kerr effect (MOKE) magnetometer is used to confirm perpendicular magnetic anisotropy of the hysteresis loop. After that the Kerr microscopy is used to investigate domains at room temperature. Then, superconducting quantum interference device vibrating sample magnetometry (SQUID VSM) is used to measure the moments as function of temperature to obtain the magnetisation and exchange stiffness. Anisotropy field measurements are performed by using extraordinary Hall effect (EHE) technique through magnetoresistance (MR) rig equipment. Lastly, image editing and computational analysis software, image J, was used to calculate domain size.

Different types of samples have deposited on silicon oxide (SiOx) and barium titanate (BTO) [001] substrates by magnetron sputtering system. Substrates are cut before being placed under acetone and physically agitated by means of an ultrasonic bath for 10 minutes. Once this has completed, a further 10 minutes of ultrasonic agitation is performed in IPA, to remove any residues from the surface. The substrates are then inserted into a vacuum chamber after being dried by air or N_2 . The purpose of using SiOx substrate is to optimize the thickness of magnetic layer and to achieve the best PMA since the BTO substrates are very expensive. However, for device applications we would prefer if the films were grown directly onto stressors, rather than relying on piezoelectric for instance PZT, as done in previous studies [118][93]. BTO [001] was used as piezoelectric substrate. BTO applies strain in the plane of the device when voltage-biased, and more interestingly BTO can generate strain purely by changing the temperature [8] making it useful for separating the effect of strain and that of the applied electric field at the interface [119].

3.2 Magnetron sputtering

The films in this study were deposited by the technique of sputter deposition. The basic sputtering process is carried out in a sputter chamber which is pumped with a roughing pump such that it goes down to a range of 20 and 30 mTorr in pressure. Further, with the use of a cryo pump the sputtering system reaches a base pressure to 10^{-7} Torr. Now, a liquid nitrogen Meissner trap is used to condense water vapour. This reduces the pressure inside the sputtering chamber to 10^{-8} Torr. A Residual Gas Analyser (RGA) is utilised to determine the pressure and gas composition/water content in this chamber. One such DC magnetron sputtering system is shown in Figure 3.1. As it can be seen, the target material is a cathode and the shield maintained as the anode. A potential difference is maintained between these two electrode systems. Argon gas is introduced in this sputtering chamber which gets ionised with the application of the potential difference. This accelerates the high energy positive argon ions towards the target. The high energy ions bombard the target and results in ejection of metal atoms from its surface. These metal atoms get deposited on the substrate. The magnets, in Figure 3.1, within the sputter gun increase the sputtering rate and allows the gun to operate at much lower pressure (1.5 mTorr). Some of the electrons emitted from the target get confined at the target by the Lorentz force. This force occurs due to the magnetic field applied below the target. Now, these electrons which are near the target further increase the sputter rate as the ionisation of Argon gas increases. The ejected atoms from the target gain a kinetic energy of 1-100 eV. This energy is approximately two orders of magnitude greater than that of evaporation techniques [120]. The system explained above consists of the substrates which are attached to a rotating wheel. This wheel is movable between guns carrying different target materials to grow films with multilayer thin films. There are 6 non-magnetic guns, 2 magnetic guns and they can operate either as RF or Dc sputtering. The sample wheel could hold to a maximum of 16 different samples. The thickness of these layers can be calibrated to the deposition time for each gun. This is done by growing the bilayer repeats of a material and having the thickness measured by X-ray reflectivity. A shutter system and the sample wheel system are controlled such that different material can be sputtered and

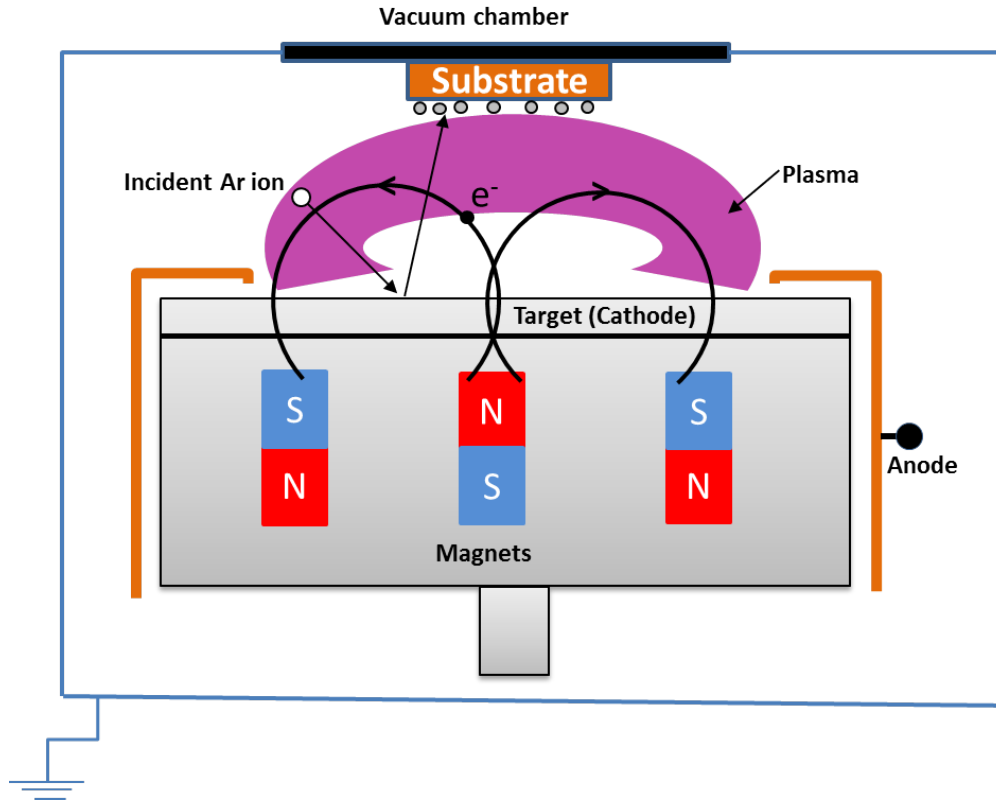


Figure 3.1: Schematic of magnetron sputtering uses to grow high quality. High energy ions are used to bombard on a target to eject atoms which gets deposited on a substrate.

sublimated thermally. The sputter target are pre sputtered for 5 mins before the deposition of samples, to remove any oxide layers and surface contamination.

3.3 X-Ray Reflectivity (XRR)

The thickness of one bilayer in the super lattice can be measured by using the low angle X-ray reflectivity patterns of the samples. Figure 3.2 is shown an example of XRR from a [Pt/CoB/Ir] x10 multilayer with Bede fitting. The aim is to reach the most accurate deposition rate for very thin films (thickness of some Angstroms). The deposition rate of each material can be determined by varying the thickness of one layer in two stacks. That is often used to measure interface

3.3 X-Ray Reflectivity (XRR)

roughness/inter- diffusion, film thickness, critical angle and superlattice period as shown in Table 3.3 . The penetration length of X-ray is related to $\sin(\theta/\mu)$ where μ is the material permeability. So for grazing rate the beam can reach the substrate surface (for thicknesses less than 1 μm) and create low frequency fringes known as "Kiessig fringes". There would be 100% reflection for incidence angles less than critical angle θ_c , as refractive index of X-ray is less than one. In addition, if the sample is a repeated layers (superlattice), Bragg like peaks would act in the pattern as a result of constructive interference from bilayer interfaces, and their position and separation is contrariwise related to bilayer thickness, similar to Kiessig fringes.

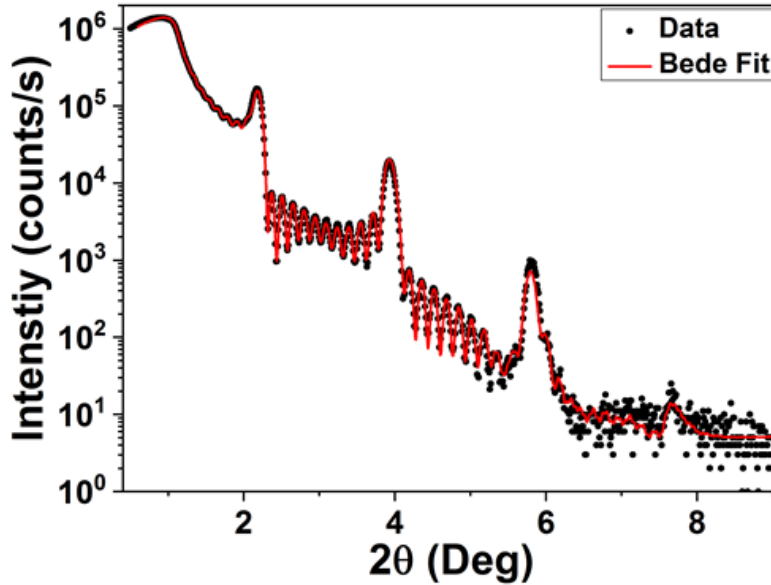


Figure 3.2: XRR from a Ta/[Pt/CoB/Ir] $_{n=10}$ /Pt multilayer on a Si/SiOx substrate is shown (black line) along with a fit to the data (red line) performed with the Bede fitting.

Table 3.3 : Extracted parameters from Bede fits of the XRR data of Figure 3.2 for Ta/[Pt/CoB/Ir] $_{n=10}$ /Pt. The table shows the value of thickness and roughness for each layer.

3.3 X-Ray Reflectivity (XRR)

Material	Thickness (Å)	Density (%)	Roughness (Å)
Si	∞	100	0.0
SiO _x	934.07	97.26	6.28
Ta	27.69	95.63	5.62
Pt	30.00	99.88	5.64
Co ₆₈ B ₃₂	6.46	97.78	2.60
Ir	4.53	97.53	1.12
Pt	28.41	97.69	5.47
Co ₆₈ B ₃₂	6.40	98.00	2.78
Ir	4.01	98.99	1.00
Pt	28.19	97.55	5.59
Co ₆₈ B ₃₂	6.72	97.82	2.82
Ir	4.55	99.63	1.10
Pt	28.07	95.81	5.58
Co ₆₈ B ₃₂	6.81	97.25	2.91
Ir	4.53	96.94	1.13
Pt	27.57	95.93	5.44
Co ₆₈ B ₃₂	6.78	97.92	2.90
Ir	4.45	97.52	1.17
Pt	27.61	94.52	5.51
Co ₆₈ B ₃₂	6.60	98.12	2.96
Ir	4.66	98.29	1.21
Pt	26.21	92.12	5.32
Co ₆₈ B ₃₂	6.57	98.34	2.99
Ir	4.85	95.94	1.29
Pt	25.63	91.24	5.25
Co ₆₈ B ₃₂	6.20	99.00	2.95
Ir	4.29	99.03	1.19
Pt	25.28	91.42	5.19
Co ₆₈ B ₃₂	6.34	98.39	3.04
Ir	4.83	99.25	1.37
Pt	25.10	90.49	5.22
Co ₆₈ B ₃₂	6.46	98.99	3.11
Ir	4.49	99.78	1.27
Pt	24.98	94.47	5.27

3.4 Magneto-optical techniques

Magneto-optical effects can be used to characterise magnetic material properties. In this study, the magneto-optical Kerr effect (MOKE) has been utilised to obtain magnetic details from thin films. A laser MOKE magnetometer was utilised to describe magnetic hysteresis loops such as coercive field and remanent magnetisation, while a wide-field Kerr microscope was used to image the domain pattern in a demagnetised state.

3.4.1 Magneto-Optical Kerr Effect (MOKE)

In the late 19th century in 1877 [121], a unique phenomenon of plane rotation of a polarised light about its principal axis when reflected from a magnetised surface was observed by John Kerr. This reflected light is passed through another polariser in order to be detected by a photodiode. Finally, a lock-in amplifier compares the incident and the reflected light. This phenomenon was named as Kerr effect, which is relevantly useful for opaque materials like metallic thin films. The foundational discovery of Kerr effect was laid down by Faraday in 1845 [6], when he measured similar phenomena in transmission of light through magnetic materials. The basic fundamental behind both the discoveries is the weak coupling of the optical and magnetic properties of different materials. This study of magnetic characterisation of samples is performed through Magneto-optical Kerr effect (MOKE). According to measurement orientation, Kerr effect has three possible geometries (shown in Figure 3.3)[122]:

(i) Polar Kerr effect: This effect occurs when the magnetisation component of the sample is out-of-plane and the incident light is perpendicular to the surface (i.e. angle of incidence of light is 0°). The light reflected from this effect has a rotated polarisation and ellipticity gain.

(ii) Longitudinal Kerr effect: This effect occurs when the component of magnetisation is in-plane and the angle of incidence of light $> 0^\circ$). Here the magnetisation component is parallel to the plane of incidence and disturbs the light of all polarisations. Similar to polar effect, the light reflected from this effect has a rotated polarisation and ellipticity gain.

(iii) Transverse Kerr effect: This effect occurs when the magnetisation is perpendicular to the plane of incidence and parallel (in-plane) to the surface of the sample. Thus, there is only change in reflectivity of the light with magnetisation direction; hence there is no rotation for the component of light which is perpendicular to the plane of incidence.

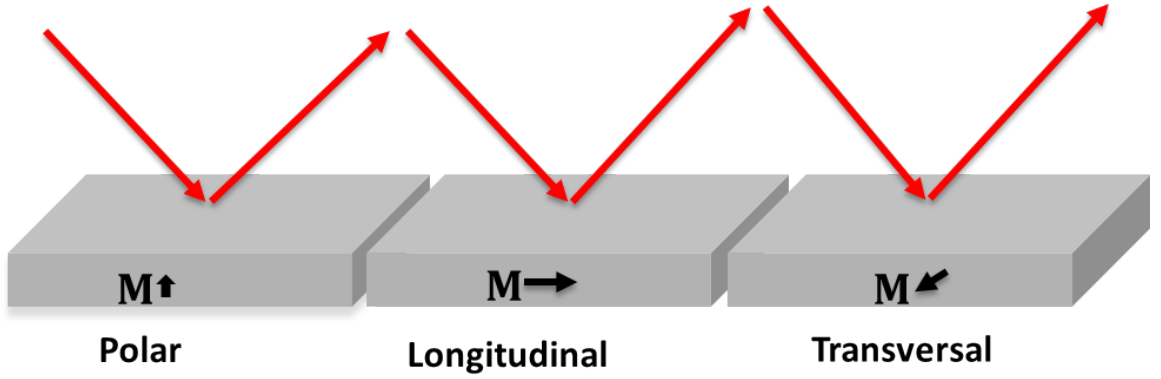


Figure 3.3: MOKE can be further classified by the direction of the magnetisation vector with respect to the plane of incidence and the reflecting surface. Where the red arrows are incident laser light.

Having thus understood the Kerr effect geometries, it is now important to mention that light penetrates up to skin depth (approximately 20 nm) in magnetic materials. The electrical permittivity of a material ϵ decides the velocity of the light in a given material through the following relation, $v = (\mu_0 \epsilon)^{-\frac{1}{2}}$. This electrical permittivity is a tensor quantity which is defined as $D_i = \epsilon_{ij} E_j$ (where $E_j =$ electric field component). One such representation of this tensor for polar Kerr effect can be represented as:

$$\epsilon = \epsilon \begin{bmatrix} 1 & iQ_V m_z & 0 \\ -iQ_V m_z & 1 & 0 \\ 0 & 0 & 1 \end{bmatrix}, \quad (3.1)$$

Where m_z is out-of-plane magnetisation component, and Q_V is Voigt material constant, which in simple terms is the perturbation on the permittivity related to the refractive index. Its size decides the Kerr rotation effect, like its small size means small effect of Kerr rotation.

A linearly polarised light can be decomposed as right and left circularly polarised light. These components have different refractive indices which explain for their different velocity of propagation and different absorption in the materials. Due to this, there is a rotation in the real part and a phase shift (ellipticity) in the imaginary part as the light propagated through a material.

The Kerr effect can be expressed by the dielectric displacement as:

$$D = \epsilon(E + iQ_v m \times E) \quad (3.2)$$

Where E is the electric field vector associated with the incident radiation. m is unit vector of the sample magnetisation [122].

It can be explained from equation 2 that electric field associated with the incident light radiation interacts with the electrons of the sample under investigation. This results in propagation of oscillating current in a direction parallel to the polarisation. The term $m \times E$ in equation 3.2 represents the Lorentz force which explains for the deflection of electrons. This deflection provides the current a component perpendicular to the magnetisation and polarisation directions, so the reflected light that caused by the electric field is rotated and obtains an ellipticity.

3.4.2 Laser MOKE magnetometer

The laser MOKE system was used for sample characterisation of the magnetic hysteresis loop. Measurements were taken in a dark room using light from HeNe laser of wavelength 632 nm, and by a water cooled electromagnet with iron pole pieces the magnetic fields can be applied up to 550 mT. Figure 3.4 shows the main experimental setup used for polar MOKE measurements. The light made to pass through a polariser and directed by a mirror through a hole in one pole piece of the electromagnet. The polarised linear light interacts with electrons of the magnetised sample such that the reflected light has rotated polarisation. The reflected light is then passed through the analyser and is detected by a photo-detector. This produces a current, which is converted the photo-current into a voltage signal by the amplifier. The voltage signal can be read from a voltmeter or recorded as a function of the applied field using a computer to produce hysteresis loop.

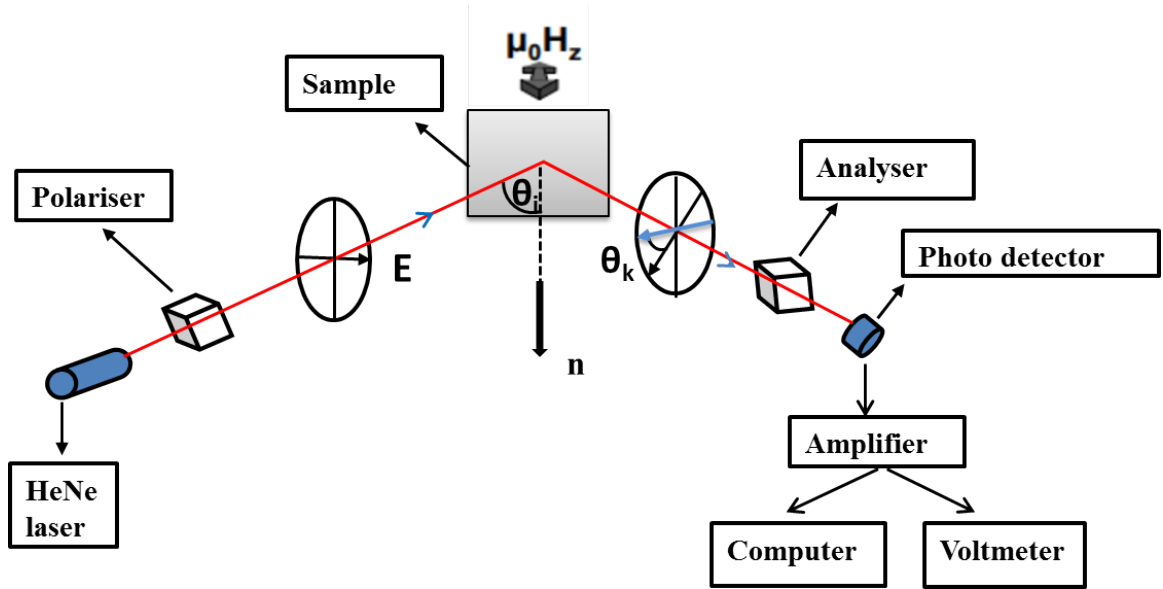


Figure 3.4: Pictorial representation of polar MOKE measurement system. It consists of main optical and electronic components which causes rotation of a polarised light on reflection from perpendicularly magnetised thin film. Both the polariser and the analyser are maintained at 90° to each other.

3.4.3 Wide-field Kerr microscopy

The Kerr microscopy was used to image the domain pattern and hysteresis loops in thin films which is based on the Kerr effect. Measurements were carried out in the polar MOKE geometry at room temperature. Depending on the type and magnification of the objective lens used, the microscope is able to create images with resolutions of micrometres or less. As seen in Figure 3.5.(a) linearly polarised light is used to measure changes in the magnetisation direction with the domains as changes in contrast of light. The analyser and the compensator in Figure 3.5.(b) polarised the light by 90° with reference to initial polarisation. This in turn isolates the signal whose intensity is measured by a photodiode detector or CCD camera. MOKE measurements are more sensitive to variations in magnetisation than to magnetisation absolute value.

Two types of Kerr microscopes are commonly used: wide-field Kerr microscope [9] and laser scanning microscopes [123]. Wide-field microscopes offer an

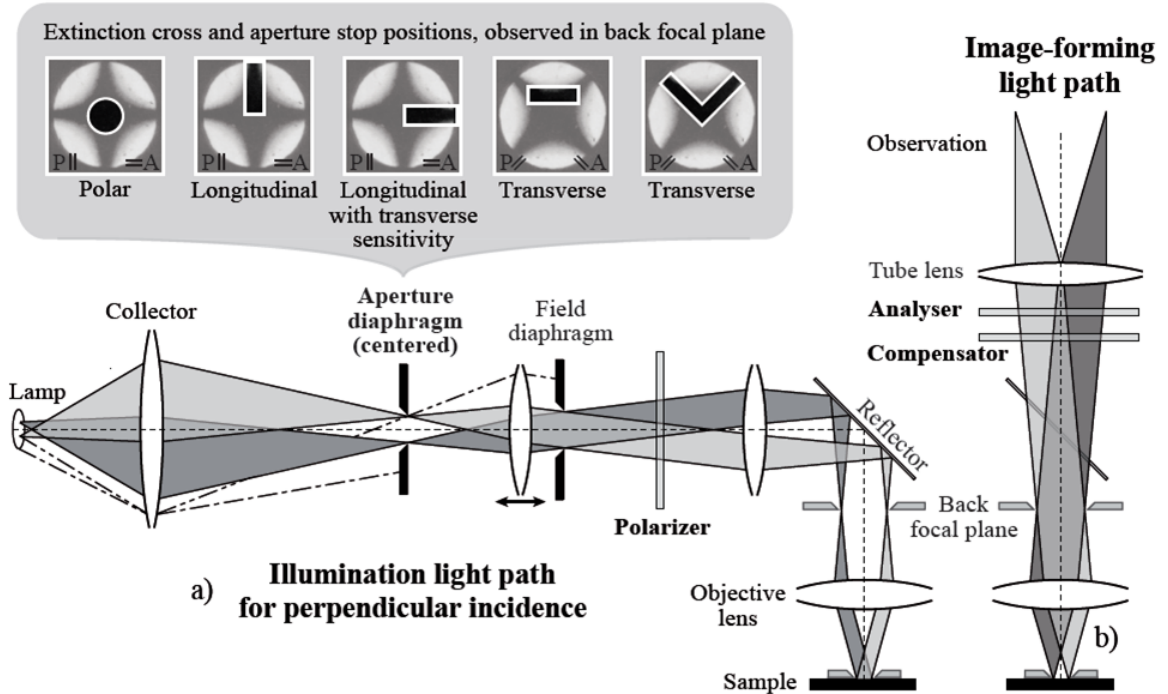


Figure 3.5: Light path and image formation in Kerr microscope. a) Light travelling from LED lamp is passed through a polariser to get reflected via objective lens and then fall on the sample. The Aperture diaphragm is monitored for selecting the polarisation region needed for polar, longitudinal and transverse Kerr measurement. b) The reflected light from the sample reaches the CCD camera for detection after passing [9].

image of a sample instantaneously, image the domain pattern at remanent state and take magnetic hysteresis loops. While laser scanning microscopy applied a laser spot to scan a certain area of a sample for building up the image. Hysteresis loops of the change in greyscale are also measured for whole image or a selected region. Moveable and rotatable sample stages with interchangeable electromagnets are powered by Kepco power supply. The magnetic coils which are perpendicular are water-cooled with no magnetic core or pole pieces. In this microscope, a white light LED is used through the optics to the sample. The light is reflected from the sample is detected using a camera and recorded on a computer. Also,

3.4 Magneto-optical techniques

the contribution intensity of light reflected from magnetic domains due to the Kerr effect.

To image the magnetic domains, the samples were prepared in a demagnetised state using an AC demagnetisation. Applying enough field between (300-500 Oe) to saturate the samples and once magnetised, the field was dropped to 0 Oe. A decay function is applied to the field to allow the oscillation between negative and positive Oersted fields at a frequency of 0.5 Hz for 120 seconds. The decaying field built up the deposition of up and down magnetisation states in the sample, producing domain wall formation at the up-down state interface. Since the samples demagnetised and domains formatting, a background image of the domain pattern was captured as shown in Figure 3.6.

Additional measurements were done at the University of Exeter using a very similar setting with a cooling stage, which allows to cool the samples and image the domains as function of temperature from (9-320)K.

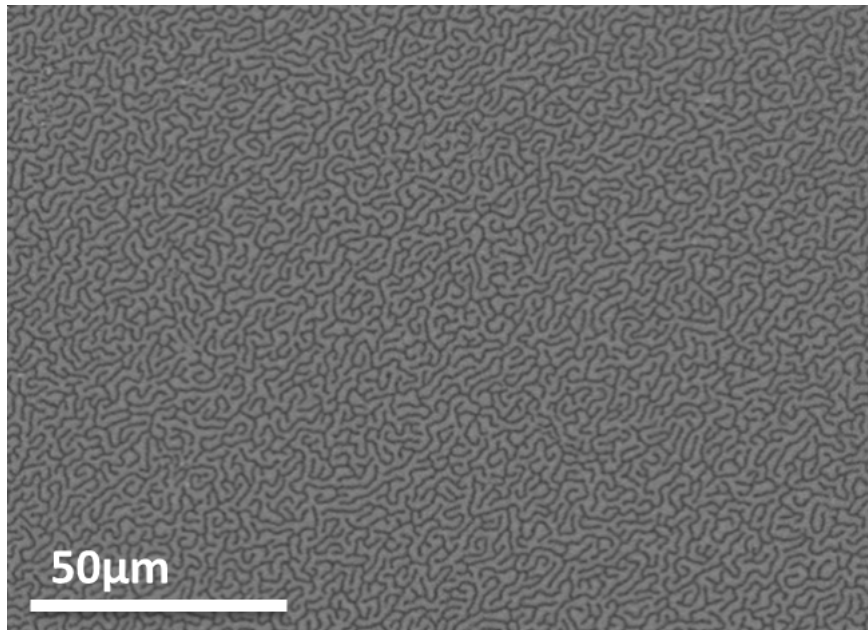


Figure 3.6: Domain pattern in a [Pt/CoFeB/Ir] \times 2 superlattice imaged by a wide-field Kerr microscope at room temperature, following AC demagnetisation.

3.5 Domain width method with image J

Image editing software, image J [124], was used to calculate the periodic domain width into the magnetic domain image. The domain images, in a demagnetised state, were thresholded to perform a fast Fourier transform (FFT) to determine the most commonly occurring domain width.

The domain width method is used to study the relationship between domain period and domain wall energy density as a function of temperature dependence in order to obtain the Dzyaloshinskii-Moriya interaction (DMI). There are several steps of image editing have done prior to perform FFT. Firstly, the raw domain image was inserted in the image J software and cut 300x300 pixel squares to get a representative spread of data. The type of pixel square was converted from 8 bit to 32 bit image to interactively alter the brightness of the image. A background image of the order 250 pixels was subtracted from the domain image, using the sliding paraboloid function to enhance contrast. Convolve and Gaussian blur filters were applied to eliminate any grainy textures in the image. Lastly, a black and white threshold image was applied to maximise the efficiency of the FFT as shown in Figure 3.7.

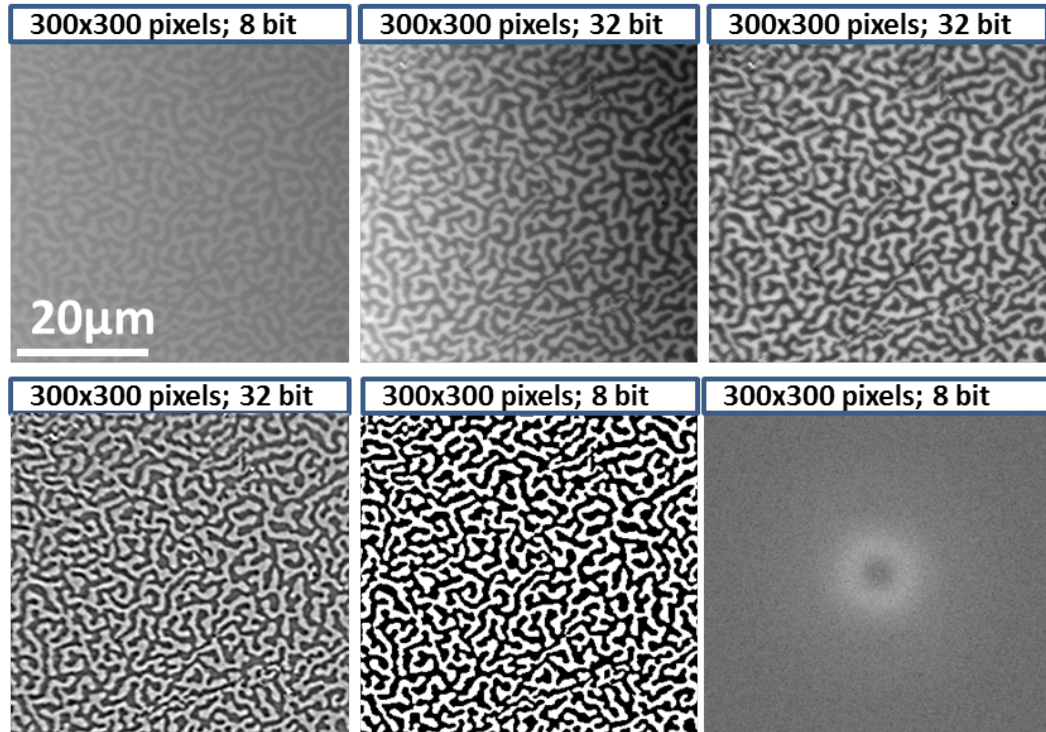


Figure 3.7: Magnetic domain of CoFeB image was edited, image J, to produce the FFT. a) A raw image inserted and cut 300x300 pixels with 8 bit, converted the image from 8 bit to 32 bit to increase threshold sensitivity, subtracted the background to improve contrast. b) Convolve and Gaussian blur filters were applied to remove any grainy textures, threshold image to increase the efficiency of the FFT, Fourier transform of the domain image.

Since the image successfully thresholded and a FFT applied, the domain image can be converted to circular intensity peaks (Figure 3.8.(a)). The middle band of the inner ring was isolated and used to plot a graph which contains intensity against pixel distance in FFT space (Figure 3.8.(b)).

The two intensity peaks in Figure 3.8.(b) are characteristic of the most typical domain size. To obtain the domain size, the raw data of the intensity peaks of FFT have to be scaled to the pixel's true size. The two peaks position was fitted to a Gaussian function to find the centre of the intensity peaks as shown in Figure 3.9. The different between two peaks was calculated and divided by 2

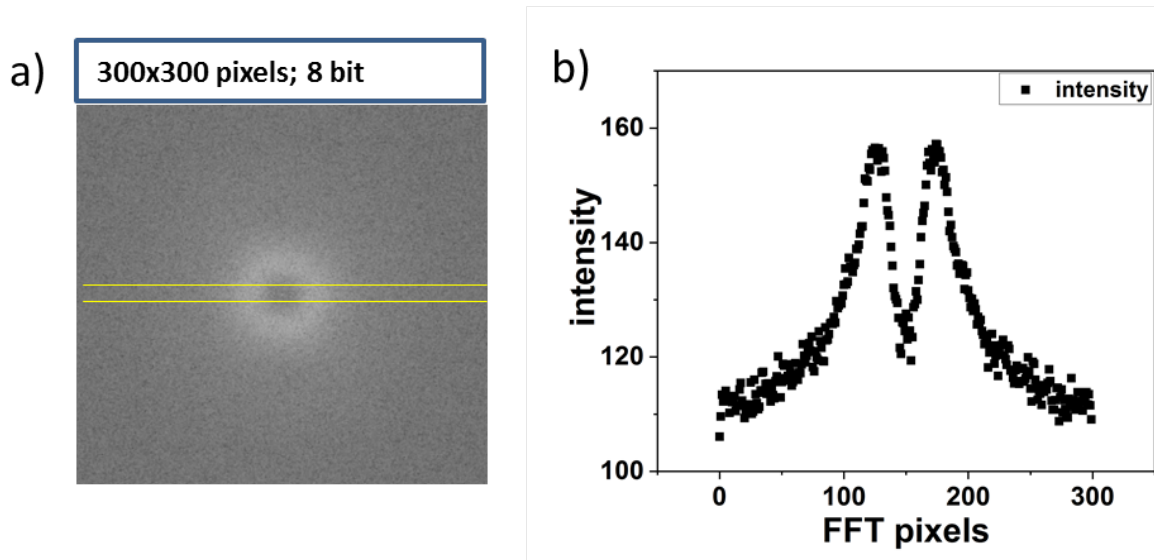


Figure 3.8: An area is spanned across the transformed image to plot intensity peaks for all sides of the ring. b) The intensity peaks of the Fourier transform for greyscale value against distance.

to find the distance of FFT in reciprocal space. Then the distance was divided by the dimension of the FFT image, of 300 pixels, and transformed back into real space. The scale bar for the image was divided by the length of scale bar to convert the unit of the real space distance from pixel^{-1} to μm^{-1} . Finally, the domain period (d) was determined from the inverse of the peak distribution in the FFT.

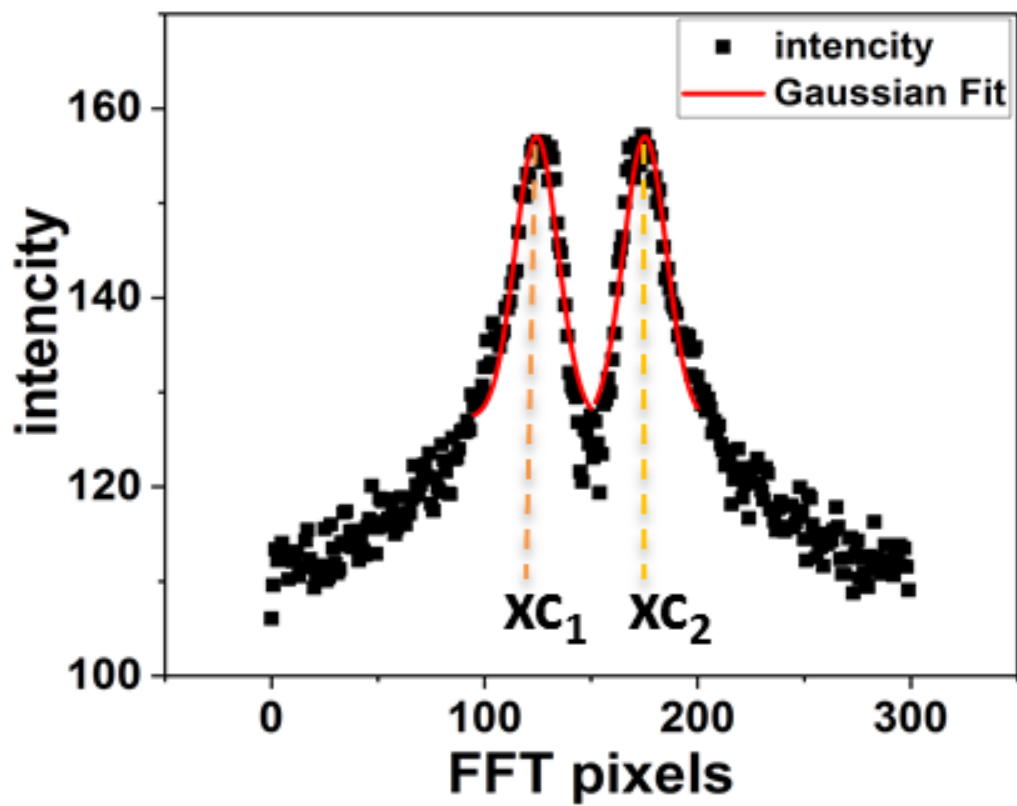


Figure 3.9: Gaussian fit to the radial peaks intensity of the Fourier transform to extract the domain size.

3.6 SQUID VSM

A superconducting quantum interference device (SQUID) [125] with high sensitivity of 10^{-8} emu is used to measure the moments of samples with small moments. Multilayered systems with perpendicular magnetic anisotropy (PMA) where the ferromagnetic (FM) layer is very thin have moments of the order 10^{-5} - 10^{-6} emu. Moreover, the SQUID-VSM system is used in this thesis capable of measuring samples over a range temperature (1.7K to 1000 K) and applied fields up to 7 T. The samples are placed through a system of superconducting detection coils, which are inductively coupled to a SQUID as shown in Figure 3.10. While the sample is vibrated up and down in the sample chamber, the current is generated due to the varying magnetic signal via Faraday's law.

In the absence of external magnetic field, the input current splits equally into the two junctions of the SQUID. However, when there is stray magnetic field from a sample, a screening current, I_s , flows in the superconducting loop generating a magnetic field that cancels the external flux. Since the screening current is circulating in a loop, it increases the magnetic flux and the junctions become momentarily resistive. The fluctuations of the current in the detection coils, correlates with the change in magnetic flux and produces an output voltage across the junction which is proportional to the magnetic moment of the sample.

In this system, hysteresis loops have been obtained by measuring magnetic moments at different field values. Magnetisation loops have been measured as a function of temperature (5- 380) K to obtain the effective anisotropy and exchange stiffness for different substrates.

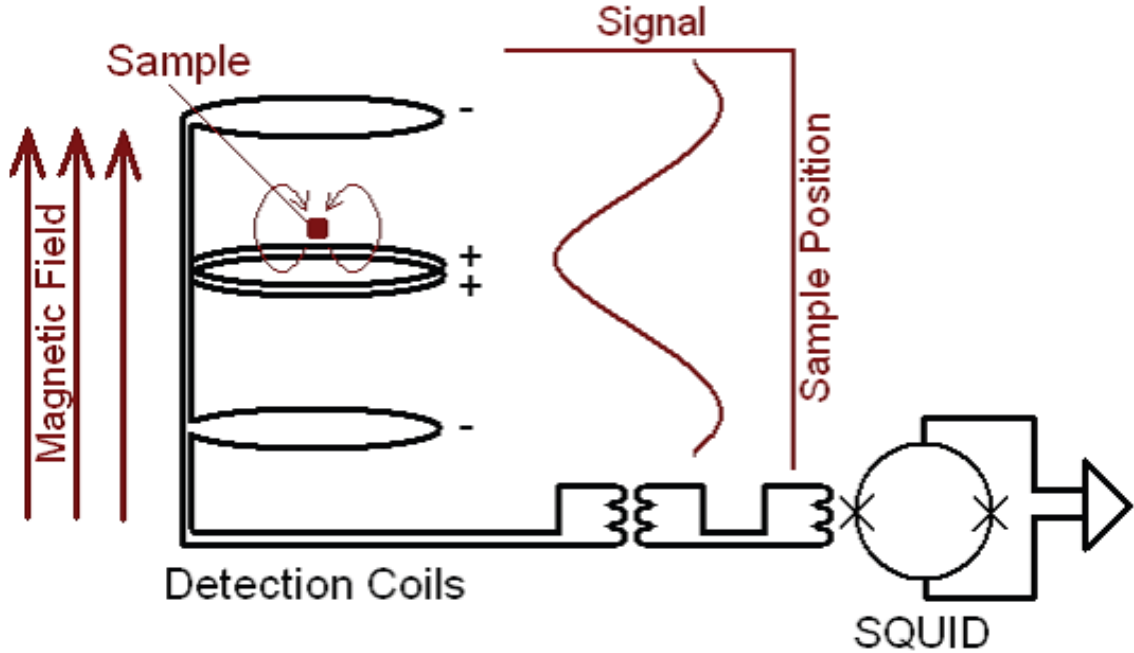


Figure 3.10: The configuration of the detection coils principle of a SQUID-VSM. The signal generated in the detection coils which are inductively coupled to the SQUID [10].

3.7 Magnetoresistance measurement technique

Transport measurements (Hall Voltage) are conducted to obtain the anisotropy field ($\mu_0 H_k$). The samples are wire-bonded on each edge (square-cut) as shown in Figure 3.11.(a). On sending current through the sample a voltage drop appears perpendicular to the current due to the Extraordinary Hall effect EHE on application of magnetic field. Constant external magnetic field (500 mT) is applied perpendicular to the current which is initially out of plane. The sample is rotated from -180° to $+180^\circ$ in 5° steps from the sample easy axis, with the rotation axis parallel to the current flow. By normalising the data and fitting a parabola (cosine), the anisotropy field can be determined [11] as shown in Figure 3.11. (b).

3.7 Magnetoresistance measurement technique

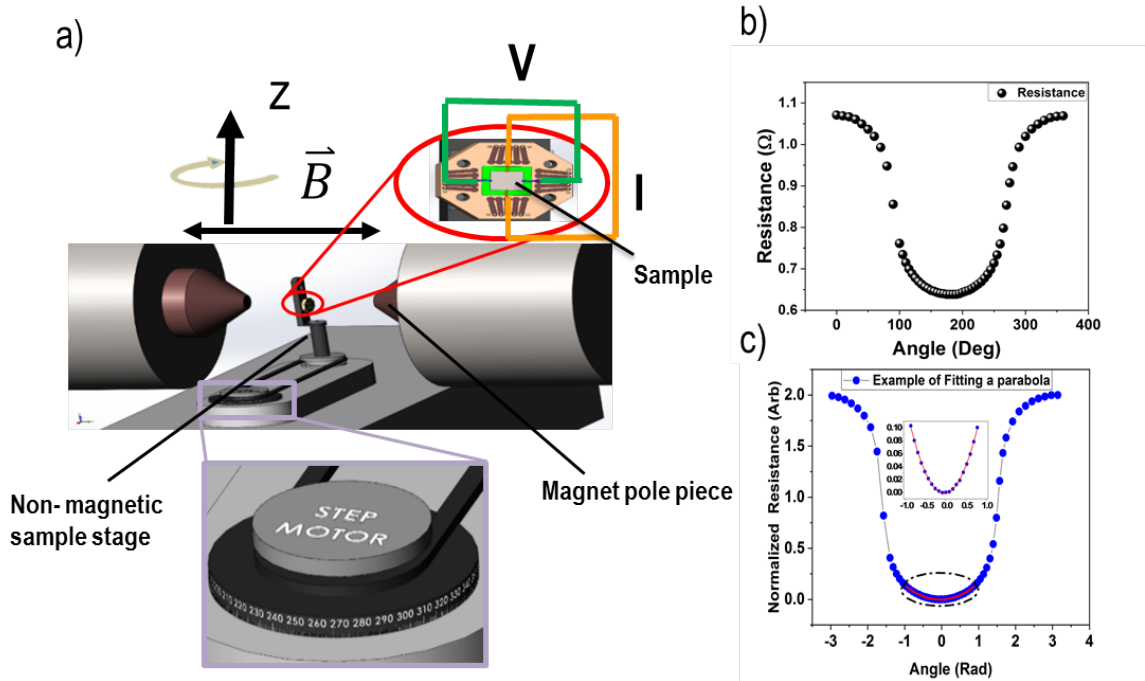


Figure 3.11: A diagram of the set-up for EHE measurements. The new system has been automated such that the measurement software is able to rotate the sample and collect whole measurements. b) The raw resistance before normalisation and as the magnetisation follows cosine law on rotation the resistance has normalised[11]. c) Normalising the data and fitting a parabola to obtain the anisotropy field.

3.7.1 Extraordinary Hall Effect (EHE)

In order to measure the change in PMA thin films magnetic properties in room temperature, two techniques sensitive to perpendicular magnetisation were adopted. The polar MOKE and Extraordinary Hall effect (EHE) are both indirect measures of the magnetisation perpendicular component. Both can be utilized to measure out-of-plane hysteresis loops and, in case an in-plane field is applied to rotate the magnetisation from the easy axis to hard axis, to measure PMA field. MOKE can also be utilized to capture magnetic domains with a wide-field Kerr microscopy.

3.7 Magnetoresistance measurement technique

The EHE, also known as the anomalous Hall effect (AHE) is a phenomenon of an electron transport. The geometry of Hall measurements necessitates passing a current into a conducting material and the voltage to be measured through the material, in a perpendicular position to the current flow. An out-of-plane magnetic field is applied perpendicularly to both the voltage measurement and the current flow. Up and down spins are differently scattered so that charge is formed along wire sides. A water-cooled electromagnet that has iron poles pieces is used to apply magnetic field, and the applied fields can reach 0.9 T. The sample sits on a rotatable stage in a way allowing the field to be applied in-plane or out-of-plane. Currents of ± 1 mA passing through the sample and measured voltage for each point, is converted to a resistance. The Hall resistance can be represented phenomenologically as the following:

$$R_H = (R_o H_z + R_E M_z) / t \quad (3.3)$$

Where R_o refers to the ordinary Hall coefficient, H_z refers to the external magnetic field, R_E refers to the EHE coefficient, M_z is the out-of-plane magnetisation and t is the thickness. The first term refers to the ordinary Hall effect with the second term resulting from the extraordinary Hall effect, discovered in 1879 by Edwin Hall [126].

In the ordinary Hall effect, a Lorentz force deflects charge carriers while charge carriers move through the material in the perpendicular magnetic field. While the ordinary Hall effect is mainly based on density of carrier and is not limited on magnetic materials, the EHE only takes place in Ferromagnets and is still under research [127]. Opposite spin of charge carriers are scattered in opposite direction.

Thus, scattering can be caused by interactions linked to their Berry's phase curvature, resulting an 'intrinsic' contribution, or by interactions linked to the material disorder, resulting the skew scattering 'extrinsic' contributions and side-jump. Skew scattering deflects an electron according to its spin-orbit coupling with an impurity, while side-jump deflects is based on the electric fields detected by electrons while they move towards and outwards from impurities [127]. The AHE has been used to measure the component of the magnetisation pointing out

3.7 Magnetoresistance measurement technique

of plane. The perpendicular anisotropy was measured by monitoring the signal of EHE while the magnetisation is pulled from out-of plane to in-plane.

3.7.2 Anisotropy Measurements of Pt/Co(Fe)B/Ir

In measuring the Pt/CoFeB/Ir and Pt/CoB/Ir multilayers perpendicular anisotropy, a technique, developed by Moon et al. [11], based on the extraordinary Hall effect is used. This technique is based on the Stoner-Wohlfarth model and can be applied in thin films possessing a strong intrinsic signal. Various factors make it challenging to calculate PMA with bulk techniques like torque magnetometry and ferromagnetic resonance. Some of the factors include small volume and magnetisation reversal behaviours that arise due to the competing nucleation-dominated processes and domain-wall motion. Such factors result in a weak signal that is challenging to be detected. However, there is a possibility of preserving a strong signal in magnetic thin films through monitoring extraordinary Hall voltage at small angle deviations, thereby making it possible to measure magnetisation state and extract the anisotropy field. The magnitude of the EHE resistance provides a measure of the magnetisation component that points out of the plane and can be applied in the determination of PMA [128].

If the magnetic system exhibits uniaxial magnetic anisotropy, the Stoner-Wohlfarth equation for magnetic energy (E) can be expressed as follows:

$$E = -K_u \cos^2 \theta - M_s H \cos(\theta - \phi_H) \quad (3.4)$$

where K_u is uniaxial anisotropy, H is the external field, θ is the magnetisation angle and ϕ_H is the angle of the external field from the easy axis, normal to the film [11]. The equation below is rewritten as follows after it has been normalised by K_u :

$$\epsilon = \frac{E}{K_u} = -\cos^2 \theta - 2\alpha \cos(\theta - \phi_H) \quad (3.5)$$

where $\alpha = M_s H / 2K_u$ and the equilibrium angle of magnetisation can be found by differentiating with respect to θ :

$$\sin 2\theta + 2\alpha \sin(\theta - \phi_H) = 0 \quad (3.6)$$

3.7 Magnetoresistance measurement technique

This equation 3.6 gives solutions for the magnetisation angle with respect to α and ϕ_H . With a focus on small angles, the solutions for $\theta \sim 0$ and $\phi_H \sim 0$ can be determined using a Fourier series expansion. Due to symmetry, the solutions of $\theta \sim 0$ and $\phi_H \sim 0$ are readily deduced. The following is the result of the Fourier expansion:

$$\cos \theta = 1 + A_2 \phi_H^2 + A_4 \phi_H^4 + A_6 \phi_H^6 + \dots \quad (3.7)$$

Due to the fact that the higher order coefficients are negligibly smaller than A_2 . The solution can be rewritten as $\cos \theta = 1 + A_2 \phi_H^2$ and the Fourier coefficient A_2 can be calculated as follows:

$$A_2(\alpha) = \frac{\alpha^2}{2!(1 + \alpha)^2} \quad (3.8)$$

As a result, it is quite appropriate to refer to the asymptotic solution as:

$$\cos \theta \simeq \frac{(M_s H)^2}{2(2K_u + M_s H)^2} \phi^2, \quad (3.9)$$

for ϕ_H in a wide range. To prevent magnetisation reversal in the multilayer sample, the sweeping angle ϕ_H is restricted to a maximum of 5.

The Hall effect was used to experimentally determine the angle of magnetisation θ . Each edge of a square-cut sample was wire bonded, with one pair attached to a current source provided by a Keithley 2400 sourcemeter and the remaining pair connected to a Keithley 182 nanovoltmeter for Hall voltage measurement. The sample is mounted on a holder and rotated in the constant external field. Upon a constant current flow of 1 mA, the Hall effect induces a transverse electric voltage. The Hall voltage is given as:

$$V_H = R_o I H_z + R_a I M_z, \quad (3.10)$$

where is R_o the ordinary Hall coefficient, R_E is the extraordinary Hall coefficient and I is the current flow across the sample. Thus, the out-of-plane components of external field $H_z = H \cos \phi_H$ and magnetisation $M_z = M_s \cos \theta$ are detected by the voltage probes.

In measuring the dependence of the sweeping angle (ϕ_H) on the magnetisation angle (θ), a 500 mT constant external field is applied normal to the film. Then,

the sample is followed by 5° rotation increments with the rotation axis of the film, parallel to the current flow. In this procedure, the ordinary Hall voltage is easily subtracted. The ordinary Hall Effect creates a signal that is proportional to $H \cos \phi_H$ during one sweep between -180° to 180°, with the amplitude is linearly dependent on the external field. Thus, the subtraction of the ordinary Hall voltage can exactly be done when various applied fields are measured. However, the ordinary Hall Effect is negligible in realistic cases since its way smaller as compared to the extraordinary Hall effect because $R_o \ll R_E$ and $H < M_s$. Lastly, $\cos \theta$ is readily calibrated after normalisation with the expression, relation

$$\cos \theta = \frac{\{2V_H - (V_{H \max} + V_{H \min})\}}{(V_{H \max} - V_{H \min})} \quad (3.11)$$

where $V_{H \max}$ represent the minimum and maximum values of the V_H in measuring one sweep. A plot of normalised extraordinary Hall voltage against the sweeping angle (ϕ_H) as shown in Figure 3.11(b) allows extraction of a quadratic equation from the data points around the minimum value. The data is picked at the maximum values of ± 180 , followed by between 60° in 5 increments. This makes it possible to obtain the Fourier coefficient A_2 as well as the calculation of anisotropy field H_k from A_2 by applying equation:

$$H_k = \frac{2K_u}{M_s} = H \frac{1 - \sqrt{A_2}}{\sqrt{2A_2}} \quad (3.12)$$

3.8 Piezoelectric transducers

Upon deposition of appropriate Pt/CoFeB/Ir and Pt/CoB/Ir on thin glass substrates, they were characterised and then attached to piezoelectric transducers in order to measure the magnetic properties under strain. The thin-film glass substrates were bonded to transducers through the epoxy resin. Then the samples were heated in a tube furnace for one and a half hours at 80°C to cure the resin. The transducers applied in this research: biaxial is represented in Figure 3.12. The transducers are formed from PZT, which is a piezoelectric ceramic that generates a voltage upon the distortion of the material structure [129]. The converse piezoelectric effect is applied in straining the samples investigated in this work,

and the transducers can be made to contract or expand by applying voltage, as shown in Figure 3.13. There is an approximately linear relationship between the expansion and applied voltage so that the material can be strained through an application of a voltage, followed by the removal of the strain to make the material regain the original length. However, as can be observed in Figure 3.14, there exists a small hysteresis in the characteristic of the voltage strain. A single PZT is used in making biaxial transducers, with the electrodes located on the two shorter sides. In Figure 3.13, the positive voltage application expansion is along the biaxial transducers' short axis. While the transducer's specified voltage range is 0 to 150 V, the thickness of the biaxial transducers is 2 mm and increases by up to 2.2 m at a voltage of 150 V resulting in a maximum uniaxial strain of $\delta t/t$ less than 0.1 %. The value represents the strain generated in a free transducer. However, bonding the glass substrate to either side of the transducer can lead to a clamping effect, hence barring maximum expansion. The implication is that effective transmission of the strain through epoxy resin layers, a glass substrate, and the Ta/Pt to reach the CoFeB/CoB. The following section detail the measurement of piezo-voltage to Pt/CoFeB/Ir and to Pt/CoB/Ir strain characteristics.

3.8.1 Strain characterisation

The strain occurring in a metal relates to the change in resistance. The resistance $R = V/I$ of a Pt/CoFeB/Ir and Pt/CoB/Ir can be obtained through the passing of a current and taking the voltage reading between the two parallel cross structures. Voltage was obtained using a Keithley 182 nanovoltmeter when a current of 1mA was applied using a Keithley 2601. The application of a voltage to the piezoelectric leads to a change in the thin film's width and thickness, as demonstrated in Figure 3.13.

The strain can be measured from the change in resistance of the thin film, represented by differentiating of following equation:

$$R = \rho l/A \quad (3.13)$$

where R is the resistance, ρ is the resistivity, l is the length and A is the cross-sectional area. However, in the event that there is a strain in the thin film, other

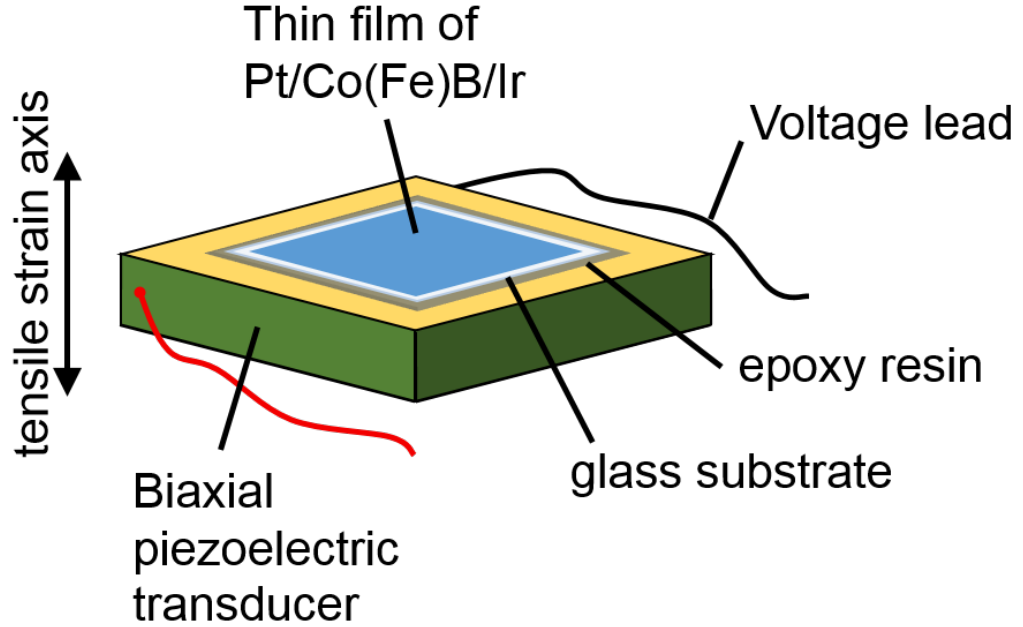


Figure 3.12: Thin film of Pt/Co(Fe)B/Ir deposited on glass substrate and attached with epoxy resin on biaxial piezoelectric transducers.

effects come into play. For example, resistivity may vary with the distortion of the material's structure, and the cross-sectional area may also vary by the quantity dictated by Poisson's ration (ν). We can obtain an equation that related the resistance change and dimension change by differentiating equation 3.13. The resulting equation takes account of A and ρ . By dividing through by R , equation 3.14, which represents resistance proportional change, is obtained.

$$\frac{\delta R}{R} = \frac{\delta \rho}{\rho} + \frac{\delta l}{l} - \frac{\delta A}{A} \quad (3.14)$$

It can be expressed in terms of strain or change of proportional length $\varepsilon = \frac{\delta l}{l}$

$$\frac{\delta R}{R\varepsilon} = \frac{\delta \rho}{\rho\varepsilon} + \frac{1}{\varepsilon} \left(\varepsilon - \frac{\delta A}{A} \right) \quad (3.15)$$

$$\frac{\delta R}{R\varepsilon} = \frac{\delta \rho}{\rho\varepsilon} + \left(1 - \frac{\delta A}{A\varepsilon} \right) \quad (3.16)$$

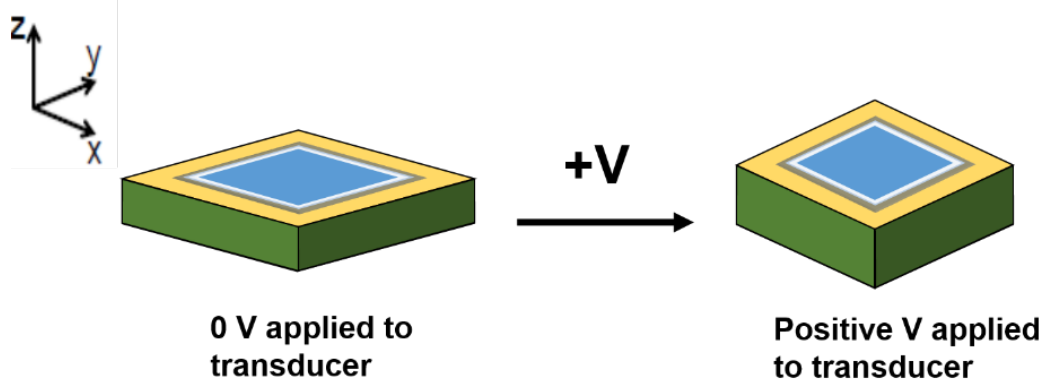


Figure 3.13: The diagram shows the effect of the biaxial piezoelectric transducer. When the voltage is increased, the transducer contracts in the x-y plane and expands in the z-direction, perpendicular to the plane of the thin film. The transducer reaches a maximum compression biaxial strain at 150V.

with the second term on the right being a geometrical deformation $C_{geo} = \left(1 - \frac{\delta A}{\varepsilon A}\right)$ description while the first term on the right being the strain coefficient of specific resistivity $C_\rho = \left(\frac{\delta \rho}{\rho \varepsilon}\right)$ which has been determined by Kuczynski [130] as 0.84 for Co and 2.60 for Pt. The strip of Pt/Co, coupled to a transducer strain, can then be obtained from the variation to resistance

$$\varepsilon = \frac{\delta R}{R} \frac{1}{C_{geo} + C_{\rho Pt/Co}} \quad (3.17)$$

with $C_{\rho Pt/Co} = 1.72$, being the average of the Co and Pt and values. Next is calculating the biaxial transducers' geometrical factors.

3.8.2 Biaxial transducers

The geometrical factor calculated for the biaxial transducers from

$$\frac{\delta A}{A} = \frac{\delta t}{t} + \frac{\delta w}{w} = \varepsilon_x - \frac{1}{\nu_z} \varepsilon_x \quad (3.18)$$

$$geometrical = \frac{1}{\varepsilon} \left(\varepsilon - \frac{\delta A}{A} \right) = \frac{1}{\varepsilon_x} \left(\varepsilon_x - \left(\varepsilon_x - \frac{\varepsilon_x}{\nu_z} \right) \right) = \frac{1}{\nu_z} \quad (3.19)$$

The Poisson ratio of the film is assumed to be $\nu_z = 0.3$, which is typical for all metallic alloys [131].

$$\varepsilon_x = \frac{\partial R}{R} \left(\frac{1}{(1/0.3) + 1.72} \right) = \frac{\partial R}{R} 0.2 \quad (3.20)$$

While the strain in the y and z directions can be calculated from

$$-\frac{1}{\nu_z} \varepsilon_x = -\frac{1}{\nu_z} \varepsilon_y = \varepsilon_z \quad (3.21)$$

Figure 3.14 demonstrates the calculated strain and resistance against biaxial transducer applied voltage with the [Pt/Co(Fe)B/Ir]_n thin film with different repeats (n =1,2,5,7,10). From the measurement, there is an elongation along z (out-of-plane) with the corresponding in-plane compression. All the samples with different repeats have a measured maximum strain between $\sim 9 \times 10^{-4}$ and 1×10^{-3} which is consistent with the estimated stain in the transducer at the voltage of 1×10^{-3} .

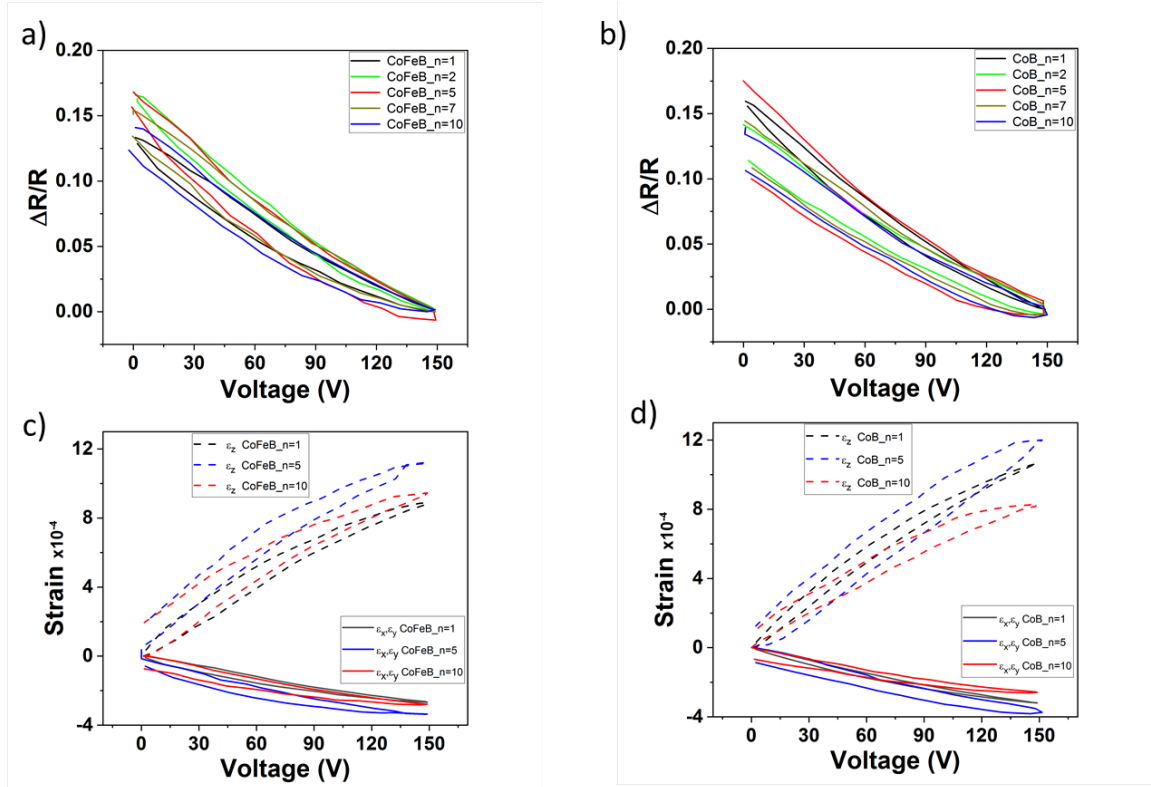


Figure 3.14: a) and b) show the resistance of Pt/CoFeB/Ir and Pt/CoB/Ir with different repeats against transducer voltage. c) and d) present the strain calculated from the change in resistance of Pt/CoFeB/Ir and Pt/CoB/Ir on biaxial transducers plotted against transducer voltage. The voltage was swept from 0 V then to 150 V and back to 0 V.

3.9 Summary

The magnetic properties of Pt/Co(Fe)B/Ir multilayers have been deposited by dc magnetron sputtering. The thickness of the samples were validated by low angle scan XRD measurements. Polar laser MOKE measurements showed out of plane magnetisation. The Kerr microscopy with a cooling stage at university of Exeter was used to image the domain pattern as function of temperature. Domain image was edited by using image J software to calculate the domain size. All the samples with different repeats have a measured maximum strain

3.9 Summary

between $\sim 9 \times 10^{-4}$ and 1×10^{-3} which is consistent with the estimated stain in the transducer at the voltage of 1×10^{-3} . The following Chapters describe the samples characterisation and measurement of Pt/Co(Fe)B/Ir in more details and present results of the hysteresis loops, anisotropy measurements, maze domain images, exchange stiffness effected by temperature and the calculations of DMI .

CHAPTER 4

Sample characterisation

4.1 Introduction

This chapter presents results of multilayers of Ta/[Pt/CoFeB/Ir]_n/Pt and Ta/[Pt/CoB/Ir]_n/Pt with perpendicular magnetic anisotropy grown on SiO_x substrates. Laser MOKE and Kerr microscopy have been used to investigate the hysteresis and domain morphology of the multilayers. Kerr microscopy shows the domain size as function of ‘n’ and temperature. The magnetic anisotropy is measured using a technique based on the extraordinary Hall effect. In combination with SQUID measurements, the saturation magnetisation and effective anisotropy can be obtained, this allows to estimate the exchange stiffness. Lastly, the DMI at room temperature has been obtained by utilising a model for the equilibrium domain size in magnetic multilayers.

4.2 Sample structure

The samples measured were Ta/[Pt/CoFeB/Ir]_n/Pt and Ta/[Pt/CoB/Ir]_n/Pt grown on a thermally oxidised Si substrate deposited by dc magnetron sputtering, where n is the number of repeats of the Pt/CoFeB/Ir or Pt/CoB/Ir trilayer, as shown in Figure 4.1. The base pressure reaches 2.4×10^{-8} Torr with use of a cryo-pump in combination with a liquid nitrogen trap. Once the pressure in a sputtering chamber is low enough, Ar gas will be introduced into the system with a partial pressure of 2.5×10^{-3} Torr.

The interfacial Dzyaloshinskii-Moriya interaction (DMI) at the interface of a 5d metal and a thin film 3d ferromagnet (like Pt/Co or Pt/CoFeB) leads to chiral domain walls and skyrmions. These topological spin textures are promising for the development of low power magnetic memory devices [132]. The substrate on which the thin film is grown on is chosen to directly affect the crystallographic or magnetic properties of the film. Ta is used as a seed layer to smooth the surface and nucleate the correct crystal texture. As Platinum nucleus is massive, it was selected as a bottom layer, and we know it is textured [111] on Ta, which is the crystallographic ordering required for PMA in Pt/Co. The top layer of Pt was attached as a cap layer to prevent the oxidation of the samples in ambient air. Ir was used as a heavy metal to break inversion symmetry in the system. With the

4.2 Sample structure

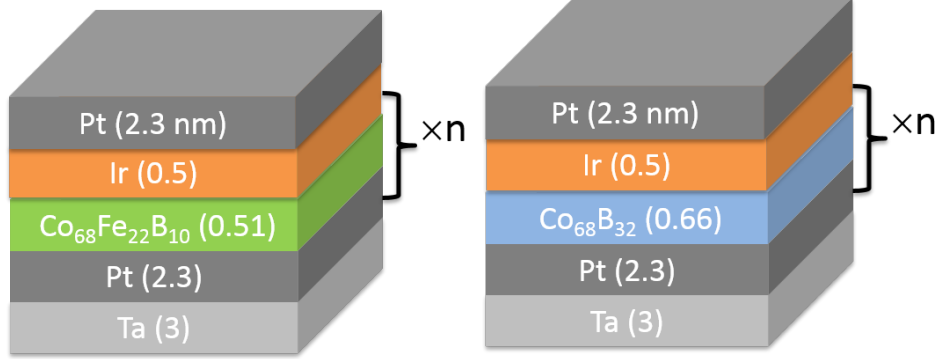


Figure 4.1: Schematic of sample structure and dimensions of the Ta/[Pt/CoFeB/Ir]_n/Pt and Ta/[Pt/CoB/Ir]_n/Pt magnetic thin films were grown on SiO_x substrates. Here, the layer thicknesses are displayed in nm and ‘n’ is the number of Pt/CoFeB/Ir or Pt/CoB/Ir layers in the thin film.

increase of the layers numbers, the base becomes less flat for the next multilayer because of the introduction of roughness at each interface. This means the more number of layers increases, the magnetisation and anisotropy decrease. Also, the objective to obtain continuous ultrathin layers which are magnetically soft, Co was used as the base magnetic material as Co has a large magnetic anisotropy [133]. Once deposited by magnetron sputtering, it is polycrystalline in nature. Due to its polycrystalline nature, the grain boundaries will act as defects, and therefore pinning domain walls at these grain boundaries. Therefore, to remove the effects of pinning sites on the domain wall motion, we require amorphous magnetic materials, such as the CoB which retains the large magnetic anisotropy of the Co base material or the magnetically soft CoFeB, with a lower anisotropy. Two series of samples were grown on SiO_x in order to achieve the optimal PMA for the magnetically hard CoB and the magnetically soft CoFeB will be discussed, as described below:

- 1- Ta(3nm)/[Pt(2.3nm)/Co₆₈Fe₂₂B₁₀(0.51nm)/Ir(0.5nm)]_n/Pt(2.3nm)
n=1,2,5,7,10,12,15,20
- 2- Ta(3nm)/[Pt(2.3nm)/Co₆₈B₃₂(0.66nm)/Ir(0.5nm)]_n/Pt(2.3nm)
n=1,2,5,7,10,12,15,20

4.3 Polar Laser MOKE

Polar hysteresis loops were used for Pt/CoFeB/Ir and Pt/CoB/Ir multilayers with different repeat of Pt/CoFeB/Ir or Pt/CoB/Ir. The polar hysteresis loops give an insight into the magnetic properties of coercive field and remanent magnetisation. The magnetic properties of the films showed out-of-plane magnetisation in each of the samples. Eight samples for each CoFeB and CoB with between $n = 1$ and $n = 20$ were taken hysteresis loops.

4.3.1 Ta(3nm)/[Pt(2.3nm)/Co₆₈Fe₂₂B₁₀(0.51nm)/Ir(0.5nm)]_n /Pt(2.3nm)

CoFeB was chosen as a similar material to CoB, but is known to be more magnetically soft [134]. As such, we can compare the effect that an applied strain has on the DMI directly and gain an understanding of the underlying mechanism. Using CoFeB the hysteresis loops are very different in shape compared to CoB. They have more wasps like shape to the hysteresis loops as shown in Figure 4.2. In CoFeB wasp waisted hysteresis appeared at $n \geq 2$, whereas for the CoB system, they appear at $n \geq 7$. The remanent magnetisation becomes smaller when the repeats increase as we see in parts (d) of Figure 4.2. The coercive field is not a very good way of comparing these sets of samples particularly in large n , due to a different reversal process of the shape of the loops. The first part of switching is different, it's shallow for CoFeB and steeper for CoB.

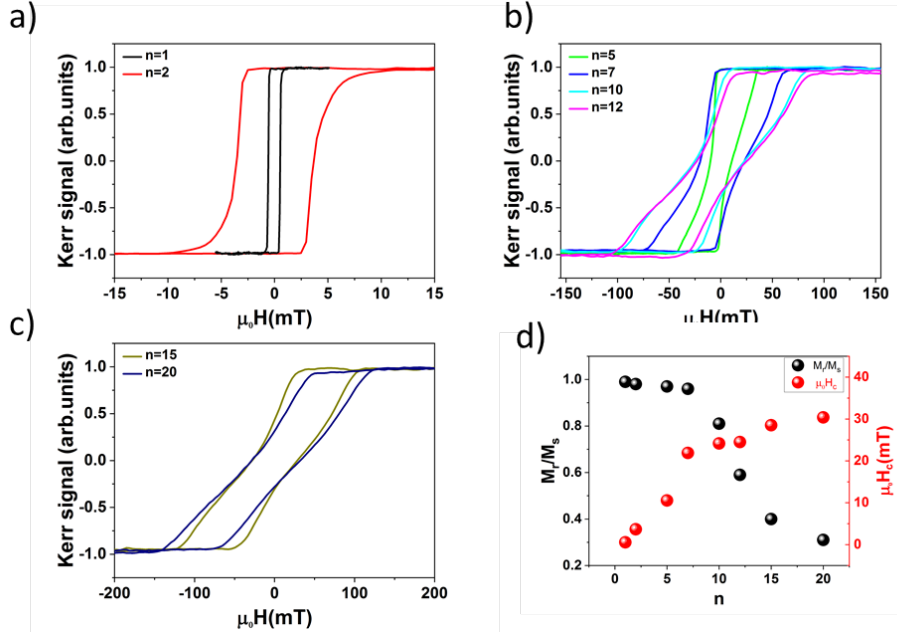


Figure 4.2: Polar MOKE hysteresis loops for Ta/[Pt/CoFeB/Ir] $_n$ /Pt with different repeats. a) At ($n \leq 2$) shows square hysteresis loop and sharp switching. b) As the number of layers increases ($2 < n \leq 12$) the hysteresis loops have a wasp shape due to changes in magnetic layers. c) As the number of repeat increases further ($15 \leq n \leq 20$) the saturation field increases, which leads to decrease of remanence. d) The remanent magnetisation and the coercive field, which shows high coercive fields and less remanent magnetisation when the repeats are increased.

4.3.2 Ta(3nm)/[Pt(2.3nm)/Co₆₈B₃₂(0.66nm)/Ir(0.5nm)] $_n$ /Pt(2.3nm)

The Pt/CoB/Ir has two distinct types of hysteresis loops. Square hysteresis loops for $n \leq 5$ and wasp like hysteresis loops for $n > 5$ due to the changes of the thickness or roughness as shown in Figure 4.3. Also due to the increase of roughness, the remanence correspondingly becomes smaller with n and the saturating field increases with n as loops become wasp like. Previous studies on Co-based PMA multilayers have linked this wasp like shape with an accumulation

of defects within the multilayer, causing the superlattice to no longer be uniform after a certain number of repeats [135][136]. Future AFM studies of the complete structure would be useful to see if we can link the surface roughness to the wasp like shape [136].

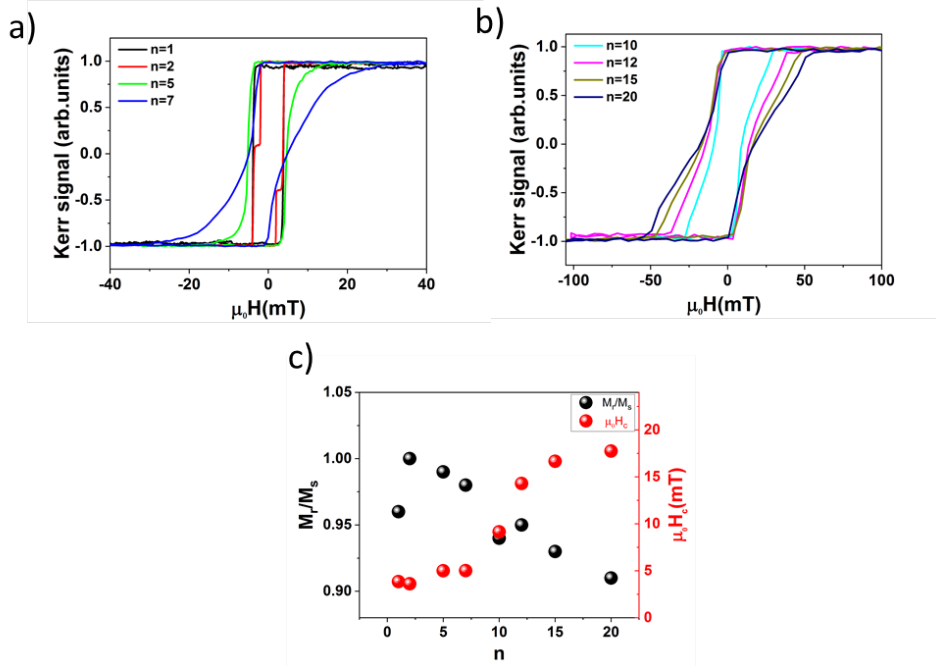


Figure 4.3: Out of plane MOKE for Ta/Pt/CoB/Ir/Pt structures with different repeats. a) The hysteresis loops are square and exhibit sharp switching until $n \leq 5$ repeats and started a wasp like from $n \geq 7$. b) Above $n \geq 10$ repeats the hysteresis loops are no longer switching in a single steps. c) Change of coercive field and remanent magnetisation of Pt/CoB/Ir structures with different repeats.

For both systems, a small number of multilayers, for instance ($n \leq 2$), the hysteresis loops are narrow and square shaped and the coercive field is small. Therefore, the narrowness of the hysteresis loops emerges and a small external field is needed to reverse the magnetisation of the sample. Increasing the number of layers into ($5 \leq n \leq 12$), the hysteresis loops become less square and have a wasp shape due to increased pinning of domain walls. The wasp like shape is due to changes in magnetic layers as number of repeats are increased and the

reversal process is changing due to large demagnetising field. As the number of layers arises, the interface roughness increases leading a local difference in the perpendicular anisotropy while also expanding the pinning field distribution [137]. As the number of layers increases further, much like ($15 \leq n \leq 20$), the switching field keeps increasing at $n=20$ and the demagnetising field becomes larger which leads to more domains in zero field, and therefore it decrease the remanent magnetisation [138].

4.4 Kerr microscopy domain imaging

The magnetic domains for CoFeB and CoB were investigated at room temperature using Magneto-Optical Kerr effect (MOKE). In Chapter 5 we are going to present measurements of the DMI as a function of temperature. Kerr microscopy has been used in the polar mode in order to sense out-of-plane magnetisation. The fields were applied depending on the coercivity of the sample. The domain morphology is very different between CoFeB and CoB. Figure 4.4 shows the variation in CoFeB domain structure as n is increased. The domains in CoFeB $n \leq 2$ show a maze domain due to a higher perpendicular anisotropy. As the repeats are increased, $5 \leq n \leq 7$, the size of the domain becomes smaller which arises from a competition between surface and shape anisotropy. As the thickness increases the surface anisotropy decreases and the shape anisotropy enforces the domain to be small. While the number of layers increases, $n > 7$, we cannot see the domains for the CoFeB even increasing the magnification of the microscope to 50.00x. Consequently, we can say more repeats give smaller rougher domains and more nucleation of domain walls.

4.4 Kerr microscopy domain imaging

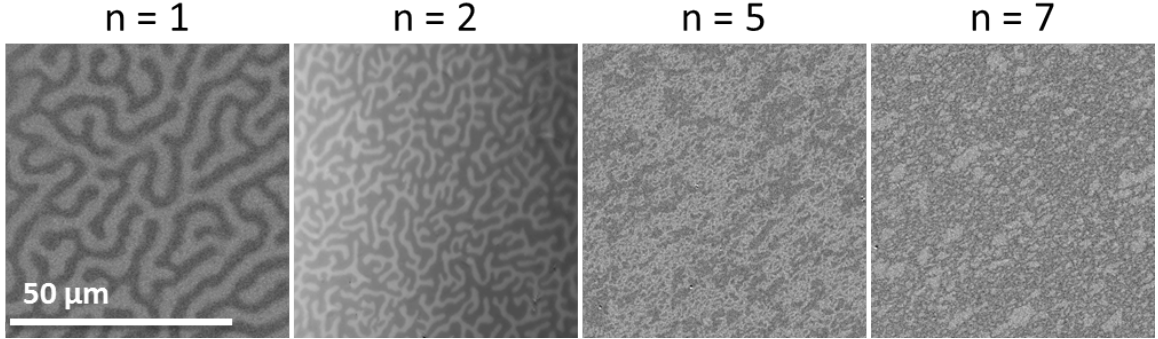


Figure 4.4: Kerr microscopy shows that the demagnetised domain patterns of CoFeB is a function of ‘n’. At the small repeat, $n \leq 2$, the domains show a maze domain and get smaller when the repeats, $5 \leq n \leq 7$, are increased. The bright and dark regions represent out of-plane magnetisation pointing up and down.

For CoB system, the magnetic domain also was imaged as a function of n as shown in Figure 4.5. The domains have been seen by using 20.00x lens but when they are almost too small we used 50.00x lens. At small number of repeats, $n \leq 2$, the domain image shows clear bubbles and very large domains and easy to move than other samples. As increasing the repeats, $5 \leq n \leq 10$, the domains become very small and maze due to the nucleation density is high and the domain walls are very rough. At (n = 5) and (n = 10) repeats we observed the domains almost without applying magnetic field because of lower remanence. Furthermore, if the repeats are increased, $12 \leq n \leq 20$, the domains become too small and hard to see due to lack of perpendicular anisotropy.

The main objective of using Kerr microscopy is to obtain the DMI by bubble expansion. However, most of samples showed maze domains. Demagnetising the sample, maze domain, at remanent state is a better way of making progress. Therefore, the domain width method of the maze domains allows calculating the domain period and from that we can obtain DMI[139].

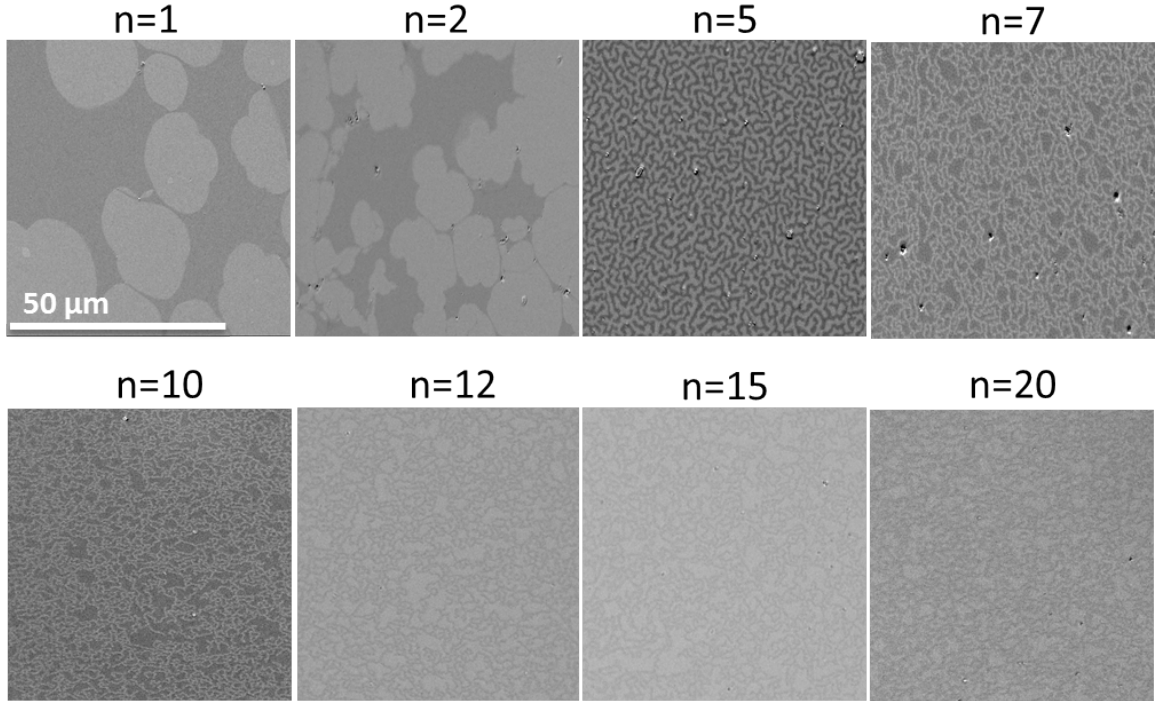


Figure 4.5: Kerr microscopy shows that the demagnetised domain pattern of CoB is a function of ‘n’. At the small repeat, $n \leq 2$, the domains show bubbles domain. At $5 \leq n \leq 10$ the domains become small and form as maze domain. Further increase, $12 \leq n \leq 20$, the domains become too small and hard to see. The bright and dark regions represent out-of-plane magnetisation pointing up and down.

4.5 XMCD domain imaging

Determination of the DMI has been shown to be possible by modelling such domain patterns [139][47]. The X-ray magnetic circular dichroism - photoemission electron microscope [XMCD-PEEM] has used at the Diamond Light Source to obtain a higher resolution magnetic image. Using XMCD-PEEM (higher resolution), we can image the remanent ferromagnetic domain state in the films and we can image domains from samples with larger repetition (n) than we can with the Kerr microscope.

4.6 Anisotropy field measurements

Two samples were imaged at remanent state as shown in Figure 4.6, which are Pt/CoB/Ir and deposited onto silicon oxide (SiOx) and barium titanate (BTO). Those samples were easy to demagnetise on the original hysteresis loop and the field which reversal started to happen is not very large. Also, the maze domains were existed and the DMI can be determined. This is a good method to determine the DMI without applying field and obtain the temperature dependence on DMI more easily (as it will present in Chapter 5) than using bubble expansion technique.

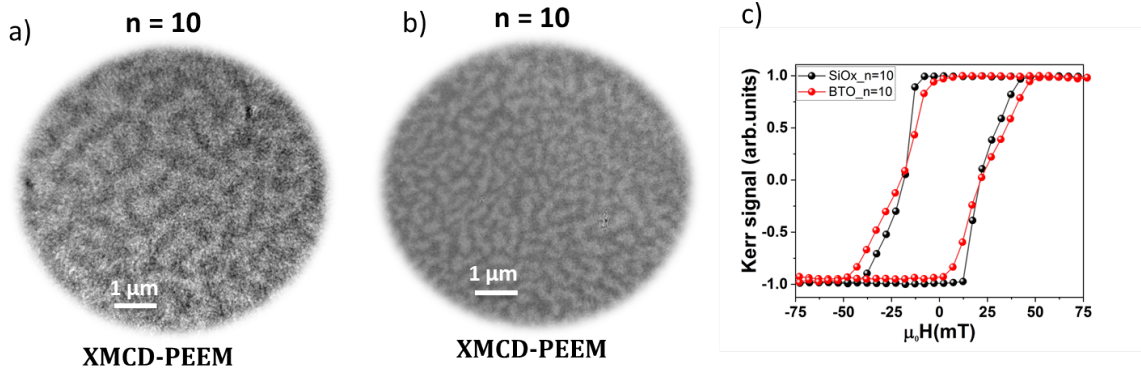


Figure 4.6: Maze domain pattern in a [Pt/CoB/Ir]_{n=10} superlattice imaged by XMCD-PEEM at room temperature, following ac demagnetisation. a) [Pt/CoB/Ir]_{n=10} on SiOx substrate. b) [Pt/CoB/Ir]_{n=10} on BTO substrate. The scale bar = 1 μm for both images. c) Polar MOKE hysteresis loops for [Pt/CoFeB/Ir]_{n=10} onto SiOx and BTO substrates.

4.6 Anisotropy field measurements

In order to measure the perpendicular magnetic anisotropy of the Pt/CoFeB/Ir and Pt/CoB/Ir multilayers, a magnetometric technique was employed using the extraordinary Hall effect (EHE). In this section the Hall voltage is measured as a function of angle (θ). The field will rotate the magnetisation and the change of the magnetisation is proportional to $\cos\phi$. By normalising the data and fitting a

4.6 Anisotropy field measurements

parabola, the anisotropy field $\mu_0 H_k$ can be determined from the fitting parameter as shown in the Equation 4.1:

$$H_k = \frac{2K_u}{M_s} = H \frac{1 - \sqrt{A_2}}{\sqrt{2A_2}} \quad (4.1)$$

where K_u is the uniaxial anisotropy (PMA), M_s is saturation magnetisation, H is the external field and A_2 is the quadratic term taken from the parabola. The magnetoresistance rig was used at room temperature to measure the dependence of the sweeping angle (ϕ_H) on the magnetisation angle (θ). The sweeping angle can also be referred to as the angle of the external field. The samples were wire-bonded on opposite edge of square sample. Two opposite wires connected to a Keithley 182 nanovoltmeter, and the remaining two wires connected to a current source supplied from Keithley 2400 sourcemeter to measure the Hall voltage. First, the sample was placed on a holder to be rotated in the fixed external field. There shall be a transversal electrical voltage is stimulated by the Hall effect when a constant current is applied across the sample. Moving on, the sample is rotated by 5° increments of the angle of the external field from the easy axis (ϕ_H) with the rotation axis parallel to the current flow, granting the ordinary Hall voltage to be deducted from the total. The evolving signal generated by the ordinary Hall effect during one sweep between -180° and $+180^\circ$ is proportional to the out-of-plane external field ($H \cos(\phi_H)$), given that the amplitude is also proportional to the magnitude of the external field.

At the beginning, we started to measure the $\mu_0 H_k$ by using the old sample stage and we could not fit the parabola accurately. That because the holder sample was not tied and the wiring in the stage had deteriorated with time. Also, the wire cable that is connected with holder sample (PCB) is twisted during the measurement and generated a tension. In Figure 4.7 below, we see the fitting of a parabola before the improvement.

The old design was a manual system and very difficult to repeat the measurements. Automatisations of the measurement was important to ensure consistency of the data obtained. Also, over time the system had degraded both mechanically and electrically. The cabling introduced a strain on the stage when we rotate the sample. Also, the sample does not rotate on axis which results in a changing or

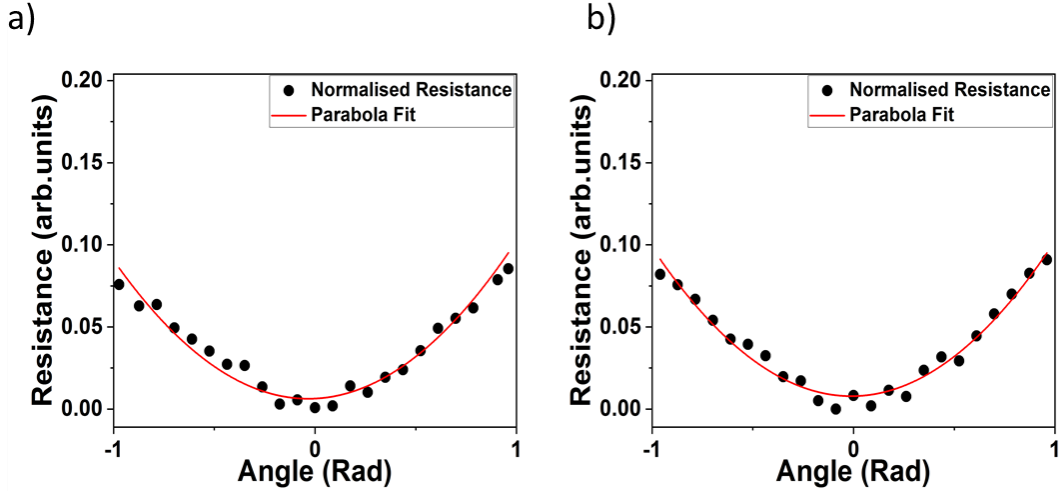


Figure 4.7: Normalised resistance against the sweeping angle in a constant external field of 500mT before improvement. A polynomial fit was applied to the data to extract the quadratic function. a) [Pt/CoFeB/Ir] with ($n=10$). b) [Pt/CoB/Ir] with ($n=10$).

non-uniform field. The high voltage lines have been separated from the signal lines to minimise effects in signal lines.

After fixed the existing old sample stage by fixing the wiring and mechanical aspects. The holder sample is tied, wire cable of PCB does not twist during rotating the sample and used a spirit level for the sample on the holder to be in the middle of two pole-piece magnets. Also, the system has been automated such that the measurement software is able to rotate the sample and collect whole measurements.

Furthermore, this allows to take multiple measurements of the samples quickly and consistently. The wiring was improved by using twisting pair within a screened sheath. This will remove the magnetic field generated by the source current. By using a step motor the sample does not rotate during the whole measurements due to the strain from the cable. As shown in Figure 4.8, there is a big improvement in quality of the data.

4.6 Anisotropy field measurements

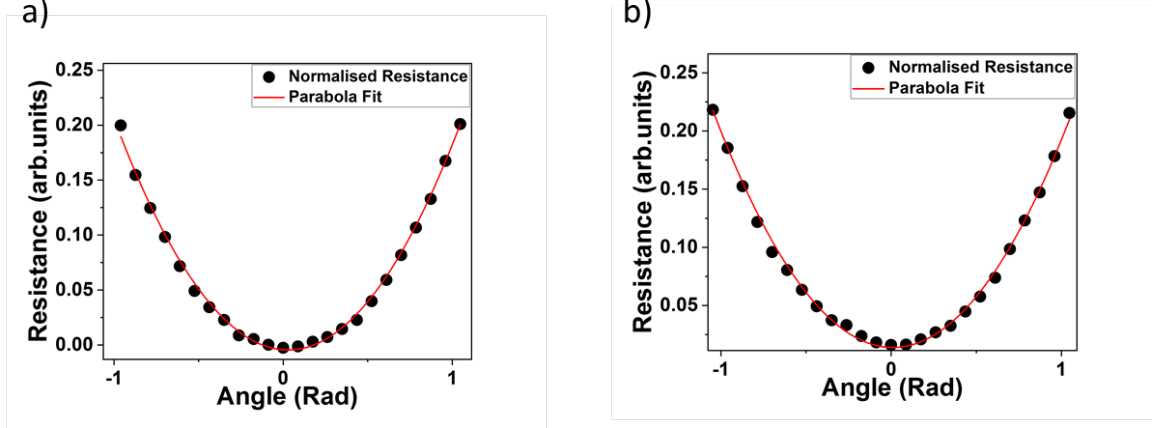


Figure 4.8: Normalised resistance against the sweeping angle in a constant external field of 500mT after improvement. A polynomial fit was applied to the data to extract the quadratic function. a) [Pt/CoFeB/Ir] with ($n=10$). b) [Pt/CoB/Ir] with ($n=10$).

More samples of CoFeB and CoB were measured to obtain a clear relationship between the anisotropy field and the number of layers as shown in Figure 4.9.

Regardless of CoFeB and CoB it has to be clear that the anisotropy field was found to decrease as the number of layers increased based on the observation of the samples where a fit was applied as shown in Figure 4.9.(c). As estimated, the largest anisotropy field calculated through studies was for when the sample had $n = 1$. Whereas the smallest anisotropy field calculated was for the sample with $n = 10$. The diminishing that takes place in the anisotropy field as the number of layers rises is a consequence of the surface roughness, which increases with each and every successive layer. The surface roughness origin may be due to a number of factors: a non-smooth Ta layer, nanocrystalline misorientation and accumulative defects, which leads to a decrease in the interface anisotropy [140]. With studies showing that multilayers with atomic-scale at interfaces show a large PMA and a high thermal stability, a smooth base layer became essentially required for high magnetocrystalline anisotropy.

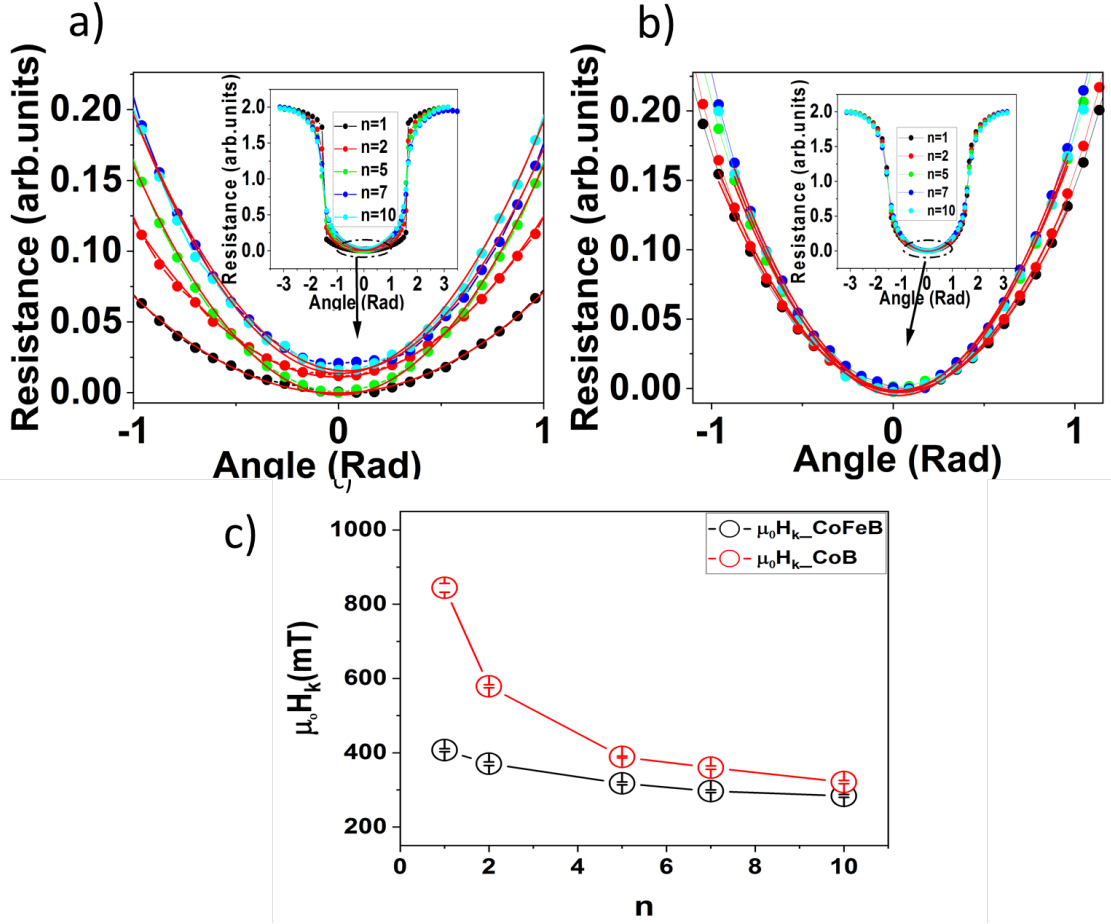


Figure 4.9: Normalised resistance against the sweeping angle in a constant external field of 500mT. a) A polynomial fit was applied to the data to extract the quadratic function for CoFeB with different repeat. b. A polynomial fit was applied to the data to extract the quadratic function for CoB with different repeat. c) Anisotropy field decreased as the number of repeat increased for both CoFeB and CoB and the solid line is a guide to the eye.

4.7 Magnetisation (M_s)

The magnetic moments of Pt/CoFeB/Ir and Pt/CoB/Ir films were measured in SQUID-VSM at room temperature to obtain the magnetisation (M_s). Saturation magnetisation is the saturated moment divided by the volume of ferromagnetic

material. An example of in plane hysteresis loop is shown in Figure 4.10.

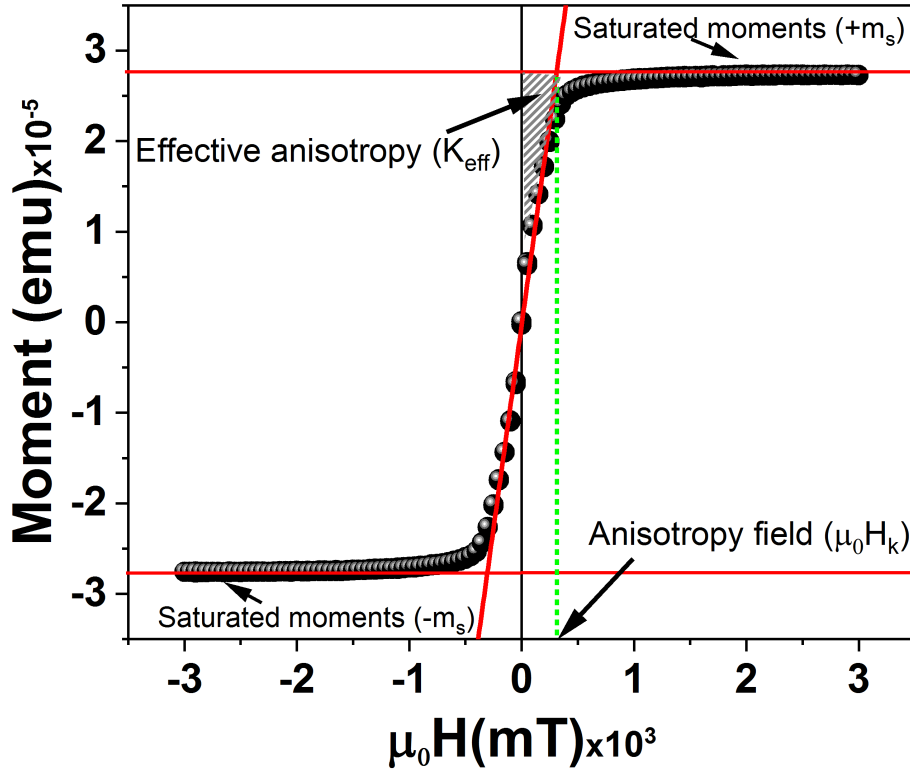


Figure 4.10: In-plane hysteresis loop of [Pt/CoFeB/Ir] $\times 2$ with out-of-plane anisotropy deposited on SiOx. Parameters that can be extracted from experimental data are shown. The red lines are linear fits to data.

Figure 4.11 shows the saturation magnetisation for all the CoFeB and CoB thin films as a function of repeat. It can be seen that the saturation magnetisation changed slightly with different repeats. For CoFeB the magnetisation varies from (0.91-1.13) MA/m, whereas CoB the magnetisation varies from (0.88-0.99) MA/m. The variation in saturation magnetisation as a function of repeat for the same composition of CoFeB and CoB is due to the amorphous nature of the films. The atoms have only short-range order, no long-range order and the nearest neighbour atoms change from thin film to others. In CoFeB and CoB films,

the magnetic moment of Co or Fe atoms depend on the saturation magnetisation and the nearest neighbours is an average of the moments, which can change for each thin film. This means the effect of the nearest neighbour atoms is the likely reason of variation in saturation magnetisation as a function of repeat. The same effect was seen for crystalline $\text{Fe}_{40}\text{Co}_{60}$, when the sample has an ordered bcc structure, the saturation magnetisation becomes higher, compared to a disordered fcc structure [141]. While the CoFeB and CoB films are amorphous and have no long-range order or set lattice constant, the nearest neighbours atoms to the Co or Fe can differ between thin films, which can vary the saturation magnetisation from sample to others.

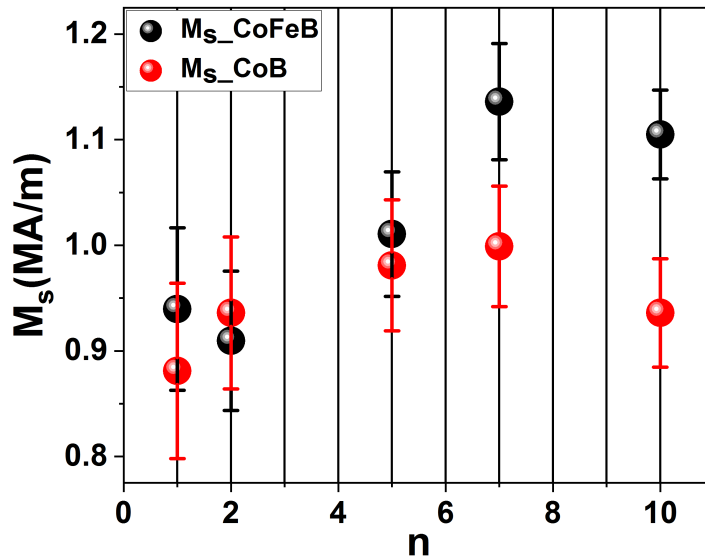


Figure 4.11: Saturation magnetisation (M_s) of Pt/CoFeB/Ir and Pt/CoB/Ir with different repeats. The saturation magnetisation slightly changed with different repeat due to the amorphous nature of the films, which means the atoms have no long-range order and the nearest neighbour atoms change from sample to others. For the $\text{Co}_{68}\text{Fe}_{22}\text{B}_{10}$ the estimate expected is a little high ~ 1.2 MA/m and for $\text{Co}_{68}\text{B}_{32}$ is in the same range ~ 0.95 MA/m

4.8 Effective anisotropy (K_{eff})

In addition, from in plane hysteresis loop we can calculate the anisotropy field H_k and effective anisotropy K_{eff} . There are several methods to extract the anisotropy field of thin-film magnetic samples as shown in Figure 4.12. The middle part of the graph is fitted with straight-line and the field on this line that contains the saturation moment will be the anisotropy field, H_k , as shown in Figure 4.10. Second method is extraordinary Hall effect by fitting a parabola as described in section (4.6). A third method is to integrate the area of a hysteresis loop and divide it by the volume of the sample, which was used to calculate effective anisotropy. It is all about using different methods, which make use of different experimental approaches and more importantly, using different approximations to a real physical problem, that is measuring the magnetic anisotropy energy or constant. The method employing the area subtractions for H(M) curves determined along hard and easy crystalline axis is much more accurate than the two others methods, because these assume a linear response, ie M-H is linear, but the real material behaves in a more complicated and complex, non-linear way. Additionally, linear response method assumes the work to magnetise the material along the easy axis as zero. Since the materials behave in a more complicated and complex non-linear way, the integrating of area is more accurate and has a less error. Whereas the approximating of straight-line is a less accurate and has a large error when the materials behave in non-linear way.

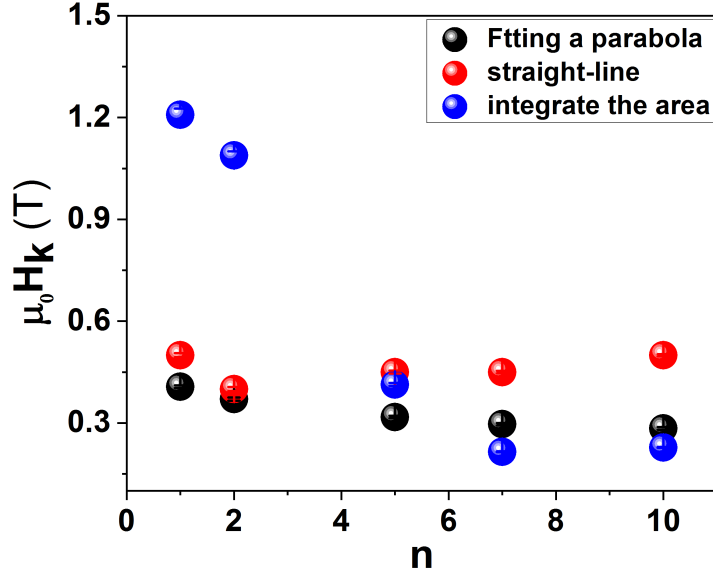


Figure 4.12: The anisotropy field (H_k) of CoFeB with different repeats. Using three different methods (fitting a parabola, straight line and integrate the area). For fitting a parabola and integrate the area methods, it's shown that the anisotropy field decreases when the number of repeats increases. However, for straight line method the real material behaves in a more complicated and complex, non-linear way and the approximating of straight-line is a less accurate. The integrate the area method is used to find the K_{eff} as linear response method assumes the work to magnetise the material along the easy axis as zero. The second method, fitting a parabola, is used to investigate the effect of strain with stressor using MR-rig, since we can not use the stressor in SQUID. Also, the MR-rig and MOKE have not enough field to saturate the sample.

The effective anisotropy of CoFeB and CoB was found to decrease when the number of repeats increased as shown in Figure 4.13. As the number of repeats increases, the random distribution ad-atoms will accumulate and the surface roughness will increase, leading to a relaxation state and the destruction of the multilayers structure. The surface roughness induced from the random nature of such fluctuations may be expected to lower the strength of PMA [136] [142].

4.8 Effective anisotropy (K_{eff})

It was shown that the magnetic properties of $\text{Co}_{90}\text{Fe}_{10}/\text{Pt}$ multilayers strongly related to its surface and interface morphology [136].

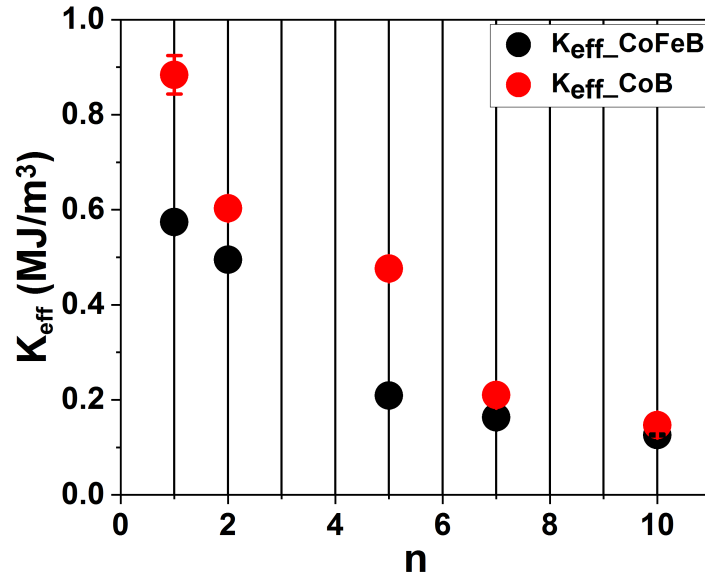


Figure 4.13: The effective anisotropy (K_{eff}) of CoFeB and CoB with different repeats. It's shown that the effective anisotropy decreases when the number of repeats increases due to the surface roughness such as nanocrystalline misorientation, a non-smooth Ta layer and defects.

4.9 Exchange stiffness (A)

It is well known that the exchange stiffness in magnetic materials decreases as the temperature increases [143]. The temperature dependence of this parameter is often expressed as a power law in the reduced magnetisation (m), e.g. calculations for Co indicate that the exchange stiffness, $A(m) \sim m^{1.8}$ is a very good approximation [143]. The temperature dependence of saturation magnetisation for CoFeB and CoB was measured in the range of 5-250 K to calculate the exchange stiffness. The Bloch law for thin film shows the relation of saturation magnetisation with temperature if it is far from Curie temperature as shown in Equation 4.2 below:

$$\frac{M_s(T)}{M_s(0)} = 1 + \frac{a^3}{NS} \frac{1}{4\pi} \frac{1}{n_z a_z} \frac{k_B T}{2D} \sum_{n=0}^{n_z} \ln \left(1 - e^{-\left(D\left(\frac{n\pi}{n_z a_z}\right)^2 + \hbar\omega_0\right)/k_B T} \right) \quad (4.2)$$

where $M_s(0)$ is the zero temperature magnetisation, N is the number of atomic layers in the thickness (t), S is the spin quantum number of each atom, k_B is the Boltzmann constant = $(1.38 \times 10^{-23} \text{ J/deg})$, T is the temperature, D is the spinwave stiffness: $D = 2\mathcal{J}Sa^2$, $\hbar\omega_0$ is energy term added into the exponential, n_z is the number of atomic layers in the z-direction and a_z is the distance between atomic layers in the z-direction. This differs for different lattice types (simple cubic, bcc, fcc) and orientations but all are based on a cubic lattice parameter $a = 0.355 \text{ nm}$ [144]. As the FM layers are amorphous the choice of a_z is somewhat arbitrary; we use values that would correspond to bcc and fcc lattices in the [100] and [111] orientations. Once the temperature dependence of saturation magnetisation measured for CoFeB and CoB, we use Equation 4.2 to fit the data and evaluate D . Then, the exchange stiffness (A) from Equation 4.3 can be calculated:

$$A = \frac{N\mathcal{J}S^2}{a} \quad (4.3)$$

From the fitting with the Bloch law for thin film in Figure 4.14.(a) we obtained the exchange stiffness $A(T = 0)$, then expressed the value as a power law in the reduced magnetisation $A(T) = A(T = 0) \times m^{1.8}$.

4.9 Exchange stiffness (A)

Following the mentioned procedure, the exchange stiffness values at room temperature (300K) was calculated as shown in Figure 4.14.(b). As a result, the exchange stiffness for CoFeB $n= 1$ and 2 was found $A= (2.6 \pm 2$ and $2.7 \pm 2)$ pJ/m, whereas, CoB $n= 5, 7,$ and 10 was $A= (4.8 \pm 2, 5.2 \pm 2$ and $3.9 \pm 2)$ pJ/m, respectively. There is a considerable uncertainty in the number of atomic layers represented by the thickness of the film because the film is likely rough at the interfaces. We therefore estimate the uncertainty in A by calculating A for $n_z \pm 1$ from the nominal value $n_z = t/a_z$ and taking the largest difference in A as the uncertainty. Our estimated error is therefore large (up to 30 %) but we believe it is a realistic estimate of how well A can currently be inferred from thermodynamic measurements in amorphous films. All the values of A here lie within the range of the uncertainty estimated above. Generally the more layers, the smaller this error because the summation in the Bloch's law is converging to the bulk value. For very thin films (like $n_z=4$) the difference between ± 1 layer is very large. Also, we looped over different lattice types such as BCC(100), BCC(111), FCC(100) and FCC(111). We have not derived the equation for BCC or FCC lattices. The effective approach we have is that the Wigner-Seitz volume changes and the distance between the layers (hence the number of layers in the film) also changes. The good thing, for using different lattice types, is that this does not change A by very much, as long as we adjust the number of layers correctly.

The values of A , as the repeat varied, seemed to be the same for both system CoFeB and CoB. However, the exchange stiffness for CoFeB is smaller than CoB. It was proved by Mohammadi et al. that when the thickness of a magnetic material decreases, the η will increase and D decreases, which leads to an increase in the A [59]. In addition, these values are smaller than a typical value of 6.5 pJ/m found in a Pt/CoFeB structure [145]. The difference could be due to the intermixing of CoFeB/CoB and Pt at the interface, which has been seen to reduce M_s and A in Co/Pt multilayers [146], [147].

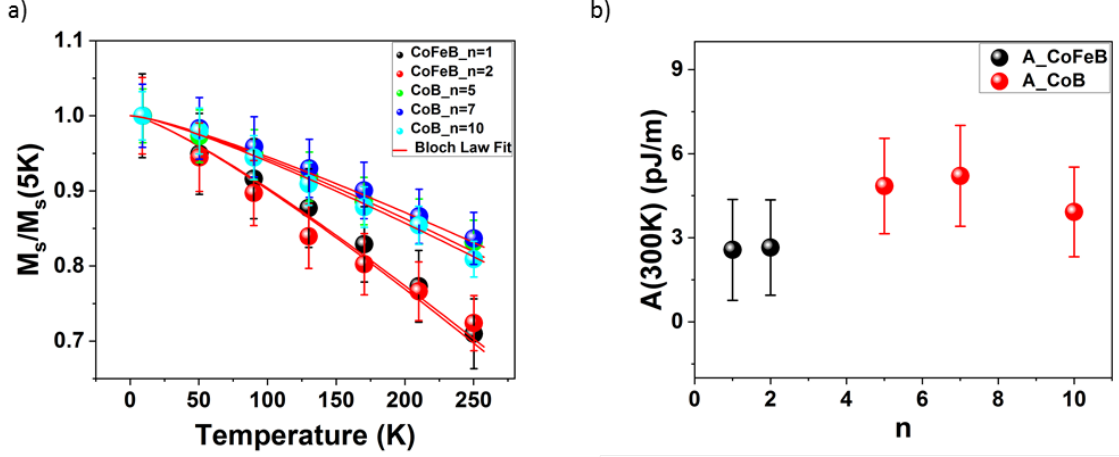


Figure 4.14: Temperature dependence of saturation magnetisation for [Pt/CoFeB/Ir] with $n=1$ and 2 , and [Pt/CoB/Ir] with $n=5, 7$ and 10 . The red line is Bloch law fit for thin film using Equation 4.2. b) The exchange stiffness at room temperature for CoFeB $n=1$ and 2 (black point), and CoB with $n=5, 7$ and 10 (red points).

4.10 Domain Period (d)

This technique is based on static domain spacing, which is determined by minimisation of the demagnetising energy and the domain wall (DW) energy [139][47]. The domain spacing in the equilibrium state can be used to determine the domain wall energy, which leads to estimate the DMI with very few assumptions. To obtain the domain wall energy, we need to measure the domain period. Wide-field Kerr microscopy was used to image the magnetic domains in the demagnetised state. After demagnetising the sample, the image was taken in zero field. Then the image editing software, image J, was used as explained in more details in Chapter (3). Raw domain image was inserted in the image J software and cut 300x300 pixel squares to get a representative spread of data. A black and white threshold image was applied to maximise the efficiency of the FFT as shown in Figure 4.15.

Once the image was successfully thresholded and a FFT applied, the do-

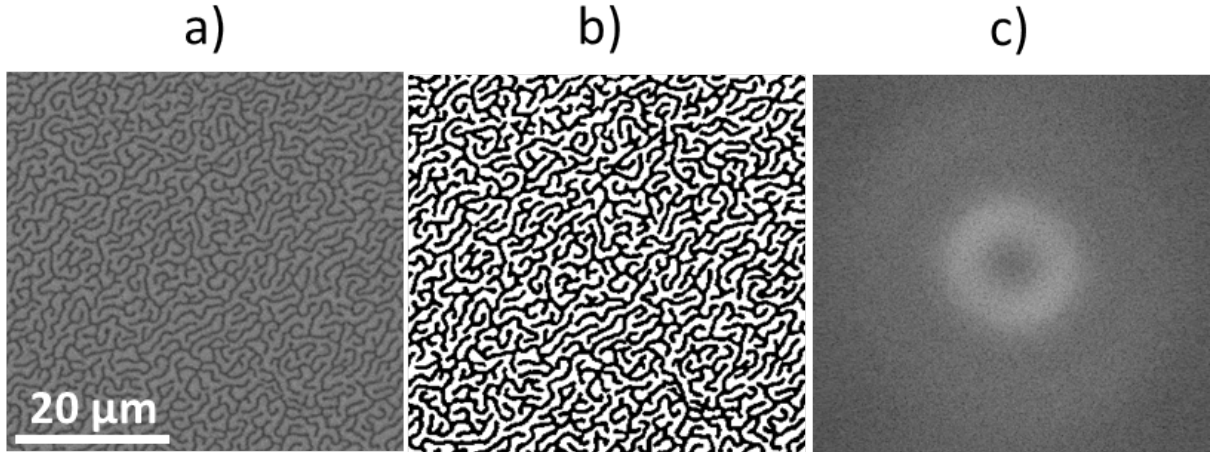


Figure 4.15: a) Magnetic domain of $[\text{Pt}/\text{CoFeB}/\text{Ir}]_{\times 2}$ imaged by Kerr microscopy and edited using, image J, to produce the FFT. a) A raw image inserted and cut 300x300 pixels. b) Threshold image to increase the efficiency of the FFT. c) A fast-Fourier transform of the domain image.

main image can be converted to circular intensity peak (Figure 4.16).(a)). A fast-Fourier transform of the image yield a radial average of the data in reciprocal space, which is then fitted with a Gaussian distribution and after transforming back into real space the peak of the distribution as shown in Figure 4.16. (b) gives the average of the domain period.

Following the mentioned procedure, the magnetic domain of CoFeB ($n=1$ and 2) and CoB ($n=5,7$ and 10) were imaged and edited as shown in Figure 4.17. These domains show a “maze” pattern, depending on the number of repeats at zero field. The images of domain pattern show that the magnetic domain is smaller in CoB ($n=5, 7$ and 10) than CoFeB ($n=1$ and 2). As the number of repeats increases in both systems, the switching field keeps increasing which results in a large dipolar stray field coupling [138]. The large stray field gives more energy to be spent on the creation of the domains and that results a small size of domains.

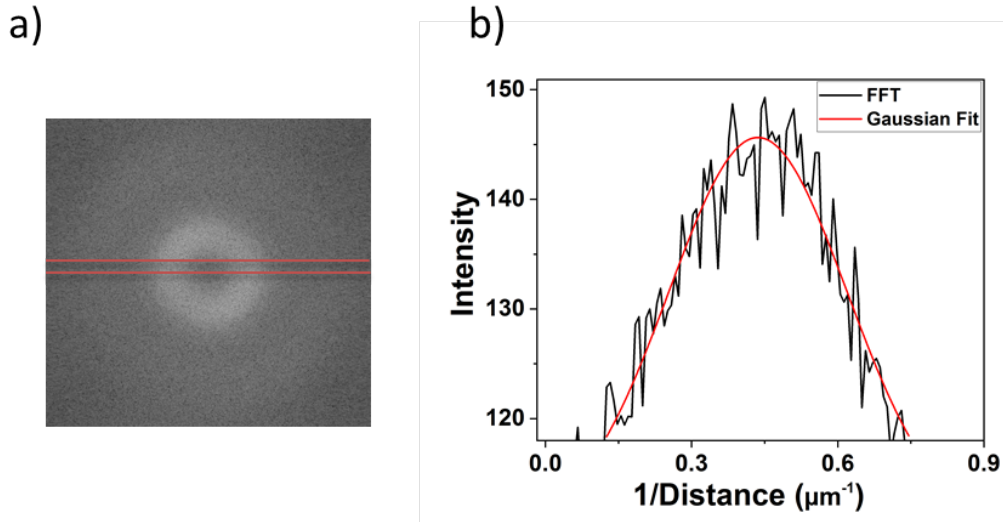


Figure 4.16: An area is spanned across the transformed image to plot two intensity peaks for all sides of the inner ring. b) Gaussian fit to the radial average peak intensity of the Fourier transform to gives the average of the domain period.

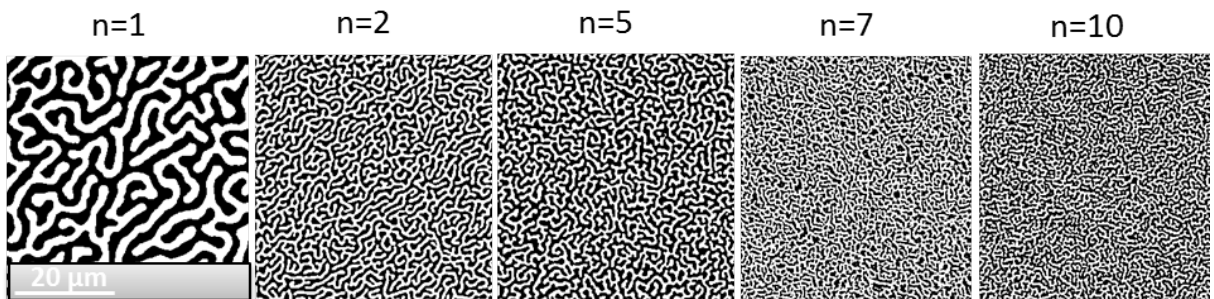


Figure 4.17: Typical demagnetised domain patterns at room temperature for CoFeB ($n=1$ and 2) and CoB ($n=5,7$ and 10).

By taking a fast Fourier transform and fitting the peak with a Gaussian function as shown in Figure 4.16, the equilibrium labyrinth domain period can be extracted for all the samples. Figure 4.18 shows a general trend is for domain period of CoFeB and CoB to decrease with increasing the number of repeats due to a large demagnetising field.

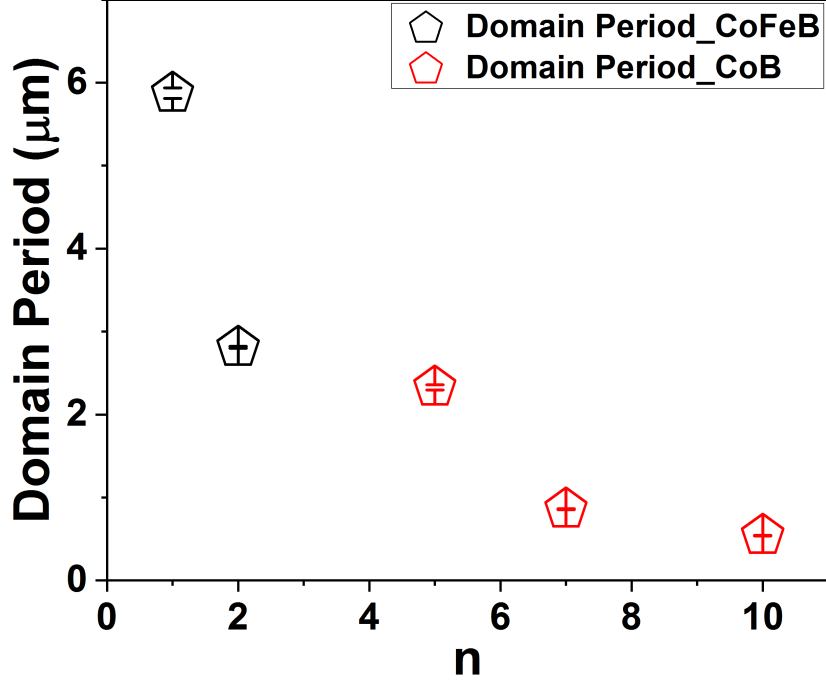


Figure 4.18: Magnetic domain period for the multilayer [Pt/CoFeB/Ir] ($n=1$ and 2) and [Pt/CoB/Ir] ($n=5,7$ and 10) grown on SiO_x substrate at room temperature. The domain period for both system decreases when the number of repeats increases.

Since the domain period, saturation magnetisation and thickness were determined, enabling a calculation of domain wall energy density following the approach of Lemesh et al [47].

$$\sigma_{Dw} = \frac{\mu_0 M_s^2 f d^2}{Nt} \sum_{\text{odd } k=1}^{\infty} \frac{1}{(\pi k)^3} \left(1 - \left(1 + \frac{2k\pi Nt}{d} \right) \left(e^{-\frac{2k\pi Nt}{d}} \right) \right) \quad (4.4)$$

To determine DW energy, the saturation magnetisation and magnetic domain period were calculated by individual measurements for each sample. The DW energy was found for CoFeB ($n=1$ and 2) and CoB ($n=5,7$ and 10) to be between

(1.3-5.2) mJ/m² as shown in Figure 4.19, using Equation 4.4. The DW energy started increasing from CoFeB $n=2$ to CoB $n=5$ and slightly decreasing for CoB $n=7$ and 10. This could be due to the large number of repeats, which leads to decrease the magnetic anisotropy energy. It has been shown that for Ni/Co with number of repeats from 3 to 70, the DW energy started to increase from small n until reaching $n=20$ and then decreased for large number of repeats [148].

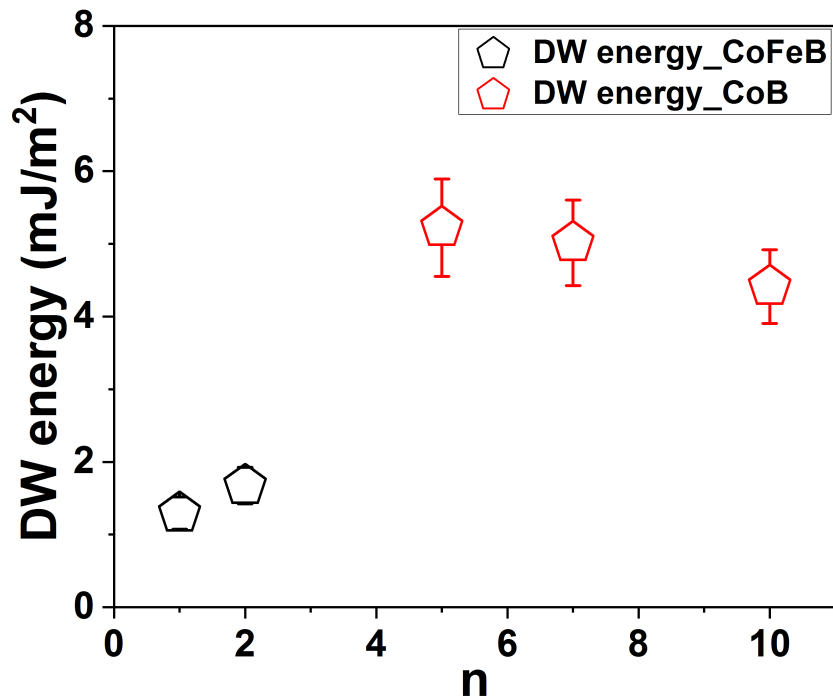


Figure 4.19: Domain wall energy for the multilayer [Pt/CoFeB/Ir] ($n=1$ and 2) and [Pt/CoB/Ir] ($n= 5,7$ and 10). The domain wall energy of CoFeB and CoB has increased with number repeats and after CoB $n=5$ slightly decreased at CoB $n=10$.

4.11 Interfacial Dzyaloshinskii-Moriya interaction (DMI)

The Dzyaloshinskii-Moriya interaction (DMI) is essential for chiral domain walls (DWs) and for the stabilisation of magnetic skyrmions. The DMI measurements in magnetic thin films (single-layered and multilayered) are important for evaluating their potential as material for skyrmionic memory and sensor applications. In addition, strong DMI can effectively minimise the domain wall energy cost by stabilising Néel walls. Determination of the DMI has been shown to be possible by modelling such domain patterns [139][47]. Here we investigate the effects of increasing the number of repeats of Pt/CoFeB/Ir and Pt/CoB/Ir to evaluate the DMI at room temperature. The DMI were quantified by analysing the static domain spacing of a maze pattern to obtain the domain wall energy. In combination with SQUID measurements of saturation magnetisation and effective anisotropy, this gives to estimate the exchange stiffness in these multilayers. For each sample, we take individual measurements of the exchange stiffness A , K_{eff} and δ_{DW} and calculate the DMI constant D . The DMI is calculated from an analytical expression for the domain wall energy density [51]:

$$|D| = \frac{4\sqrt{AK_{eff}} - \sigma_{DW}}{\pi} \quad (4.5)$$

where A is the exchange stiffness, K_{eff} is the effective anisotropy constant and $|D|$ is the DMI constant. Figure 4.20 exhibits the resulting DMI of CoB is less than what we can get with CoFeB, and the number of repeats does not necessarily affect the DMI as it was reported in Co/Ir [149]. The DMI of the CoFeB (n=1 and 2) is found to be in the range of $(1.1 \pm 0.5$ and $0.9 \pm 0.4)$ mJ/m², whereas, CoB n= 5, 7, and 10 is found $D = (0.3 \pm 0.4, 0.3 \pm 0.3$ and $0.4 \pm 0.2)$ mJ/m², respectively. The large error in the DMI comes from the exchange stiffness as it was explained in section 4.9, while K_{eff} error is (5-7) % and DW energy (8-12) %.

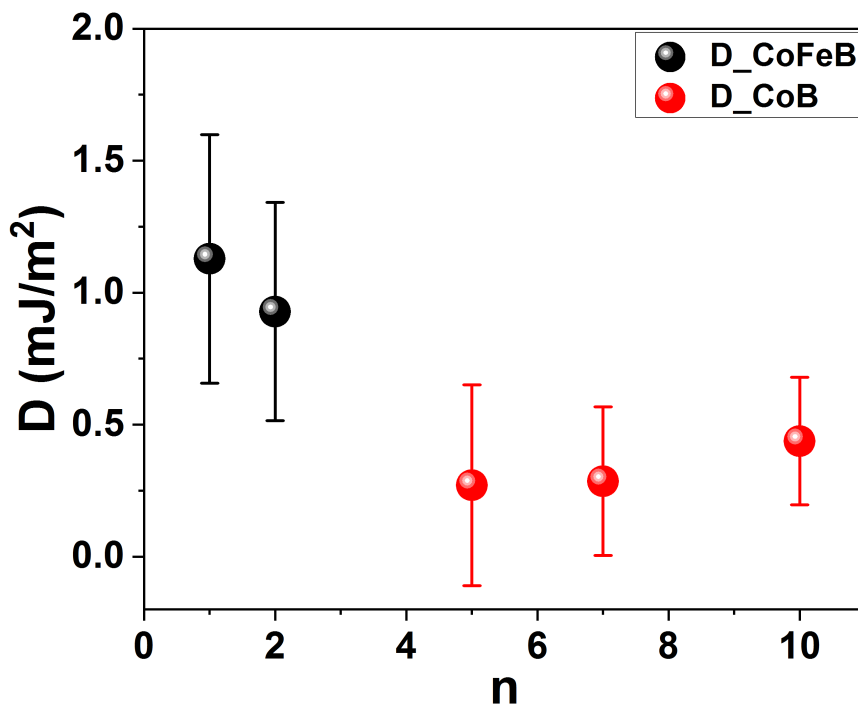


Figure 4.20: DMI constant D for the multilayer [Pt/CoFeB/Ir] ($n=1$ and 2) and [Pt/CoB/Ir] ($n=5,7$ and 10). The resulting DMI of CoB is less than what we can get with CoFeB and the number of stacking does not influence the DMI.

A threshold value D_{thr} , the minimum DMI required to show Néel walls for these thin films, was found to be < 0.1 mJ/m² as in Ref.[139], which is smaller than the D values obtained and confirms that our thin films exhibit Néel domain walls. The DMI values of Pt/CoFeB/Ir and Pt/CoB/Ir are almost similar to previous reports [51] [150][151][152]. However, the difference in the DMI between these systems could be associated with the higher proportion of magnetic material in CoFeB (the at % of Co is 68 in both cases, but in the CoFeB sample, there is an additional 22/10 at% of Fe/B compared with 32 at% B in the CoB sample). In addition, previous works showed Fe/Ir contributed to DMI and that could be another reason for large DMI for CoFeB [153][154][155].

4.12 Summary

The magnetic properties of CoFeB and CoB multilayers with different repeat of Pt/CoFeB/Ir or Pt/CoB/Ir have been characterised by using polar laser MOKE measurements and the magneto-optical Kerr effect. For both systems, a small number of multilayers, the hysteresis loops are narrow and square shaped and the coercive field is small. As the number of layers increases further the switching field keeps increasing, which leads to decrease of remanent magnetisation. The magnetic domains for CoFeB and CoB were imaged at room temperature using Magneto-Optical Kerr effect. The magnetic domains for CoFeB show a maze domain and get smaller when the repeats, $5 \leq n \leq 7$, are increased. While the magnetic domains for CoB, at the small repeat $n = 2$, show bubbles domain. At $5 \leq n \leq 10$ the domains become small and form as maze domain. Further increase, $12 \leq n \leq 20$, the domains become too small and hard to see.

The magnetic anisotropy is measured using a method based on the extraordinary Hall effect (EHE). The anisotropy field for CoFeB and CoB was found to decrease as the number of layers increase due to a rising in surface roughness at the interface. The saturation magnetisation for CoFeB (0.91-1.13) MA/m and CoB (0.88-0.99) MA/m was calculated with different repeats. The variation in saturation magnetisation as a function of repeat is due to the amorphous nature of the films and the nearest neighbour atoms change from thin film to others.

The effective anisotropy of CoFeB and CoB was found to decrease when the number of repeats increased. As the number of repeats increases, the random distribution ad-atoms will accumulate and the surface roughness will increase, leading to a relaxation state and the destruction of the multilayers structure.

The temperature dependence of saturation magnetisation for CoFeB and CoB was measured in the range of 5-250 K to calculate the exchange stiffness by fitting the thin film Bloch law.

A technique is based on static domain spacing in the equilibrium state used to determine the domain wall energy, which leads to estimate the DMI with very few assumptions. The resulting DMI of CoB is less than CoFeB, and the number of repeats does not affect the DMI.

CHAPTER 5

Temperature dependence of
Dzyaloshinskii-Moriya interaction in
magnetic multilayers (in SiO_x substrate)

5.1 Introduction

Magnetic multilayers with perpendicular anisotropy and an interfacial Dzyaloshinskii-Moriya interaction contain chiral domain walls and skyrmions that are promising for applications. Many proposed devices use electric current to drive domain walls or skyrmions along narrow magnetic strips. The induced Joule heating will raise the temperature of the devices. Moreover, it is expected for electronic devices to operate over a range of temperatures around room temperature. It is therefore important to understand the temperature dependence of the different energy contributions. The changes in anisotropy, exchange stiffness and demagnetising fields with temperature are reasonably well understood but the DMI less so. It is therefore important to measure the temperature dependence of DMI in a variety of candidate materials to improve our understanding. There is also fundamental interest, because the temperature dependence can lead to a better understanding of the microscopic origin of the DMI in magnetic multilayers.

Here we measure the temperature dependence of the Dzyaloshinskii-Moriya interaction (DMI) in Pt/CoFeB/Ir and Pt/CoB/Ir multilayers by means of static domain imaging. First, the temperature dependences of saturation magnetisation (M_s), exchange stiffness (A) and intrinsic perpendicular anisotropy (K_u) are determined independently, and scaling laws for K_u and D with the magnetisation are established. We then image the demagnetised domain pattern in each multilayer by wide-field Kerr microscopy in the temperature range 9-290 K, and determine the characteristic domain period at each temperature. We calculate the DMI constant D from an analytical expression for the domain wall energy density that treats the multilayer as a uniform medium. We find that the scaling of K_u and D are similar to that of A predicted theoretically (~ 1.8).

5.2 Samples

The multilayers that we studied consist of (i) [Pt(2.3nm)/Co₆₈Fe₂₂B₁₀(0.51nm)/Ir(0.5nm)]_n (CoFeB multilayers) and (ii) [Pt(2.3nm)/Co₆₈B₁₀(0.66nm)/Ir(0.5nm)]_n (CoB multilayers) deposited by dc magnetron sputtering on a 3 nm Ta seed layer

on a thermally oxidised Si substrate. A 2.3 nm capping layer of Pt was deposited on top to prevent oxidation. The ferromagnet (FM) is amorphous CoFeB or CoB, originally chosen to try and avoid the problems of skyrmion pinning at grain boundaries. Pt and Ir are chosen because they are expected to give rise to DMI of opposite signs at the top and bottom interface and thus a large net DMI, although this is disputed [156]. The number of repeats n was varied from 1 to 20 (as seen in chapter 4) and then the samples were subjected to an ac demagnetising procedure, yielding a maze domain structure at zero field. Three samples were then selected for further study according to their suitability for DMI measurement: those with a large number of domains in the typical field of view in a wide-field Kerr microscope (approximately $200\ \mu\text{m} \times 200\ \mu\text{m}$ square), to provide a reasonable statistical estimate of the domain period, but with domains that were still well resolved, no smaller than $0.8\text{-}3\ \mu\text{m}$. The samples thereby selected were CoFeB ($n = 2$) and CoB ($n = 5$ and 7).

5.3 Magnetic characterisation

The samples exhibit a perpendicular magnetic anisotropy as deduced from Figure 5.1.(a) and this can be measured using a magneto-optical Kerr effect magnetometer with a polar configuration that makes it sensitive to out-of-plane. In order to obtain the temperature-dependent value of the DMI, we first begin by extracting the M_s , A , K_{eff} , and K_u , as shown in Figure 5.1.(b, c, and d). The saturation magnetisation was measured from hard axis in-plane hysteresis loops in the temperature range 9- 290 K, and the exchange stiffness at low temperature was found by fitting a modified version of the Bloch $T^{3/2}$ law for thin films to the normalised SQUID-VSM moment versus temperature data. The temperature dependence of A was then extrapolated from the low temperature value by assuming a power law scaling of $A(m) \sim m^{1.8}$ [143]. The effective perpendicular anisotropy K_{eff} was measured from integrating the area of in-plane SQUID-VSM hysteresis loops and dividing it by the volume of the sample, from which the intrinsic perpendicular anisotropy K_u was calculated by accounting for the shape anisotropy term $\frac{1}{2}\mu_0 M_s^2$.

5.3 Magnetic characterisation

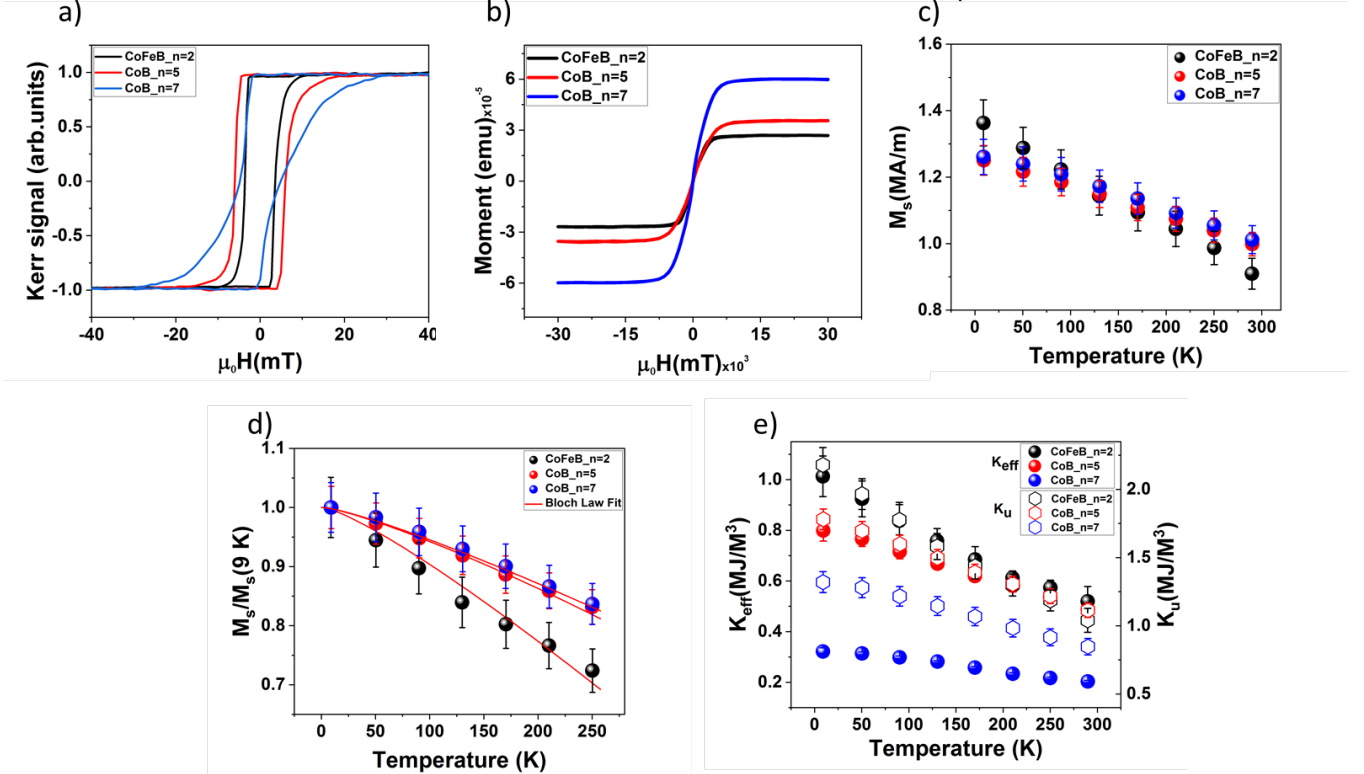


Figure 5.1: a) Hysteresis loops measured at room temperature by magneto optic Kerr effect with field applied out of plane. b) Hysteresis loops measured at room temperature by SQUID with field applied in-plane. c) The saturation magnetisation was measured from SQUID-VSM hysteresis loops in in-plane (hard-axis) configuration in the temperature range 9-290 K. d) Temperature dependence of saturation magnetisation normalised to the low temperature value and the solid lines are fits to the data using Equation 4.2 in (Chapter 4). e) The effective anisotropy (K_{eff}) and intrinsic perpendicular anisotropy (K_u) in the temperature range 9-290 K.

The temperature dependence of Dzyaloshinskii-Moriya interaction in Pt/CoFeB/Ir (n=2) and Pt/CoB/Ir (n=5 and 7) multilayers has been investigated. Figure 5.1.(a) shows hysteresis loops measured at room temperature (290 K). The main contributions to the perpendicular anisotropy and DMI come from the Pt/Co(Fe)B interface, and Co(Fe)B/Ir interface primarily plays a part in break-

ing the symmetry of the system [157]. Figure 5.1.(c) shows $M_s(T)/M_s(9K)$ for CoFeB ($n = 2$) and CoB ($n = 5$ and 7) thin films. Fitting the data with Equation 4.2 in (Chapter 4) yields the low temperature value of the exchange stiffness A for each sample, given in Table 5.3. We then extrapolate the temperature dependence of A using the power law scaling $A(T)/A(9K) = (M_s(T)/M_s(9K))^{1.8}$ from theory [143], as shown in Figure 5.2.

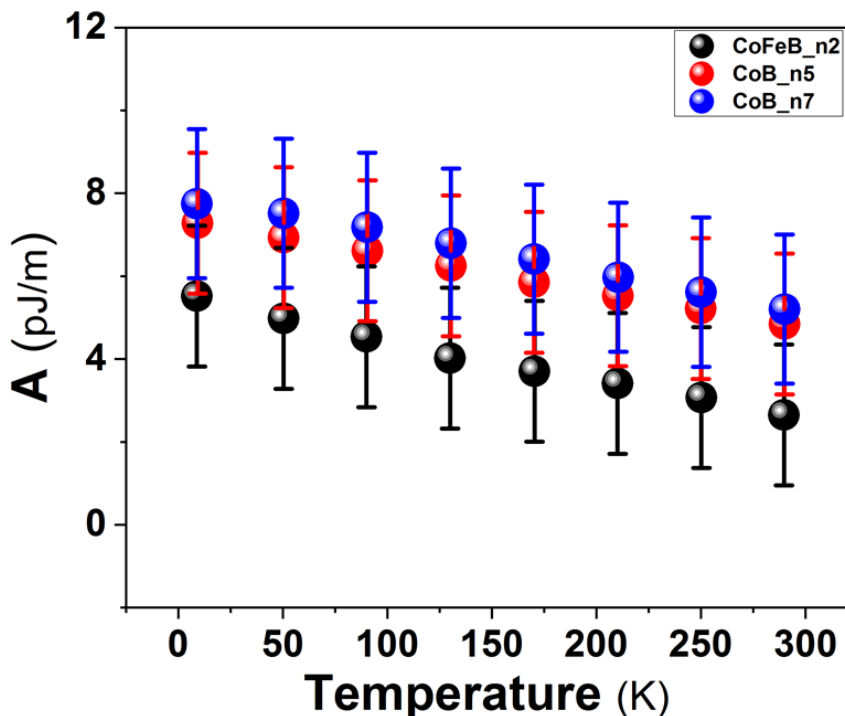


Figure 5.2: The Exchange stiffness for CoFeB $n=2$ and CoB $n= 5$ and 7 , using Bloch’s law for thin films in the temperature range 9- 290 K. Exchange stiffness decreases with increasing temperature due to renormalisation of the magnon spectrum by the thermal magnons.

The value of exchange stiffness in Bloch’s law is the zero temperature value. Exchange stiffness decreases with increasing temperature due to renormalisation of the magnon spectrum by the thermal magnons [158]. Theory and experiment

5.3 Magnetic characterisation

find an approximately power law scaling of the exchange stiffness with the temperature dependent magnetisation where the exponent depends on the lattice geometry [159].

The low temperature values of K_{eff} and the intrinsic perpendicular anisotropy K_u are reported in Table 5.3. The uncertainty in the anisotropy is mainly due to the error in measuring the volume of the sample, which is divided into the hysteresis loop area to find K_{eff} . In principle $K_u(T)$ contains both bulk magnetocrystalline anisotropies and interface anisotropies. However for amorphous transition metal films we expect the bulk anisotropy to be negligible. The main source of anisotropy is a two-ion anisotropy at the interfaces, for example Co-Pt-Co where the spin-orbit coupling of the Pt leads to an anisotropic exchange favouring an out of plane orientation for the magnetisation. The scaling of two-ion anisotropies according to Callen-Callen theory [4] is $K_u \sim m^2$.

Since the M_s , A , and K_{eff} were determined, we measured the magnetic domain period in the temperature range 9-290 K from images of the demagnetised domain pattern obtained by wide-field Kerr microscopy. We first saturate the samples in sufficient field (30-50 mT) and then demagnetise them by applying a sinusoidally varying out-of plane field at 0.5 Hz decaying over 120 seconds from a maximum amplitude of 30 mT down to zero. We then mounted each sample in turn in an optical cryostat and an image of the domain pattern was captured at several set temperatures across the range. Using a similar method to Agrawal et al.[139] we extracted the domain period from these images as shown in Figure 5.3.

Table 5.3. Extracted low temperature values of magnetic parameters for the three measured thin films.

Sample	$M_s(9\text{ K})\text{MA/m}$	$A(9\text{ K})\text{pJ/m}$	$K_{eff}(9\text{ K})\text{MA/m}^3$	$K_u(9\text{ K})\text{MA/m}^3$	$D(9\text{ K})\text{mJ/m}^2$
CoFeB (n=2)	1.36 ± 0.07	5 ± 2	1.01 ± 0.08	2.2 ± 0.1	1.8 ± 0.5
CoB (n = 5)	1.25 ± 0.04	7 ± 2	0.80 ± 0.04	1.78 ± 0.08	0.47 ± 0.40
CoB (n = 7)	1.26 ± 0.05	7 ± 2	0.32 ± 0.01	1.32 ± 0.08	0.52 ± 0.31

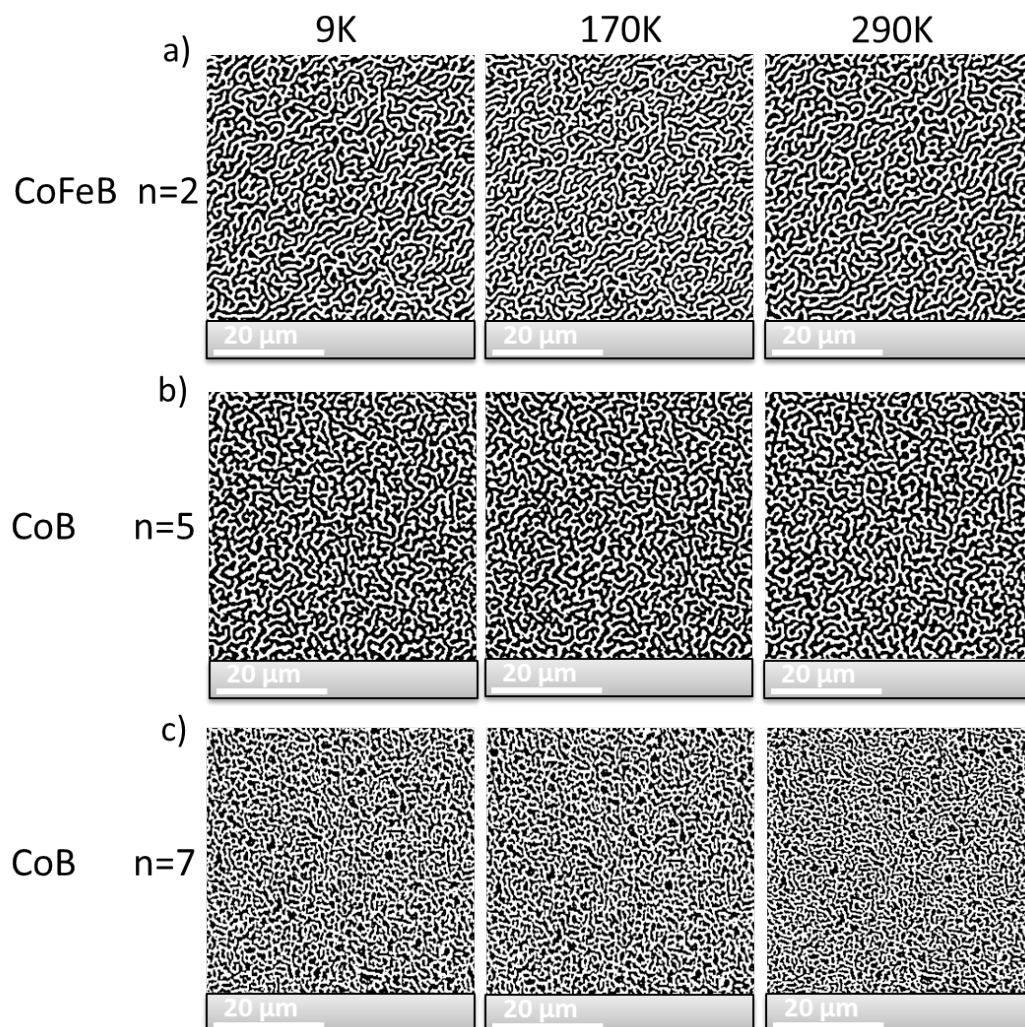


Figure 5.3: Demagnetised domain patterns imaged by Kerr microscopy at different temperature for (a) CoFeB ($n = 2$), (b) CoB ($n = 5$) and, (c) CoB ($n=7$). The images have been adjusted to display maximum contrast between up/down domains.

Briefly: a fast-Fourier transform of the image produces rings at a characteristic wavelength related to the maze domains. We extract this wavelength by radially averaging in reciprocal space and fitting a Gaussian function to the intensity. Transforming back into real space the peak of the function gives the average domain period (d) as shown in Figure 5.4.

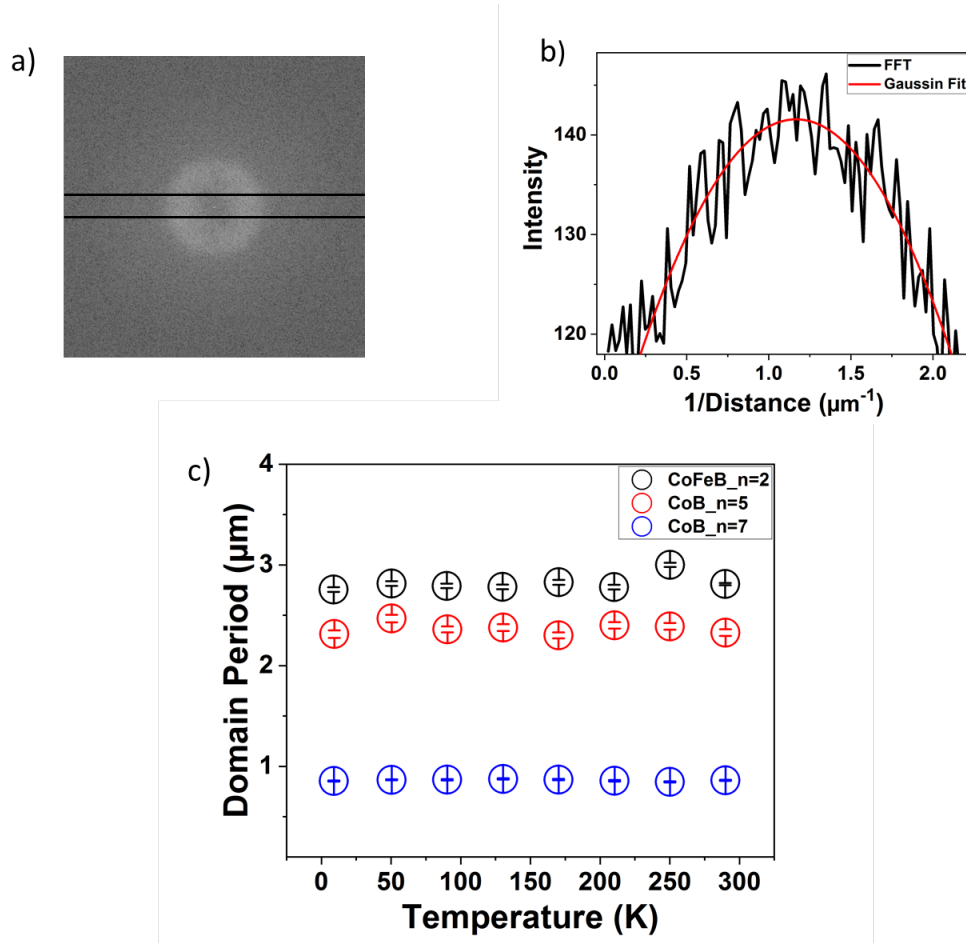


Figure 5.4: An area is spanned across the transformed image to plot two intensity peaks for all sides of the inner ring for CoB ($n=7$). b) Gaussian fit to the radial average peak intensity of the Fourier transform to extract the domain period. (c) Domain period vs. temperature for all three samples. Error bars are smaller than the data points.

Figure 5.3 shows typical demagnetised domain patterns at different temperature and the extracted domain period d (T) as a function of the temperature is shown in Figure 5.4. After performing a fast Fourier transform on the image, rings with a characteristic wavelength associated with the maze domains are produced. The circular average FFT was plotted at different angle ($0^\circ, 30^\circ, 60^\circ, 90^\circ, \dots, 360^\circ$) for CoFeB and CoB at all temperatures (9K-290K) and calculated the average of

domain period. The magnitudes and error bars of domain period for those angles are the same, which indicates that the domains are uniform and the error bars are small. Also, the domain period is the same area of white and black domains. The domain period does not change and is almost independent of temperature, because all the important parameters (A , K_u and D) have the same temperature dependence.

While the domain period is determined from images of the demagnetised domain pattern as a function of the temperature, enabling a calculation of domain wall energy density can be obtained from Equation 4.4 (Chapter 4). For each temperature we use $d(T)$, $M_s(T)$, and $K_{eff}(T)$ and calculate the domain wall energy density (in J/m^2) as shown in Figure 5.5.

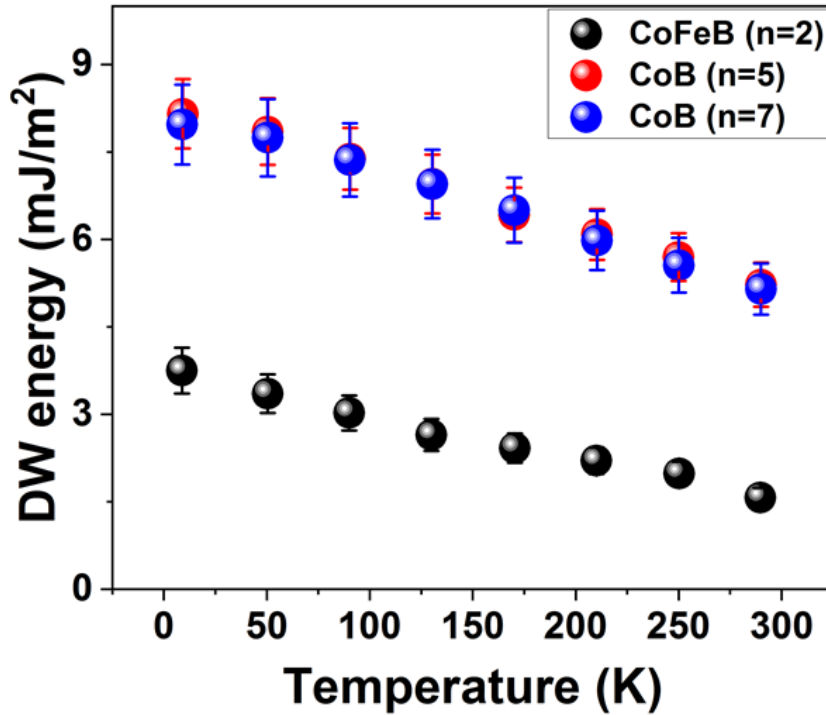


Figure 5.5: Domain wall energy density for the multilayer $[\text{Pt}/\text{CoFeB}/\text{Ir}]$ $n=2$ and $[\text{Pt}/\text{CoB}/\text{Ir}]$ $n=5$ and $n=7$.

5.3 Magnetic characterisation

Then we measured DMI by fitting an expression for the domain wall energy density, for which the inputs are temperature-dependent measurements of the effective perpendicular anisotropy K_{eff} , the exchange stiffness A and the domain wall energy density. We find D from the theoretical domain wall energy density [151].

$$|D(T)| = \frac{4\sqrt{A(T)K_{eff}(T)} - \sigma_{DW}(T)}{\pi} \quad (5.1)$$

Figure 5.6 exhibits the temperature-dependence of the DMI of CoFeB ($n=2$) and CoB ($n=5,7$) and the number of repeats for CoB does not necessarily affect the DMI as it was reported in Co/Ir [149].

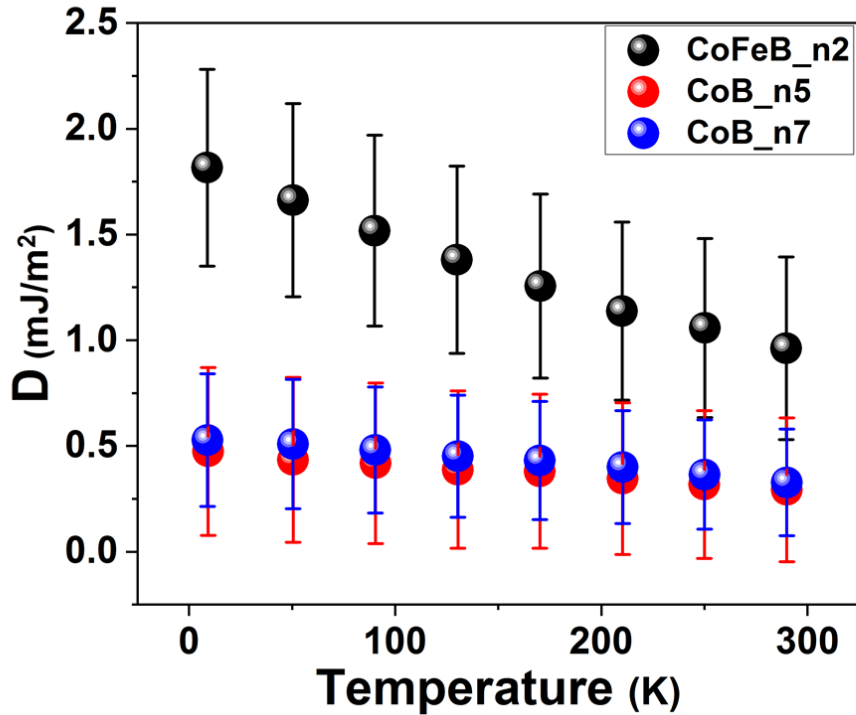


Figure 5.6: The temperature-dependence of DMI constant D for the multilayer [Pt/CoFeB/Ir] ($n=1$ and 2) and [Pt/CoB/Ir] ($n=5$ and 7).

In the Pt/CoFeB/Ir (n=2) multilayers that we study, the DMI varies between 1.0-1.8 mJ/m², depending on the temperature, while in the Pt/CoB/Ir (n=5 and 7) multilayers the DMI remains at 0.3-0.5 mJ/m². This analysis yields $D(T)$ for each sample (Figure 5.6). The uncertainty in A dominates the uncertainty in D . D for both CoB samples is the same within error, as expected, because the interfaces are the same and the only difference is the number of repeats. While the temperature dependence of DMI for the CoFeB sample is greater than that of the CoB samples in absolute terms, the relative change (50-60 %) is the same for both samples, which we can ascribe to the presence of Fe and also the smaller atomic percentage of B in the CoFeB sample. The DMI in the CoB samples is in the range of what might be expected given a previous measurement in a [Pt(1.0 nm)/Co₈₀B₂₀(0.7 nm)/Ir(1.0 nm)]n=6 multilayer [152]. The temperature dependence of the DMI for the CoFeB sample is also greater than that of the CoB samples.

5.4 The scaling of K_u , A and D with M_s

We find that K_u , A and D all scale close to the theoretically predicted behaviour, but that the scaling of the Pt/CoFeB/Ir is subtly different from that of the Pt/CoB/Ir. Table 5.4 lists the scaling parameters. Figure 5.7 shows K_u normalised by the low temperature value plotted against the normalised magnetisation. The gradient of the linear fit ranges from 1.88-2.09 for the different thin films, consistent with a power law scaling of $K_u \sim m^2$ for a two-ion interfacial anisotropy. Anisotropy decreases with increasing temperature in a power law $K_u(T)/K_u(T = 0) = m(T)^{l(l+1)/2}$, where $m = M_s(T)/M_s(0)$, the reduced magnetisation, and l is the order of the anisotropy. This result is derived from Callen- Callen theory [160].

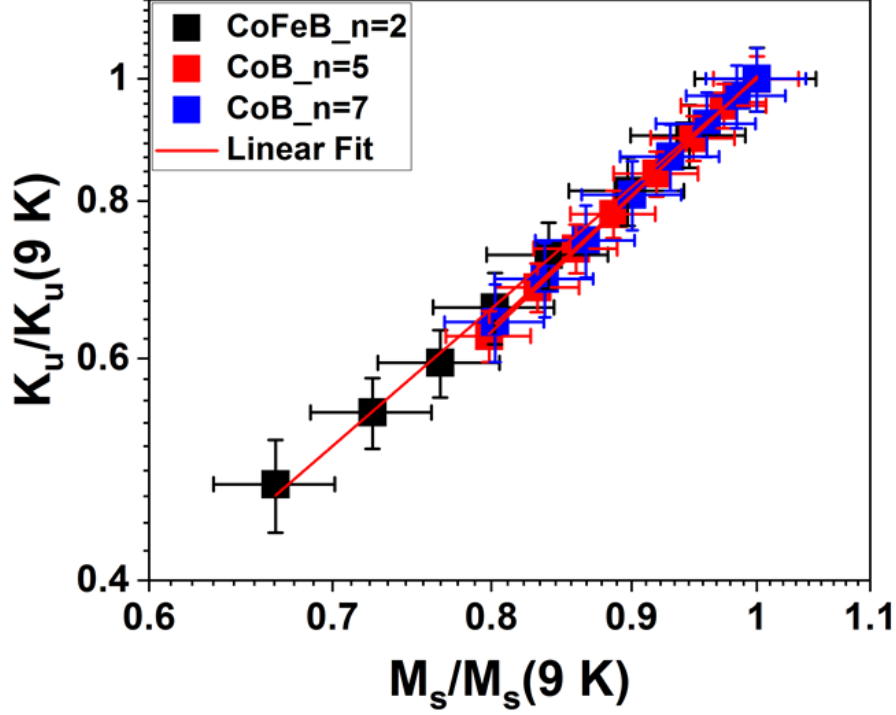


Figure 5.7: Scaling of the intrinsic perpendicular anisotropy K_u with MS. The solid red line represents the Callen-Callen scaling law $K_u \sim m^2$.

Table 5.4 Scaling exponents of the magnetic parameters for the three measured thin films. ” denotes theoretical value.

Sample	α	K	δ
CoFeB ($n = 2$)	1.80*	1.88 ± 0.03	1.65 ± 0.04
CoB ($n = 5$)	1.80*	2.09 ± 0.02	1.81 ± 0.09
CoB ($n = 7$)	1.80*	2.05 ± 0.02	1.86 ± 0.05

Although, there is not such a simple theory for the temperature dependence of the exchange stiffness and of the DMI but numerical simulations suggest that they

also follow power laws $A(T)/A(T=0) = m(T)^\alpha$ and $D(T)/D(T=0) = m(T)^\delta$ and that the exponents α and δ are the same [161][159][143]. While these works calculated $\alpha = 1.5$, the important conclusion that should be drawn from them is that $\alpha = \delta$. Figure 5.8 shows A normalised by the low temperature value plotted against the normalised magnetisation.

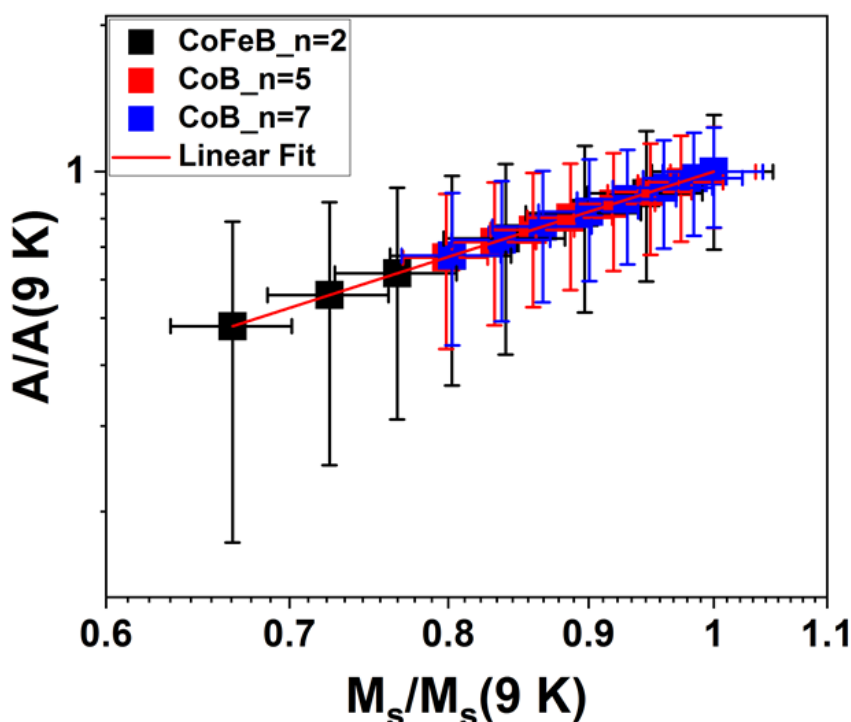


Figure 5.8: Scaling of A with M_s , normalised by the low temperature values. The solid red line represents $A \sim m^{1.8}$.

Figure 5.9 shows log-log plots of $D(T)$ normalised by the low temperature value against the normalised magnetisation. Linear fits yield the scaling exponents, which range from 1.65–1.86. The values of the scaling are nearly all the same within error.

The scaling for CoFeB($n=2$) is only lower than for CoB samples because the data is skewed by one point at room temperature. The scaling parameters are

close to the exchange stiffness scaling ~ 1.8 , and align with previous predictions and results [145][58].

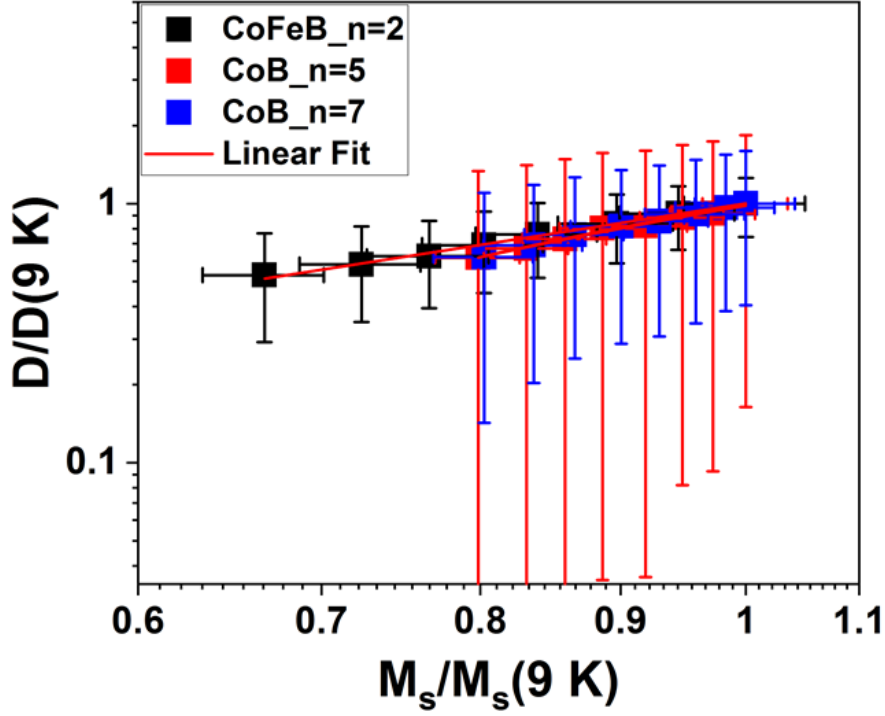


Figure 5.9: Scaling of D with M_s , normalised by the low temperature values. The solid red line represents $D \sim m^{1.8}$.

The similar scaling of K_u , A and D explains why the domain period is almost independent of temperature. In general the value of the exponent will vary depending on the choice of lattice. One experimental study on Pt/Co/Cu superlattices [162] finds $D(m) \sim m^{4.9}$, while another on [Pt/CoFeB/Ru]($n=2$) [145] measures $D(m) \sim m^{1.86}$. So far the study that found $m^{1.86}$ is realistic, while the study that found $m^{4.9}$ is far away from expectations.

5.5 Summary

We have measured the temperature dependence of the magnetisation, perpendicular anisotropy and demagnetised domain period in Pt/CoFeB/Ir (n=2) and Pt/CoB/Ir (n=5 and 7) multilayers. The domain period does not change significantly as the temperature is varied from 9-290 K. This result can only be obtained if A and D have the same temperature dependence, as predicted by theory. Assuming a scaling of $A \sim m^{1.8}$, we find that, approximately, $D \sim m^{1.8}$, and we report values for the DMI in these films across the temperature range. Pt/CoFeB/Ir exhibits a larger D and greater dependence of DMI on temperature than Pt/CoB/Ir in absolute change, but the relative change is about 50-60 %, which indicates both of them decrease by the same factor.

CHAPTER 6

Temperature dependence of
Dzyaloshinskii-Moriya interaction in
magnetic multilayers (in BTO substrate)

6.1 Introduction

Magnetic multilayers with perpendicular anisotropy and an interfacial Dzyaloshinskii-Moriya interaction contain chiral domain walls and skyrmions that are promising for use in computing. Here we measure the temperature dependence of the Dzyaloshinskii-Moriya interaction (DMI) and observe the domain pattern in Pt/CoFeB/Ir and Pt/CoB/Ir multilayers deposited on barium titanate, BaTiO₃, (BTO). At room temperature, stripe domains in the Pt/CoFeB/Ir film are tilted along the length of the BTO a-domains, perpendicular to the in-plane tensile strain. The BTO undergoes structural phase transitions at ~ 180 K and ~ 270 K and these introduce further in-plane strain which we deduce to be responsible for increasing the domain width in the Pt/CoFeB/Ir, as the temperature is increased over the range 13-320 K. This strain is also responsible for reducing the effective perpendicular anisotropy K_{eff} of the film, as compared to identical films grown on Si, and consequently for increasing the domain wall energy by 40 %.

By using static domain imaging, we investigate the temperature dependence of the Dzyaloshinskii-Moriya interaction (DMI) in Pt/CoFeB/Ir and Pt/CoB/Ir multilayers in two different substrates. To begin, the temperature dependences of saturation magnetisation (M_s), exchange stiffness (A), and intrinsic perpendicular anisotropy (K_u) are calculated separately, followed by the establishment of scaling laws for K_u and D with magnetisation. The demagnetised domain pattern in each multilayer is then imaged using wide-field Kerr microscopy throughout the temperature range 9-320 K, and the characteristic domain period is determined for each temperature. The DMI constant D is calculated analytically using a domain wall energy density equation that considers the multilayer as a uniform medium.

6.2 Samples

We have investigated two types of multilayers: (i) [Pt(2.3nm)/Co₆₈Fe₂₂B₁₀(0.55nm)/Ir(0.5nm)]_n (CoFeB multilayers) and (ii) [Pt(2.3nm)/Co₆₈B₁₀(0.76nm)/Ir(0.5nm)]_n (CoB multilayers) deposited by dc magnetron sputtering on a 3 nm Ta seed layer

on a thermally oxidised S_i and ferroelectric (BTO) substrates. To avoid oxidation, a 2.3 nm thick Pt capping layer was placed on top. The ferromagnet (FM) is made of amorphous CoFeB or CoB, which was first selected to prevent skyrmion pinning at grain boundaries. Pt and Ir were selected because they are expected to produce DMI with opposite sign at the top and bottom interfaces, resulting in a high net DMI, although this is debatable [156]. These samples have grown at a different times from the samples that were discussed (in Chapter 4). The number of repetitions n was adjusted between 1 and 6, and the samples were subsequently demagnetised with ac current, resulting in a labyrinth domain structure at zero field. Four samples were then chosen for further study based on their suitability for DMI measurement: those with a large number of domains within the typical field of view of a wide-field Kerr microscope (approximately $200\ \mu\text{m} \times 200\ \mu\text{m}$ square), sufficient to provide a reasonable statistical estimate of the domain period, but with domains that remained well resolved, no smaller than 1.15 - 2.2 μm . Thus, CoFeB ($n = 2$) and CoB ($n = 4$) samples on SiOx and BTO substrates were chosen.

6.3 Magnetic characterisation

As inferred from Figure 6.1.(a), the samples show perpendicular magnetic anisotropy, which may be detected using a magneto-optical Kerr effect magnetometer with a polar configuration that is sensitive to out-of-plane magnetic fields. To get the DMI's temperature-dependent value, we begin by extracting the M_s , A , K_{eff} , and K_u , as shown in Figure 6.1. (b, c,d, and e). The saturation magnetisation was determined using hard axis in-plane hysteresis loops over the temperature range 9–320 K, and the exchange stiffness at low temperatures was determined by fitting a modified version of the Bloch $T^{3/2}$ law for thin films to normalised SQUID-VSM moment versus temperature data. After assuming a power law scaling of $A(m) \sim m^{1.8}$, the temperature dependence of A was extrapolated from the low temperature value [143]. The effective perpendicular anisotropy K_{eff} was determined by integrating the area of in-plane SQUID-VSM hysteresis loops and dividing it by the volume of the sample; the intrinsic perpendicular anisotropy K_u was then computed by accounting for the shape anisotropy term $\frac{1}{2}\mu_0 M_s^2$.

6.3 Magnetic characterisation

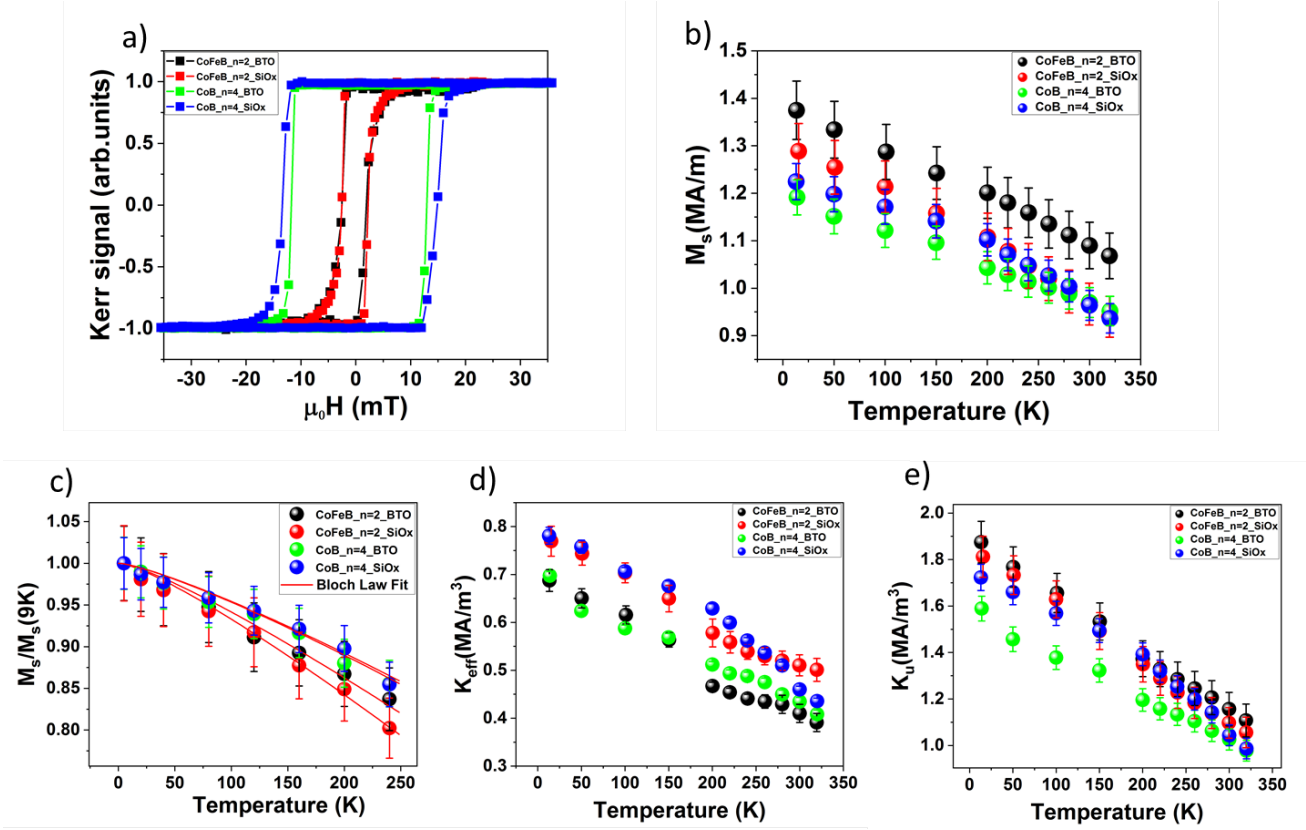


Figure 6.1: a) Measurement of hysteresis loops at room temperature using the magneto optic Kerr effect with an out-of-plane field. b) In the temperature range 13-320 K, the saturation magnetisation was determined using SQUID-VSM hysteresis loops in an in-plane (hard-axis) configuration. c) Temperature dependence of saturation magnetisation normalised to the low temperature value and the solid lines represent fitted data using Equation 4.2 in (Chapter 4). d) Effective anisotropy (K_{eff}) and e) intrinsic perpendicular anisotropy (K_u) for temperatures ranging from 13 to 320 K.

Hysteresis loops at room temperature (300 K) with different materials and substrates are shown in Figure 6.1.(a). CoFeB ($n=2$), in both substrates, follows the same shape and exhibits a wasp shape due to changes in magnetic layers. Also, CoB ($n=4$) follows the same shape and shows a square polar hysteresis loop, and all the samples confirmed the out-of-plane character of Co(Fe)B.

Figure 6.1.(c) depicts the $M_s(T)/M_s(13K)$ results for CoFeB ($n = 2$) and CoB ($n = 4$) multilayers, respectively. Using Equation 4.2 in (Chapter 4) to fit the data, we can get the low temperature value of the exchange stiffness A for each sample, which is shown in Table (6.3) below. As illustrated in Figure 6.2, we can extrapolate the temperature dependence of A using the power law scaling $A(T)/A(13K) = (M_s(T)/M_s(13K))^{1.8}$ from theory [143] to obtain the temperature dependence of A .

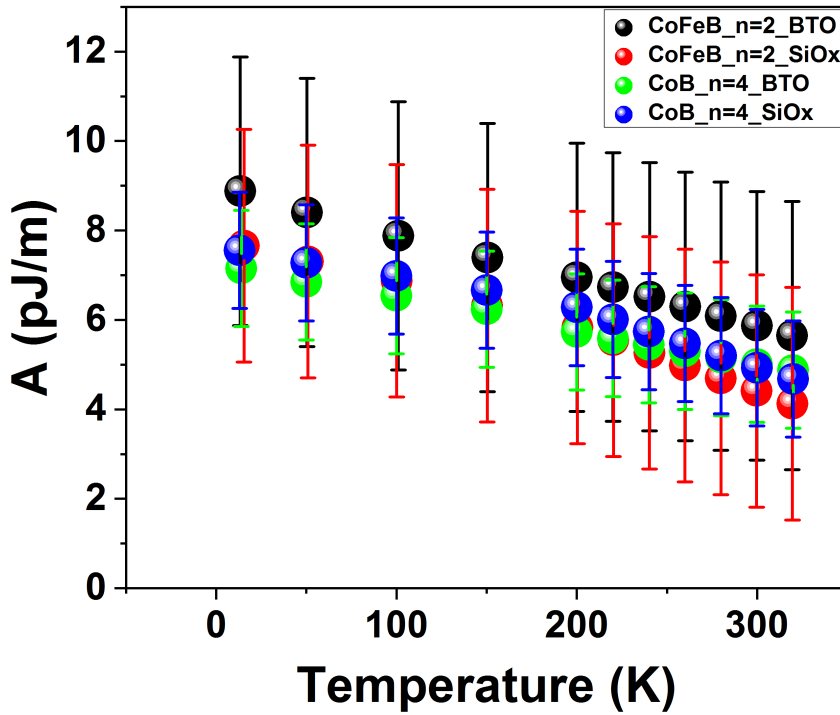


Figure 6.2: : The exchange stiffness for CoFeB ($n=2$) and CoB ($n= 4$) onto BTO and SiOx substrates, using Bloch's law for thin films in the temperature range 13-320 K. Exchange stiffness decreases with increasing temperature due to renormalisation of the magnon spectrum by the thermal magnons.

The exchange stiffness at low temperatures was obtained by fitting a normalised SQUID-VSM moment versus temperature data to a modified version of

6.3 Magnetic characterisation

the Bloch $T^{3/2}$ law for thin films. Bloch's law defines exchange stiffness as the value at zero temperature. As shown in Figure 6.2 exchange stiffness decreases as the temperature increases due to renormalisation of the magnon spectrum by the thermal magnons [158]. According to theory and experiment, the exchange stiffness scales roughly power law with the temperature dependent magnetisation, where the exponent relies on the lattice geometry [159]. We utilise $A(T)/A(0) = A(m) \sim m^{1.8}$ in our study, which is consistent with theory [143].

Table 6.3. Extracted low temperature values of magnetic parameters for the four measured thin films.

Sample	$M_s(13\text{ K})\text{MA/m}$	$A(9\text{ K})\text{pJ/m}$	$K_{\text{eff}}(9\text{ K})\text{MA/m}^3$	$K_u(9\text{ K})\text{MA/m}^3$	$D(9\text{ K})\text{mJ/m}^2$
CoFeB (n=2) BTO	1.37 ± 0.06	9 ± 3	0.69 ± 0.03	1.87 ± 0.09	2 ± 0.5
CoFeB (n=2) SiOx	1.29 ± 0.06	8 ± 3	0.77 ± 0.03	1.81 ± 0.09	1.98 ± 0.50
CoB (n=4) BTO	1.19 ± 0.04	7 ± 1	0.69 ± 0.01	1.59 ± 0.05	0.6 ± 0.3
CoB (n=4) SiOx	1.22 ± 0.04	8 ± 2	0.78 ± 0.02	1.72 ± 0.06	0.78 ± 0.30

The uncertainty in the anisotropy is mostly attributable to measurement errors in the volume of the sample, which is divided into the hysteresis loop area in order to determine K_{eff} .

After determining the M_s , A , and K_{eff} , we calculated the magnetic domain period in the temperature range 13-320 K using wide-field Kerr microscopy images of the demagnetised domain pattern. In this case, the demagnetising process was the same to the one that was described in (Chapter 5.3). Then, using a method similar to that used by Agrawal et al.[139], we were able to extract the domain period from these images, as shown in Figure 6.3 and 6.4.

6.3 Magnetic characterisation

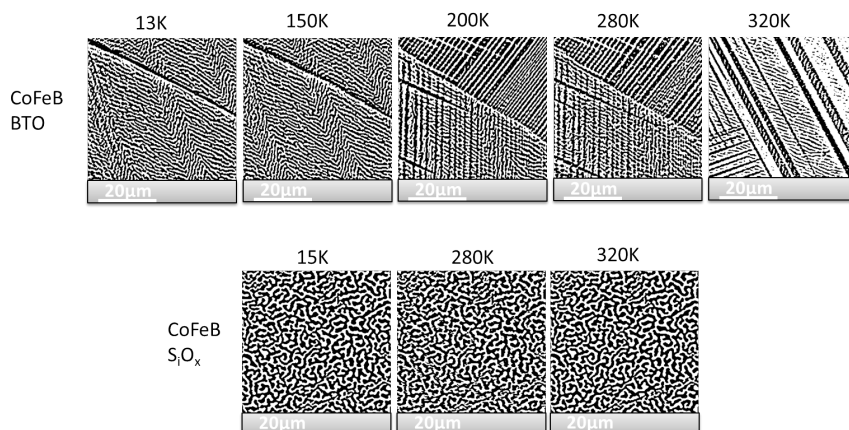


Figure 6.3: a) Kerr microscopy images of demagnetised domain patterns for CoFeB ($n = 2$) sample across the temperature range on BTO, with three from CoFeB ($n = 2$) sample on SiO_x for comparison. The BTO domains of CoFeB ($n=2$) appears as stripes of approximately equal width in the rhombohedral phase and as stripes of unequal width (but identical direction) in the tetragonal phase. Adjustments have been made to the images to maximise contrast between the up/down domains.

As mentioned before in Chapter (5.3), a fast Fourier transform of the images generates rings with a wavelength typical of the labyrinth domains. We determine the wavelength by radially averaging in reciprocal space and fitting the intensity to a Gaussian function. When the function is transformed back to real space, the peak of the function yields the average domain period (d), as shown in Figure 6.5.

6.3 Magnetic characterisation

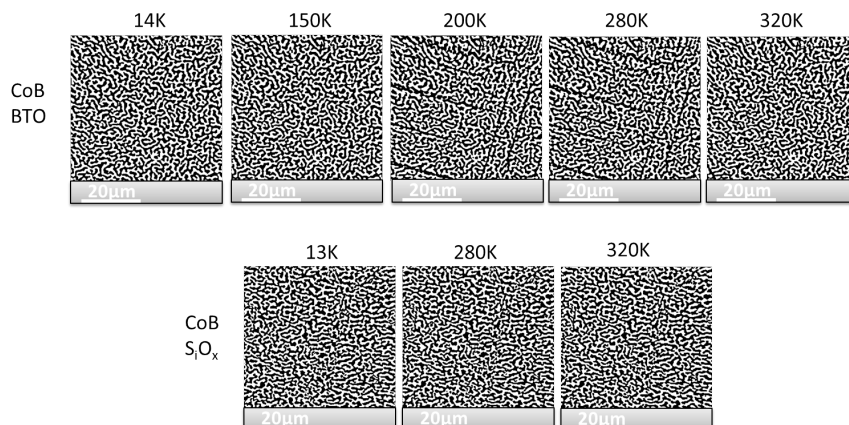


Figure 6.4: Kerr microscopy images of demagnetised domain patterns for CoB ($n = 4$) sample across the temperature range on BTO, with three from CoB ($n = 4$) sample on SiO_x for comparison. The BTO domains of CoB($n=4$) and SiO_x CoB ($n=4$) approximately are the same size and no effect from the temperature. Adjustments have been made to the images to maximise contrast between the up/down domains.

While the domain period is calculated from images of the demagnetised domain pattern as a function of temperature, the domain wall energy density can be obtained from Equation 4.4 in (Chapter 4). According to Figure 6.5, for each temperature, we utilise the parameters $d(T)$, $M_s(T)$, and $K_{eff}(T)$ to compute the domain wall energy density (in J/m^2), which is displayed in the graph (Figure 6.6).

6.3 Magnetic characterisation

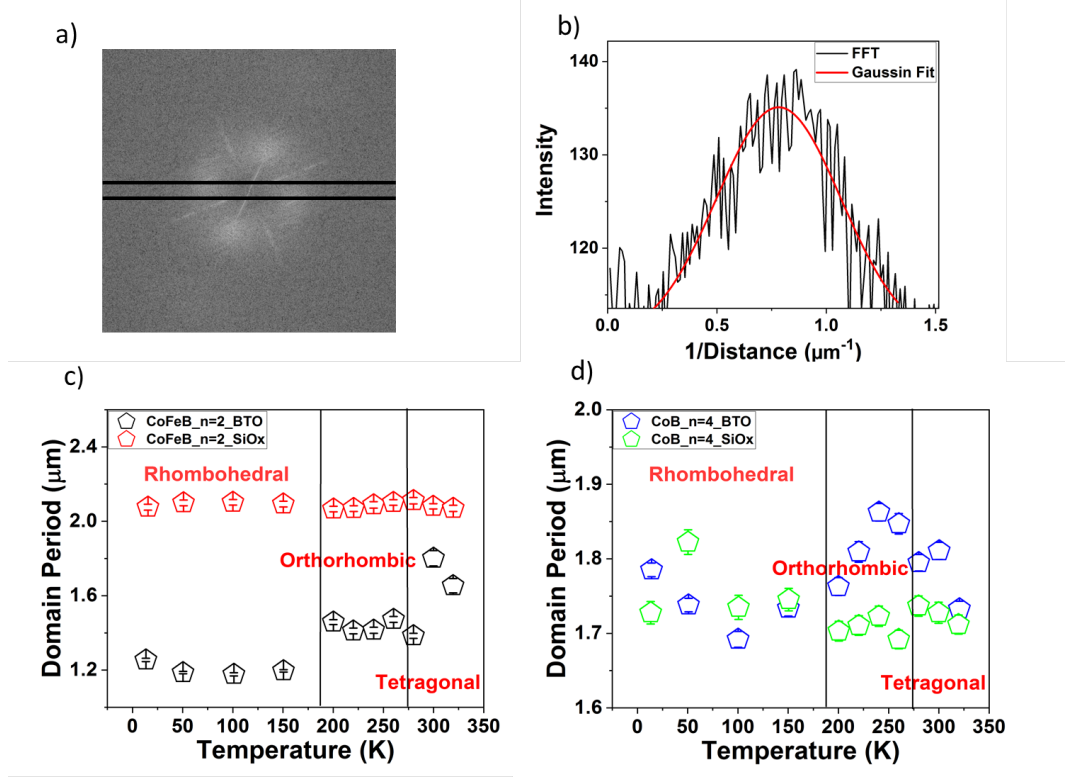


Figure 6.5: a) An area is spanned across the transformed image to plot two intensity peaks for all sides for CoFeB ($n=2$) in BTO and due to the stripe domains the FFT pattern is not any more a ring. substrate and . b) Gaussian fit to the radial average peak intensity of the Fourier transform to extract the domain period. c) Domain period vs. temperature for CoFeB ($n=2$) and CoB ($n=4$) in BTO substrates with phase transitions of BTO as functions of temperature. d) Domain period vs. temperature for CoFeB ($n=2$) and CoB ($n=4$) in SiOx substrates. Error bars are smaller than the data points.

After that, we measured DMI by fitting an equation for the domain wall energy density, where the inputs are temperature-dependent measurements of the effective perpendicular anisotropy K_{eff} , the exchange stiffness A , and the domain wall energy density, respectively. The theoretical domain wall energy density [151]. is used to calculate D .

The DMI of the Pt/CoFeB/Ir ($n=2$) multilayers we investigate fluctuates

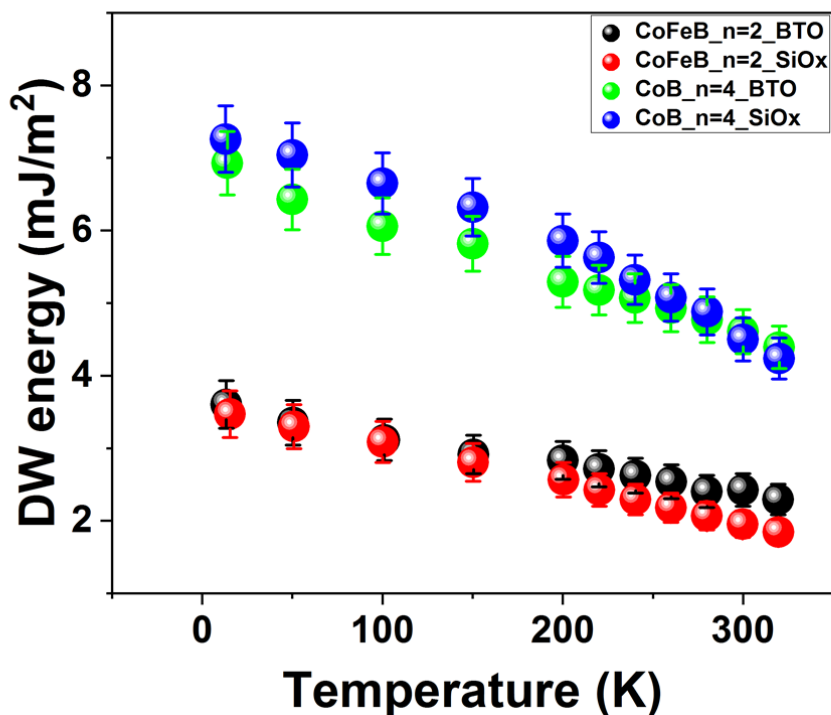


Figure 6.6: Domain wall energy density for the multilayer [Pt/CoFeB/Ir] $n=2$ and [Pt/CoB/Ir] $n=4$ in BTO and SiOx substrates.

between 1.15 and 1.99 mJ/m², depending on the temperature and substrate, while the DMI of the Pt/CoB/Ir ($n=4$) multilayers remains between 0.39 and 0.78 mJ/m². This analysis yields $D(T)$ for each sample and the uncertainty in A dominates the uncertainty in D . Figure 6.7 shows that the DMI for CoFeB on BTO and SiOx are the same within error, and that the DMI for CoB on BTO and SiOx are the same within error. The DMI of the CoFeB sample is larger than that of the CoB sample in absolute change but the relative change is the same, which we may attribute to the presence of Fe and also to the CoFeB sample having a lower atomic percentage of B. The DMI values in the CoB samples are within the range predicted by a prior measurement [152]. Temperature dependence of the DMI is significantly higher for the CoFeB sample than for the CoB sample.

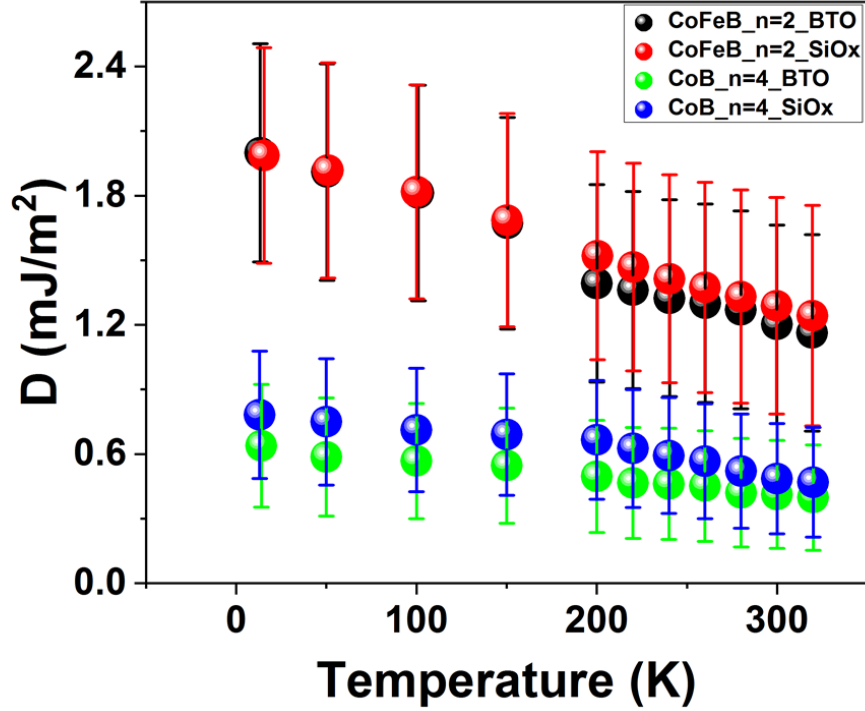


Figure 6.7: Exhibits the temperature-dependence resulting DMI constant D of CoFeB ($n=2$) and CoB ($n=4$) into BTO and SiOx substrates.

6.4 Discussion

The Figure 6.3.(a).(b) illustrates typical demagnetised domain patterns at various temperatures. The first image of CoFeB (BTO) was taken at room temperature (the tetragonal phase) before we went down to low temperature (13K) as shown in Figure 6.8.(a). Then we increased the temperature to 320 K. Now for the temperature dependence of the BTO we measured from ~ 13 K to 320K, spanning the rhombohedral (R) (0-175K), orthorhombic (O) (175-270K), and tetragonal (T) (270-390K) structural phases as presented in Figure 6.8.(b). The ferroelectric domains of BTO ($n=2$) appear as stripes of roughly equal width in the rhombohedral phase, and unequal width (but same direction) in the tetragonal phase.

So in the tetragonal phase, we suppose that the BTO domains are a -type (narrow) and c -type (wide) and that the ferromagnetic stripe domains are tilted along “ a ” domain length, perpendicular to the in-plane stress (1.1% tensile), following Fackler et al [85]. In the rhombohedral phase we deduce that the BTO domains are a_1 and a_2 -type [85]. The BTO domains change direction in going from a_1 to a_2 -type (rhombohedral phase) and also in going from a to c -type (tetragonal phase).

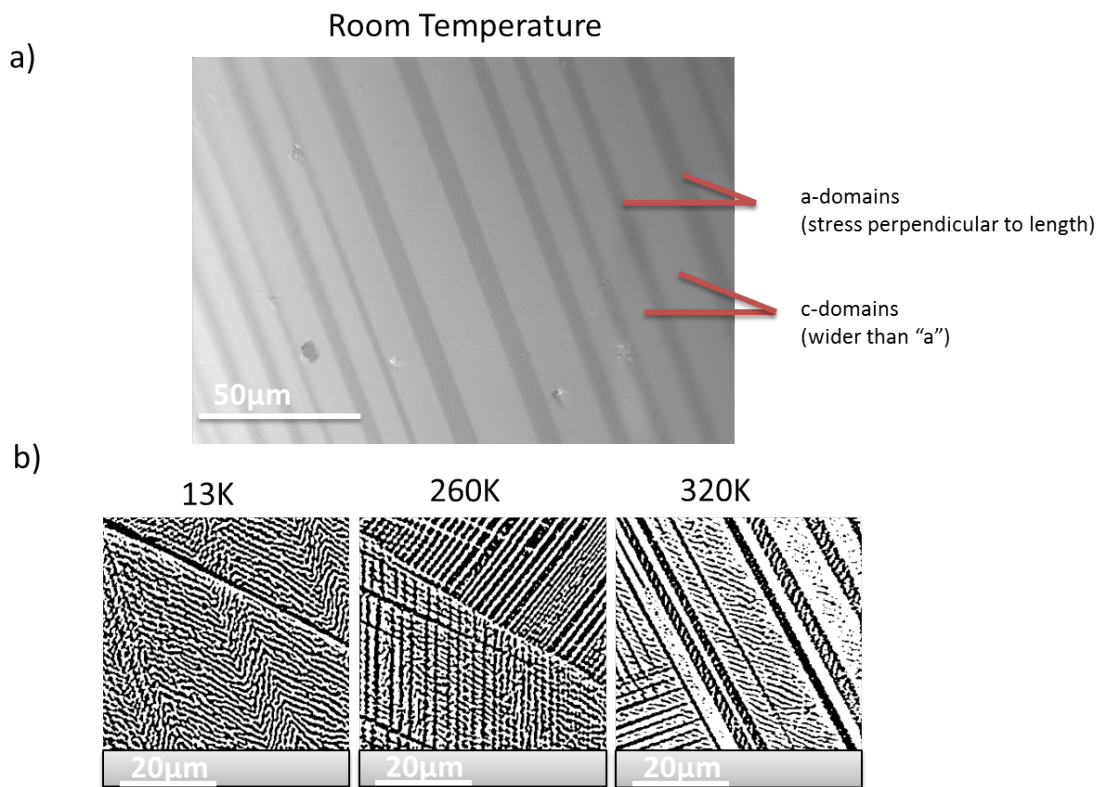


Figure 6.8: Kerr microscopy images of demagnetised domain patterns for CoFeB ($n = 2$) sample across the temperature range on BTO. a) The first image of CoFeB (BTO) was taken at room temperature before we went down to low temperature. b) Three images of CoFeB ($n=2$) at different phase transition for BTO.

Films are then cooled to LT and R-phase. In ferromagnetic/ferroelectric heterostructures that show domain pattern transfer, the anisotropy direction at the

abrupt 90° is changed on top of narrow ferroelectric domain boundaries results in significant pinning of magnetic domain walls. This is because strain is transferred during the ferroelectric phase transition, which occurs when the temperature is changed. 90° degree change in stripe direction is preserved but proportions of areas are different and probably commensurate with body diagonal polarised BTO domains. The surface lattice squares become diamonds so there is a little stress but it is not as much as on “ a ” domains in the T-phase.

The domain pattern seen in the rhombohedral phase is slowly broken in the orthorhombic phase, until there is a sudden change back to the original pattern with the switch of the BTO to tetragonal phase near room temperature.

The imprint of the BTO domains is only seen for CoFeB and not for CoB and that maybe due to the CoFeB has a larger magnetostriction as it has been measured in Chapter (7). Figure 6.5 (c) demonstrates that the domain period in CoFeB/BTO is less than the domain period in CoFeB/Si. This is due to the fact that K_{eff} is less. The domain period increases abruptly in CoFeB/BTO as the BTO changes through the phases R-O-T. This is not due to any change in M_s or A and therefore must be due to applied stress which increases domain period, and reduces K_{eff} a little bit (any change in in-plane anisotropy reduces the (K_{eff}) , as we know from previous work [2].

In both CoFeB/BTO and CoFeB/Si, the domain wall energy is the same at low temperature. This is due to the fact that, although M_s is higher for CoFeB/BTO, domain period is less, and so things seem to be more balanced in this regard. When the BTO goes orthorhombic, the domain wall energies diverge, which is most likely due to a decrease in (K_{eff}) at that point in the BTO.

Additionally, we see that the scaling of (K_u) , A , and D is consistent with the theoretically expected behaviour, but that the scaling of Pt/CoFeB/Ir is somewhat different from that of Pt/CoB/Ir. The scaling parameters are shown in Table 6.4. K_u normalised by the low temperature value is shown versus normalised magnetisation in Figure 6.5 (a and b). The scaling for CoFeB/SiOx ($n=2$) is only lower than other samples (1.77) because we have the steps in the data. Also, we have got two scaling parameters from two parts of the data (1.78 and 1.96) for CoFeB/BTO ($n=2$) which are actually more or less the same within error (1.87).

The gradient of the linear fit varies between 2.08 and 2.09 for CoB on SiOx and BTO, which is consistent with a power law scaling of $K_u \sim m^2$ for two-ion interfacial anisotropy. The anisotropy reduces with increasing temperature according to the power law $K_u \sim m^2$.

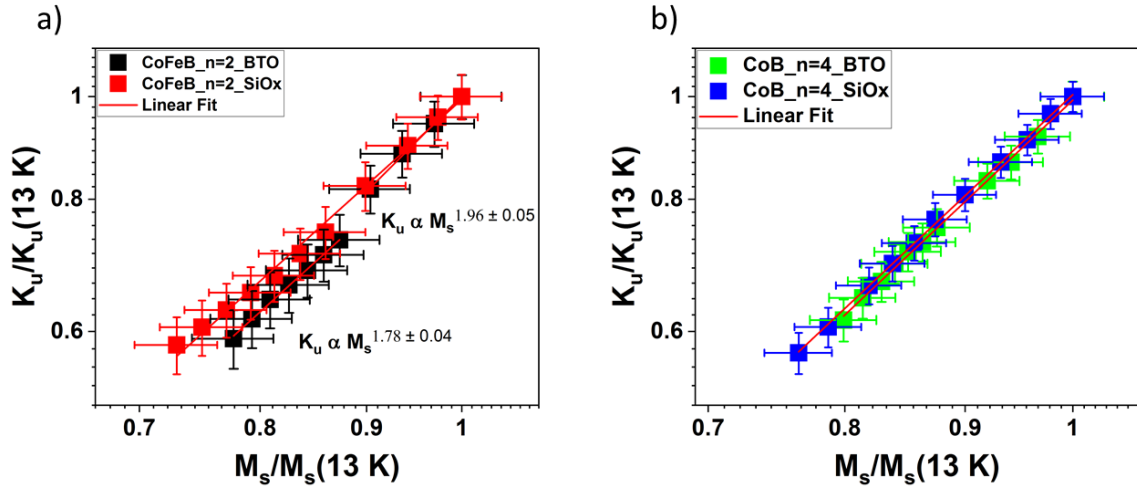


Figure 6.9: a) and b) Scaling of the intrinsic perpendicular anisotropy K_u with M_s for CoFeB and CoB into BTO and SiOx. The solid red line represents the Callen-Callen scaling law $K_u \sim m^2$.

Values of the exchange stiffness as a function of temperature are then extrapolated using the power law scaling $A/A_{13K} \propto (M_s/M_{13K})^{1.8}$ from theory [161][159][143]. The temperature-dependence of A is then plotted as A/A_{13K} versus the normalised saturation magnetisation. The gradient of a linear fit to the data on a log-log plot yields the scaling close to the theoretical value of 1.8, as expected.

Table 6.4 Scaling exponents of the magnetic parameters for the four measured thin films. * denotes theoretical value.

Sample	α	K	δ
CoFeB ($n = 2$) BTO	1.80*	2.14 ± 0.05	2.00 ± 0.13
CoFeB ($n = 2$) SiOx	1.80*	1.77 ± 0.04	1.60 ± 0.05
CoB ($n = 4$) BTO	1.80*	2.09 ± 0.03	1.87 ± 0.05
CoB ($n = 4$) SiOx	1.80*	2.08 ± 0.02	1.74 ± 0.08

The log-log graphs of $D(T)$ normalised by the low temperature value against the normalised magnetisation are shown in Figure 6.10. The scaling exponents, which vary from 1.60 to 2.08, are determined using linear fits. Scaling for CoFeB ($n=2$) in BTO is higher than for CoFeB ($n=2$) in SiOx samples due to the temperature effect on the phase transitions in BTO as shown Figure 6.10 .(a). Whereas the scaling parameters within error for CoB ($n=4$) are close to the exchange stiffness scaling factor of 1.8 in both substrates and they are consistent with earlier predictions and observations [145][58], as shown in Figure 6.10 (b).

The exchange stiffness scaling factor of 1.8 does not lie in the quoted range of uncertainty for any of the D scaling parameters for CoFeB samples. CoFeB/BTO is the obvious outlier, and it is because we have the steps in the data, where it doesn't really make sense to fit across the whole T range. We have got two scaling parameters from two parts of the data (1.5 and 1.72) (CoFeB/BTO) which are actually more or less the same within error (~ 1.6), as shown in Figure 6.10 .(a). Thus, the 1.6 average we have got in the table for (CoFeB/SiOx) is probably about right, but it is definitely then less than 1.8, especially in the non-rhombohedral phase. However, the whole discrepancy may be due to the difference in measured M_s . So the result is that the scaling of (D and K_u) are unchanged by the substrate, and close to what was found in Chapter 5.

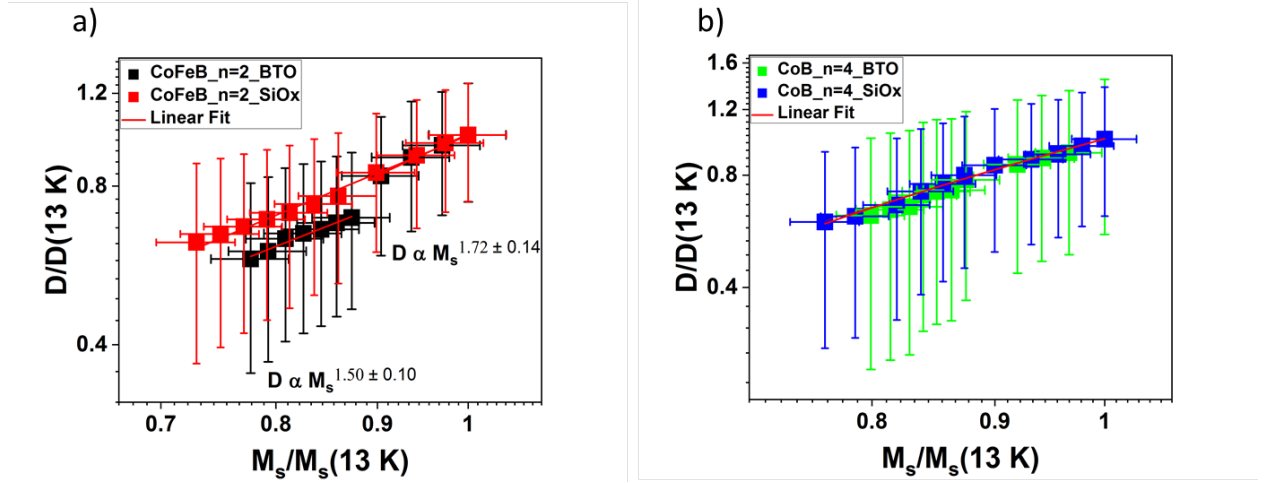


Figure 6.10: a) Scaling of D with M_s , normalised by the low temperature values with a separate fit to different phase transitions for CoFeB/BTO. The solid red line represents $D \sim m^{1.8}$ for all the samples. b) Scaling of D with M_s , normalised by the low temperature values for CoB ($n=4$) in BTO and SiOx.

6.5 Summary

The temperature dependence of magnetisation, perpendicular anisotropy, and demagnetised domain period has been determined in multilayers of Pt/CoFeB/Ir ($n=2$) and Pt/CoB/Ir ($n=4$) in BTO and SiOx substrates.

The BTO undergoes structural phase transitions at 180 and 270 K, introducing additional in-plane strain that we infer is responsible for the increasing domain width in the Pt/CoFeB/Ir when the temperature is increased throughout the range 13-320 K. Additionally, this strain reduces the effective perpendicular anisotropy K_{eff} of the film as compared to similar films grown on SiOx, increasing the domain wall energy by 40%.

Consequently, the scaling of (D and K_u) is unaffected by the substrate, while in CoFeB the values of K_{eff} and domain period vary when the phase changes, resulting in the transformation of domains into stripes.

CHAPTER 7

Anisotropy Measurements under Strain

7.1 Introduction

This chapter comprises the measurement of magnetic anisotropy field ($\mu_0 H_k$) of Pt/CoFeB/Ir and Pt/CoB/Ir multilayers under application of strain. The samples have been grown on glass substrates and glued to biaxial piezoelectric transducers. A method based on the extraordinary Hall effect (EHE) is used in measuring the magnetic anisotropy field. The polar hysteresis loops were taken for Pt/CoFeB/Ir and Pt/CoB/Ir and the saturation magnetisation is calculated. The strain effects on the anisotropy field, through coupling the films to the piezoelectric transducers, is described and the magnetostriction constant subsequently is measured. The next section discusses the multilayers system investigated.

7.2 Multilayer system

The following multilayer systems investigated are Ta(3nm)/[Pt(2.3nm)/Co₆₈Fe₂₂-B₁₀(0.51nm)/Ir(0.5nm)]_n/Pt(2.3nm) and Ta(3nm)/[Pt(2.3nm)/Co₆₈B₃₂/Ir(0.5nm)]_n/Pt(2.3nm), which were grown on 150 nm thick glass substrates and deposited by dc magnetron sputtering. The thicknesses of the layer are expressed in nm and 'n' representing the number of Pt/CoFeB/Ir and Pt/CoB/Ir layers in the thin film. In addition, the number of the Pt/CoFeB/Ir and Pt/CoB/Ir layers were changed between n=1 and n=10. The polar MOKE was used in the characterisation of all the samples to display perpendicular magnetic anisotropy due to a large interface contribution (Figure 7.1.(a)). Besides, the moment of the samples were measured by SQUID-VSM to calculate the saturation magnetisation M_s (Figure 7.1.(b)). The multilayers were then bonded to the biaxial piezoelectric transducers using epoxy resin. Application of voltages between 0 V and 150 V to the transducers can be used to induce strain. In addition, a positive voltage applied to the biaxial transducer produces a biaxial compression in the sample plane as well as a corresponding out-of-plane tensile strain (see Chapter 3 for more details on the strain).

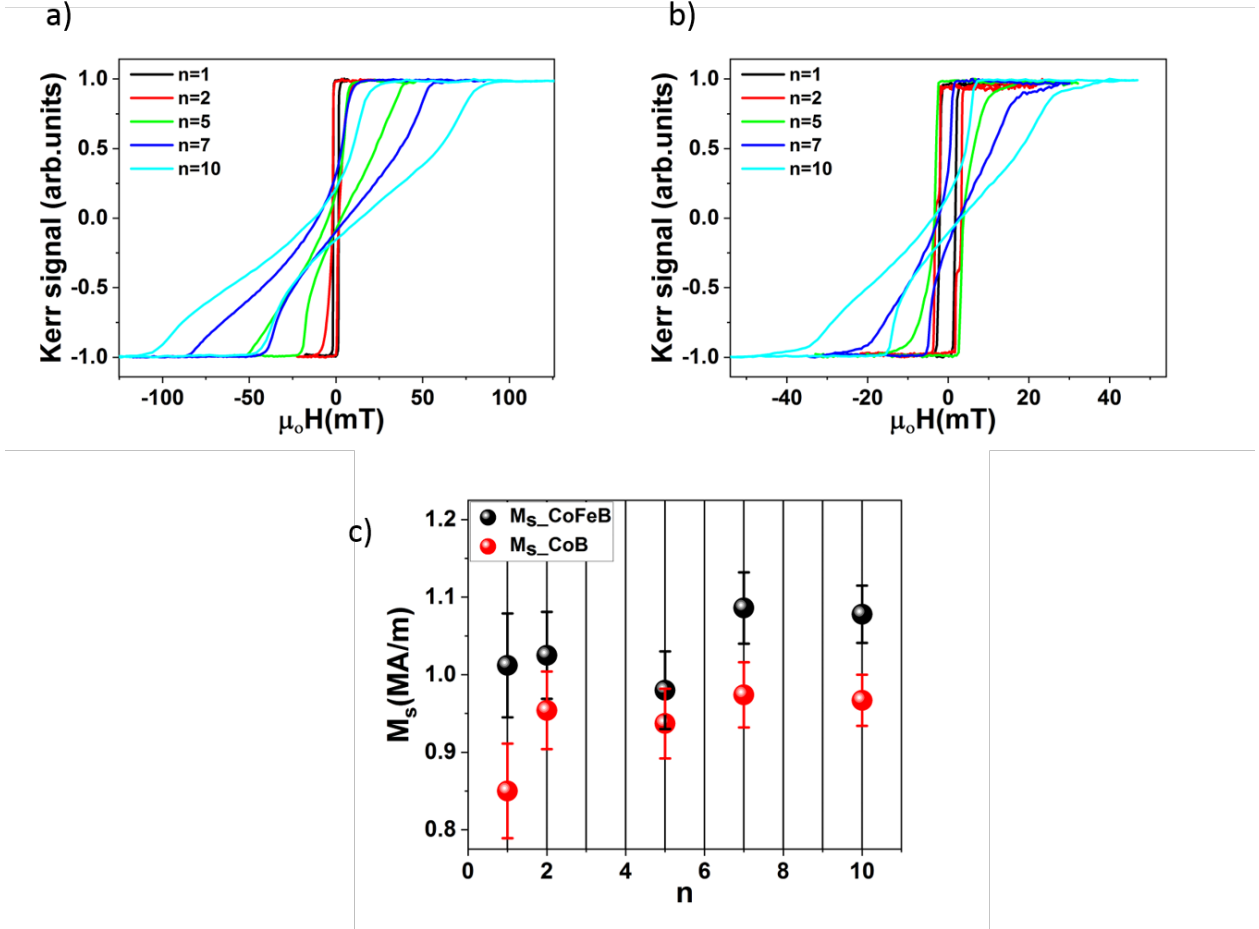


Figure 7.1: a) A $[\text{Pt}/\text{CoFeB}/\text{Ir}]_n$ Polar MOKE hysteresis loops with different repeats (these samples were grown on glass). At ($n < 2$) displays a square hysteresis loop and sharp switching. With an increasing number of layers, ($2 \leq n \leq 10$), the hysteresis loops develop a wasp shape due to changes in magnetic layers. b) A $[\text{Pt}/\text{CoB}/\text{Ir}]_n$ Polar MOKE hysteresis loops with different repeats. The hysteresis loops are square and sharp switching until $n = 5$ repeats and started a wasp-like from $5 \leq n \leq 10$. c) Saturation magnetization (M_s) of Pt/CoFeB/Ir and Pt/CoB/Ir with various repeats.

7.3 Anisotropy Measurements

The anisotropy field is the field needed for a coherent rotation of the magnetisation from the easy axis to the hard axis. Figure 7.2 illustrates a schematic of the sample

7.3 Anisotropy Measurements

measurement geometry. In measuring the dependence of the sweeping angle ϕ_H on the magnetisation angle (θ), a 500 mT constant external field is applied normal to the film. Then, the sample is followed by 5° rotation increments with the rotation axis of the film, parallel to the current flow.

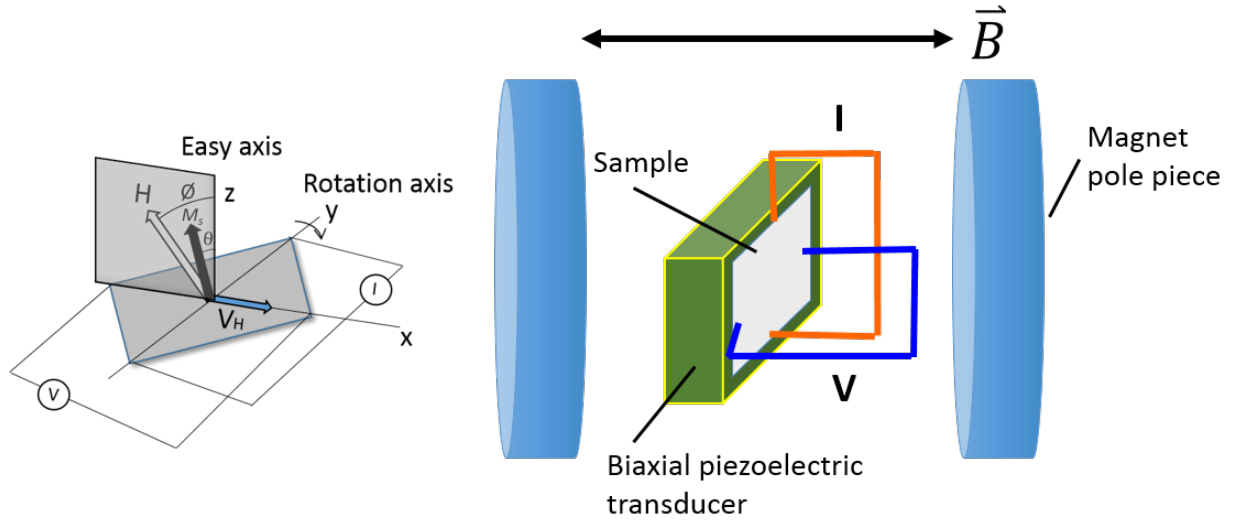


Figure 7.2: A schematic representation of measurement geometry and a sample on a transducer.

In this procedure, the ordinary Hall voltage is easily subtracted. The ordinary Hall Effect creates a signal that is proportional to $H \cos \phi_H$ during one sweep between -180° to 180° , with the amplitude is linearly dependent on the external field. Thus, the subtraction of the ordinary Hall voltage can exactly be done when various applied fields are measured. A plot of normalised extraordinary Hall voltage against the sweeping angle ϕ_H as shown in Figure 7.3 allows extraction of a quadratic equation from the data points around the minimum value. The data is picked at the maximum values of ± 180 , followed by between 60° in 5 increments. This makes it possible to obtain the Fourier coefficient A_2 as well as the calculation of anisotropy field H_k from A_2 by applying Equation 4.1.

It is important to make it clear that, regardless of the CoFeB and CoB, the anisotropy field found to decrease with an increase in the number of layers based

7.3 Anisotropy Measurements

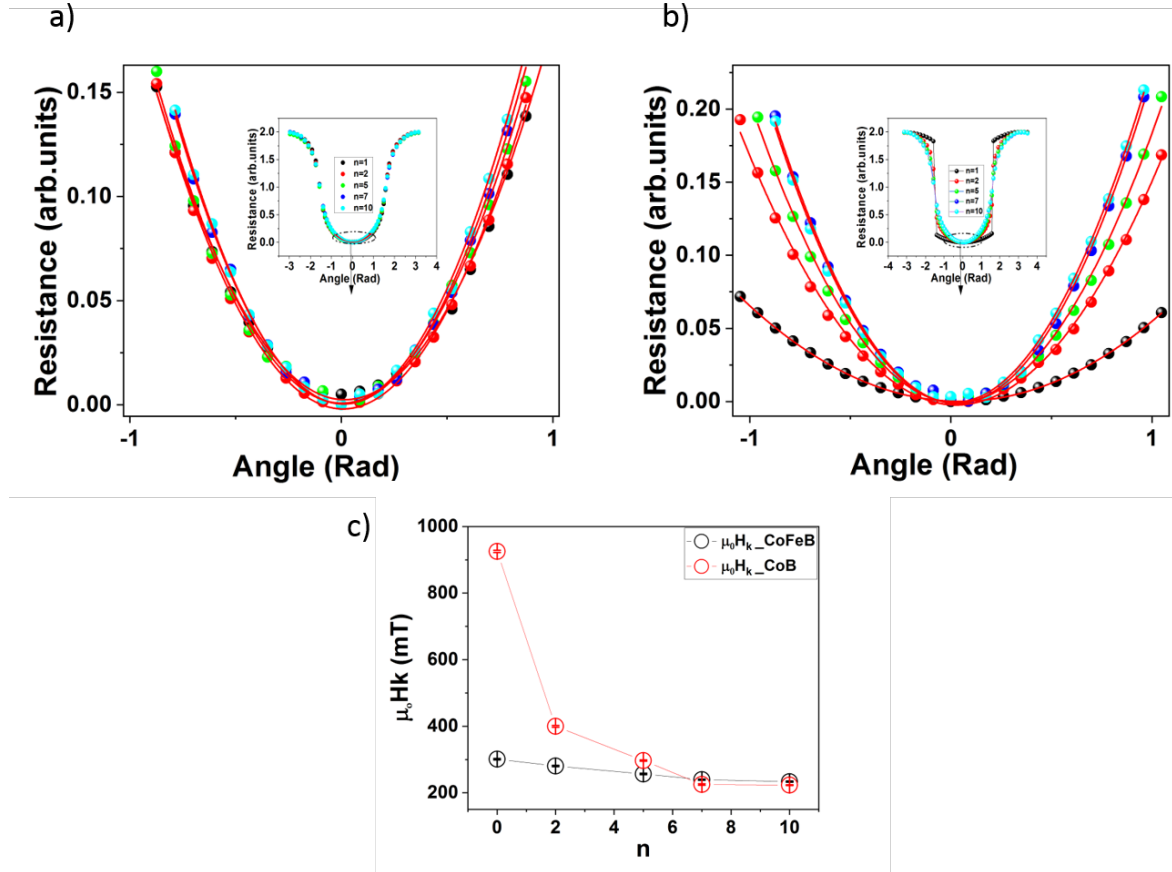


Figure 7.3: Normalised resistance against the sweeping angle in a 500mT constant external field and the inset in *a* and *b* are one sweep between -180° to 180° . *a*) A polynomial fit was applied to the data to help in extracting the quadratic function for CoFeB on a glass substrate with different repeat. *b*). A polynomial fit was applied to the data to help in extracting the quadratic function for CoB on a glass substrate with different repeat. *c*) Anisotropy field reduced with an increasing number of repeats for both CoFeB and CoB, and the solid line is a guide to the eye.

on the observations of the samples where a fit was applied (Figure 7.3).(c). As assessed, the largest anisotropy field obtained when the sample possessed $n=1$. On the other hand, the smallest was obtained for the sample $n=10$. So basically the same conclusion as the films were grown on SiOx. The observed diminishing

of the anisotropy field with an increase in the number of layers results from the roughness of the surface, which increases with every successive layer. A range of factors can explain the origin of the surface roughness, including nanocrystalline misorientation, non-smooth Ta layer, as well as accumulative defects that result in interface anisotropy decrease [140]. Various studies have shown that multilayers possessing atomic misfit at the interface exhibit a large PMA as well as high thermal stability; therefore, for high magnetocrystalline anisotropy, a smooth base layer is an essential requirement [136].

7.4 Anisotropy Measurements with strain

A voltage was applied across the piezoelectric transducer to strain a film with the strain adding a magnetoelastic contribution to the magnetic anisotropy. In this section, the influence of strain on Pt/CoFeB/Ir Pt/CoB/Ir from the biaxial transducer is investigated. Moreover, a magnetostrictive ferromagnet, which can cause changes in the magnetic anisotropy when strained, will be measured of these samples.

7.4.1 Pt/CoFeB/Ir and Pt/CoB/Ir on biaxial transducer

It is usually prudent to carry out a test on the transducers prior to bonding samples to them. Various ways can be used to accomplish the testing. For instance, by attaching the leads to a digital voltmeter (for example, Keithley) that can suitably be used to measure small voltage signals as well as to detect small changes in voltage. Secondly, one can apply a full voltage cycle and check that the capacitive behaviour, when the voltage is slowly ramped, by measuring the current and seeing its decay. The current should be a few microamps decaying over a few second when the voltage is applied. The resistance and the calculated strain were measured against a transducer voltage applied for the biaxial transducers with Pt/CoFeB/Ir and Pt/CoB/Ir. Every Pt/CoFeB/Ir and Pt/CoB/Ir repeat have a measured maximum strain of $\varepsilon_z \sim 9 \times 10^{-4}$ and 1×10^{-3} .

As mentioned earlier, through rotating the sample by 5° between every measurement, with respect to the magnetisation angle (θ) and sweeping angle ϕ_H ,

7.4 Anisotropy Measurements with strain

the magnetisation can be obtained via the EHE. The out-of-plane magnetisation describes a parabolic path if rotated in a constant field with coherent magnetisation rotation. However, in the case where the field is increased or a rotation is done to the sample to a large sweeping angle ϕ_H , reversing the magnetisation, then the EHE signal deviates from the parabolic path. Then, the EHE signal is normalised between 2 and 0, which allows the parabola quadratic term A_2 to be obtained from the data.

The biaxial transducers afford a strain (biaxial in-plane) that can be considered as a uniaxial out-of-plane strain. An application of a voltage across the transducers is predicted to cause a change in PMA.

From Figures 7.4 and 7.5, it is clearly observed that there is an anisotropy field reduction between the transducer at 0 and 150 V for Pt/CoFeB/Ir and Pt/CoB/Ir. The anisotropy field measurements were carried out for the transducer voltages in 15 V steps from 0V to 150 V. Then, the anisotropy field is plotted against the transducer voltage for [Pt/CoFeB/Ir] $_n$ with $n = 1, 2, 5, 7, 10$ repeats (Figure 7.5). The anisotropy field reduces in a linear manner with applied transducer voltage, exhibiting a change of ~ 12 mT over the voltage ranges for every repeat of Pt/CoFeB/Ir.

7.4 Anisotropy Measurements with strain

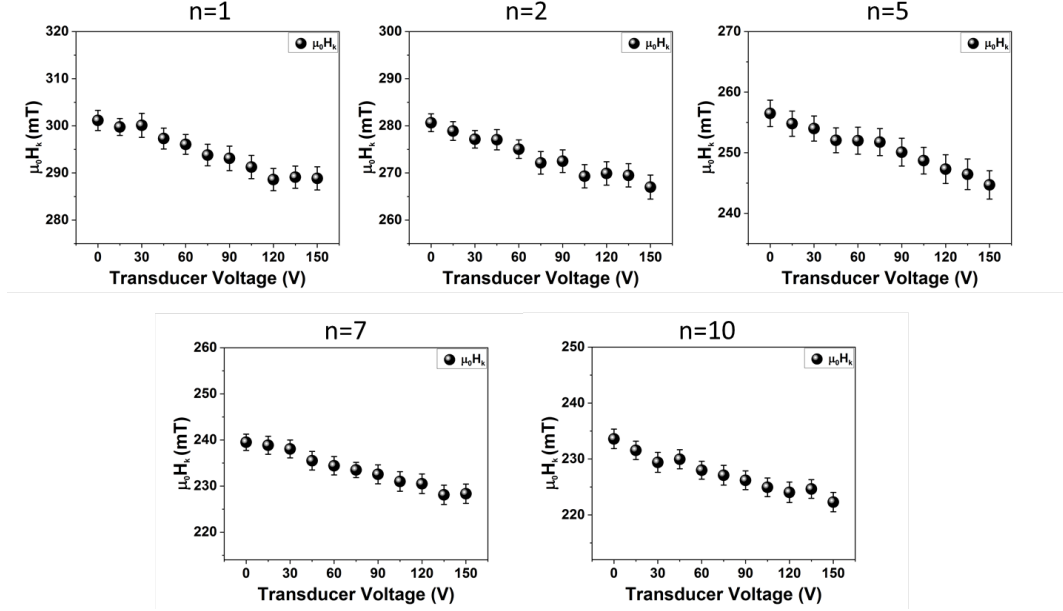


Figure 7.4: Plots of the magnetic anisotropy field against biaxial transducer voltage for $[\text{Pt}/\text{CoFeB}/\text{Ir}]_n$ multilayers ($n = 1, 2, 5, 7, 10$). Three measurements are averaged to give each data, and the error bars are standard errors on the mean values.

Equation 4.1 was used in calculating the magnetic anisotropy field, which decreases with an increase in repeat Pt/CoFeB/Ir from (301 ± 2) mT for $n=1$ to (233 ± 2) mT for $n=10$. The reduction in $\mu_0 H_k$ implies that the thickness of CoFeB increases consistently and that the thickness scale sub-nanometer precision is valid.

In addition, using the same procedure, it is observable in Figure 7.5 that an application of a voltage to the transducer to produce strain on the Pt/CoB/Ir film leads to a change in the anisotropy field. At a small repeat, where $n=1$, the anisotropy field appeared to be constant when changing the voltage as compared to other repeats. Besides, the anisotropy for Pt/CoB/Ir $n=1$ is a large anisotropy where the strain may be not large enough to cause anisotropy changes. For others repeats, $n=2, 5, 7, 20$, the anisotropy field reduces in a linear manner with applied transducer voltage, showing a change of ~ 9 mT over the voltage ranges for every

7.4 Anisotropy Measurements with strain

repeat of Pt/CoB/Ir.

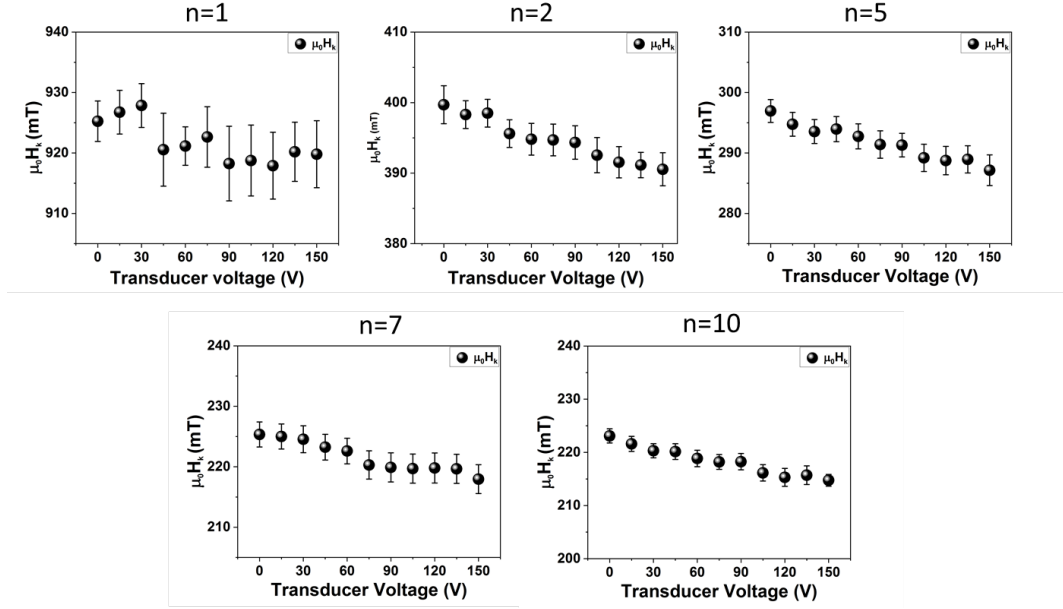


Figure 7.5: Plots of the magnetic anisotropy field against biaxial transducer voltage for $[\text{Pt}/\text{CoB}/\text{Ir}]_n$ thin films ($n = 1, 2, 5, 7, 10$). Three measurements are averaged to give each data, and the error bars are standard errors on the mean values.

7.4.2 Magnetostriction of Pt/CoFeB/Ir and Pt/CoB/Ir

The magnetostrictive materials in the form of thin films have become increasingly vital in the development of actuators and sensors. Applying a strain to the magnetostrictive ferromagnet offers a degree of control over the material's magnetic anisotropy energy. In the recent past, there has been continued interest in having control of perpendicular magnetic anisotropy in the thin films through strain from piezoelectric material [163][23][164][165]. In addition, the measurement of the ensuing magnetic anisotropy changes permits a calculation of magnetostriction. The magnetostriction constant A is calculated from the changes of the magnetic anisotropy field induced by strain with applied stress. The anisotropy field change is then expected to be, as shown in Equation 7.1 below:

7.4 Anisotropy Measurements with strain

$$\Delta H_k = \frac{3Y\lambda\varepsilon}{M_s} \quad (7.1)$$

where λ is the magnetostriction constant, ε is the strain and Y is Young's modulus.

From the gradient in Figure 7.6, a graph of anisotropy field plotted against tensile out-of-plane strain ($dH_k/d\varepsilon_z$), the value of the slope gives the magnetostriction value of the Pt/CoFeB/Ir and Pt/CoB/Ir with various repeats by applying Equation 7.1. It is vital to note that from the findings, a negative intercept indicated that the easy axis was perpendicular to the strain applied. Comparatively, a positive intercept indicated that the easy axis of the film was originally along the applied strain direction. Each CoFeB and CoB give a different change per unit of strain.

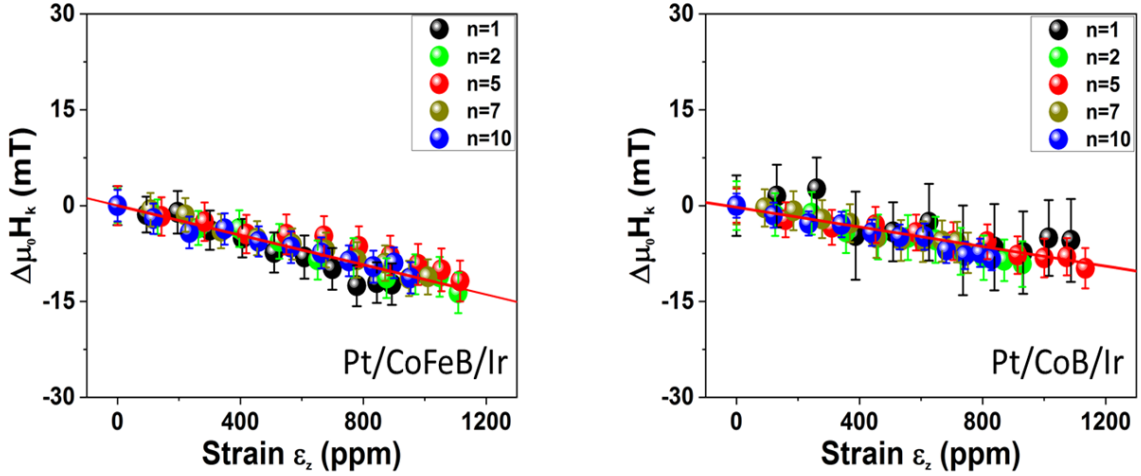


Figure 7.6: a) and b) are the change in the anisotropy field of Pt/CoFeB/Ir and Pt/CoB/Ir with different repeats due to out-of-plane strain z induced by biaxial transducers. The solid line is a fit of the data to Equation 2.

The Pt/CoFeB/Ir and Pt/CoB/Ir magnetostriction constant is found from a least-squares fit of the anisotropy field change to the Equation 7.1 with Y treated as the bulk Pt and Co Young's moduli averages (180 GPa) [165]. The change in magnetostriction constant (λ) with various systems and repeats is shown in

7.4 Anisotropy Measurements with strain

Figure 7.7 . It is also clear that Pt/CoFeB/Ir films have higher magnetostriction constants as compared to Pt/CoB/Ir. The Pt/CoFeB/Ir n=1 showed the highest λ of -28 ± 2 ppm, and increasing the number of repeats up to n=10 leads to a slight decrease to -21 ± 2 ppm. In the case of Pt/CoB/Ir films, the magnetostriction constant was nearly constant between (-13 ± 3) ppm and (-18 ± 2) ppm, even though the values were still lower than those of the Pt/CoFeB/Ir films. Therefore, the introduction of Fe into the CoB thin films increased the magnetostriction constant by lowering the space between the atoms since the radius of the Fe atom is moderately low.

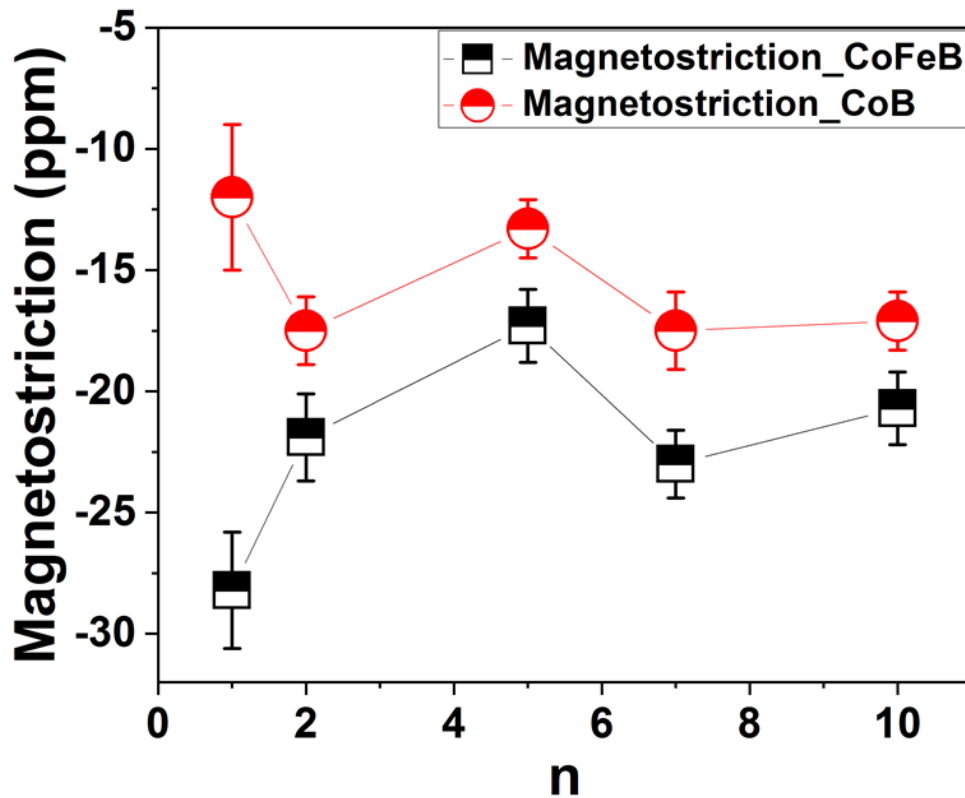


Figure 7.7: The magnetostriction constant of Pt/CoFeB/Ir and Pt/CoB/Ir with different repeats . The solid line is a guide to the eye.

The magnetostriction constant measured is slightly lower than the bulk Co value for $\lambda = -50$ ppm and a slight change with number repeats. Furthermore, the Pt/Co/Pt magnetostriction of -35 ppm has been found in previous study [30]. Besides, the $\text{Co}_{60}\text{Fe}_{20}\text{B}_{20}$ alloys magnetostriction has been examined, and the obtained results are close to those that we got for CoFeB and CoB [166]. Due to the fact that CoPt alloys magnetostriction increases from negative values at low concentrations of Pt to positive values at high concentrations of Pt [167], the negative magnetostriction constant that we got shows that there is a little intermixing at the Pt/CoFeB and Pt/CoB interface. Contrasting a study of Pt/Co multilayers, which observed substantial interface effects to the magnetostriction [165], volume type magnetostriction of CoFeB and CoB indicates that the magnetostriction of Pt/CoFeB/Ir and Pt/CoB/Ir comes mostly from the bulk-like Co volume. The magnetostriction and PMA are both related to the magnetocrystalline anisotropy that comes from the spin-orbit coupling and crystal field [38]. The electron orbitals of the Co atoms are distorted by strain. The bulk-like Co orbital distortion has in the Pt/CoFeB/Ir and Pt/CoB/Ir obtained here, a larger effect on the magnetic anisotropy as compared to the distortion of the hybridized Pt 5d orbitals and Co 3d orbitals that direct the anisotropy out-of-plane component. The out-of-plane anisotropy is constant under the piezoelectric strain, while the in-plane bulk anisotropy varies.

7.5 Summary

In conclusion, the magnetic properties of the Pt/CoFeB/Ir and Pt/CoB/Ir samples grown on glass substrates have been investigated. The samples display a perpendicular magnetic anisotropy because of a large anisotropy interface contribution. An increase in the number of layers results in an increase in the switching field, with the polar hysteresis loops becoming more diagonal. In addition, the changes in the saturation magnetisation with respect to the repeats were obtained.

A method based on the EHE has been used in measuring Pt/CoFeB/Ir and Pt/CoB/Ir multilayers magnetic anisotropy field. Identification of a coherent magnetisation rotation at a constant field was done, which can be fitted to obtain the anisotropy field.

From the obtained measurement of the change of the anisotropy field in Pt/CoFeB/Ir and Pt/CoB/Ir under biaxial transducers induced strain was shown that tensile strain along a particular axis lowers the magnetic anisotropy constant. The measurement of Pt/CoFeB/Ir and Pt/CoB/Ir magnetostriction constant showed that CoFeB films have higher magnetostriction constant than CoB films. Additionally, the variation in the anisotropy field with strain was found to be caused by bulk-like Co atoms and not the interface with the Pt.

CHAPTER 8

Conclusions

This thesis studied the magnetic properties, temperature dependence and magnetostriction constant of Pt/CoFeB/Ir and Pt/CoB/Ir multilayers. The background of the work and the theoretical ideas have been discussed and the pertinent experimental techniques have been described. The purpose of this study was to investigate the magnetic properties of Pt/CoFeB/Ir and Pt/CoB/Ir and how the properties can be changed upon application of the strain by changing the temperature and from a piezoelectric transducer.

Chapter 4 described the magnetic properties of CoFeB and CoB multilayers with different repeat ($n=1 - n=20$) of Pt/CoFeB/Ir and Pt/CoB/Ir have been characterised by using polar laser MOKE measurements (hysteresis loops), the magneto-optical Kerr effect (domain period (d)), MR-rig (H_k) and SQUID (M_s, A and K_{eff}). The magnetic domains for CoFeB and CoB were imaged at room temperature using Magneto-Optical Kerr effect. The magnetic domains for CoFeB show a maze domain and get smaller when the repeats, $5 \leq n \leq 7$, are increased. While the magnetic domains for CoB, at the small repeat $n \leq 2$, show bubbles domain. At $5 \leq n \leq 10$ the domains become small and form as maze domain. Further increase, $12 \leq n \leq 20$, the domains become too small and hard to see. Furthermore, a technique is based on static domain spacing in the equilibrium state used to determine the domain wall energy, which leads to estimate the DMI with very few assumptions. The resulting DMI of CoB is less than CoFeB, and the number of repeats does not affect the DMI.

Chapter 5 presented the measurement of the temperature dependence of DMI in Pt/CoFeB/Ir ($n=2$) and Pt/CoB/Ir ($n=5$ and 7) multilayers deposited on SiOx. We measure DMI by fitting an expression for the domain wall energy density, for which the inputs are temperature-dependent measurements of the saturation magnetisation M_s , the exchange stiffness A , the effective perpendicular anisotropy K_{eff} and the domain period d . The low temperature exchange stiffness is determined by fitting an expression for Bloch's law in a thin film to $M_s(T)$, while the domain period is determined from images of the demagnetised domain pattern obtained by wide-field Kerr microscopy in the temperature range 9-290 K. The domain period does not change significantly as the temperature is varied from 9-290 K. This result can only be obtained if A and D have the same temperature dependence, as predicted by theory. Assuming a scaling of

$A \sim m^{1.8}$, we find that, approximately, $D \sim m^{1.8}$. Pt/CoFeB/Ir exhibits a larger D and greater dependence of DMI on temperature than Pt/CoB/Ir, which we ascribe to the presence of Fe and the smaller at% of B in the former.

In Chapter 6 we measured the temperature dependence of DMI and observe the domain pattern in Pt/CoFeB/Ir ($n=2$) and Pt/CoB/Ir ($n=4$) multilayers deposited on barium titanate, BaTiO₃, (BTO). At 180 and 270 K, the BTO structural phase changes, introducing additional in-plane strain that we conclude is responsible for the increasing domain width in the Pt/CoFeB/Ir when the temperature is increased between 13 and 320 K. Moreover, this strain reduces the effective perpendicular anisotropy K_{eff} of the film as compared to similar films grown on SiOx, increasing the domain wall energy by 40%.

Chapter 7 showed the magnetic anisotropy of the Pt/CoFeB/Ir and Pt/CoB/Ir multilayers grown on glass substrates and then attached to piezoelectric transducers in order to measure the magnetic properties under strain. All the samples with different repeats have a measured maximum strain between $\sim 9 \times 10^{-4}$ and 1×10^{-3} which is consistent with the estimated strain in the transducer at the voltage of 1×10^{-3} . The measurement of Pt/CoFeB/Ir and Pt/CoB/Ir magnetostriction constant showed that CoFeB films have higher magnetostriction constant than CoB films. Additionally, it was determined that the anisotropy field fluctuation with strain is produced by bulk-like Co atoms rather than the interface with the Pt.

To continue the work of this project, we investigate to further our study by imaging at a larger number of repetition and temperature set points for superlattices containing either Pt/CoB/Ir or Pt/CoFeB/Ir on standard silicon substrates SiOx and on BTO. The XMCD-PEEM experimentation could be performed to identify the atoms at the interface and investigate the resulting domain structure, since while the latter is suitable for smaller domains ($<1 \mu\text{m}$) imaged in superlattices with large n . The high quality images of domains that we will obtain will enable us to determine the temperature dependence of the domain width in a systematic way and, with sufficient number of temperature set points, would allow us to properly compare with available theoretical models of the temperature dependence of D . Also, It is good to use bubble expansion method to measure the DMI, CoB $n=1$ and 2, and compare the results with static domain imaging.

Using uniaxial transducers and measure the effective anisotropy K_{eff} as function of strain. This part involves measuring the PMA field under applied strain of Pt/CoFeB/Ir and Pt/CoB/Ir thin films grown on glass substrates and BTO. The aim of this measurement is to determine if application of strain will lead to change in the magnetic anisotropy and compare the results with biaxial transducers.

References

- [1] R. Skomski, *Simple models of magnetism*. Oxford University Press on Demand, 2008. [xi](#), [7](#)
- [2] P. M. Shepley, *Effect of piezoelectric strain on the magnetic properties of Pt/Co thin films*. PhD thesis, University of Leeds, 2015. [xi](#), [7](#), [115](#)
- [3] M. Johnson, P. Bloemen, F. Den Broeder, and J. De Vries, “Magnetic anisotropy in metallic multilayers,” *Reports on Progress in Physics*, vol. 59, no. 11, p. 1409, 1996. [xi](#), [6](#), [7](#), [9](#), [11](#)
- [4] R. A. Khan, *Chiral Spin Textures in Magnetic Nanostructures*. PhD thesis, University of Leeds, 2018. [xi](#), [12](#)
- [5] W. Legrand, J.-Y. Chauleau, D. Maccariello, N. Reyren, S. Collin, K. Bouzehouane, N. Jaouen, V. Cros, and A. Fert, “Hybrid chiral domain walls and skyrmions in magnetic multilayers,” *Science advances*, vol. 4, no. 7, p. eaat0415, 2018. [xi](#), [13](#), [14](#)
- [6] W. Eerenstein, N. Mathur, and J. F. Scott, “Multiferroic and magnetoelectric materials,” *nature*, vol. 442, no. 7104, pp. 759–765, 2006. [xii](#), [20](#), [21](#)
- [7] K. Franke *et al.*, “Domain wall coupling in ferromagnetic/ferroelectric heterostructures: Scaling behaviour and electric field driven motion,” 2016. [xii](#), [26](#)
- [8] S. Bennett, A. Wong, A. Glavic, A. Herklotz, C. Urban, I. Valmianski, M. Biegalski, H. Christen, T. Ward, and V. Lauter, “Giant controllable magnetization changes induced by structural phase transitions in a metamagnetic artificial multiferroic,” *Scientific reports*, vol. 6, no. 1, pp. 1–7, 2016. [xii](#), [27](#), [31](#)

REFERENCES

- [9] R. Schäfer, “Investigation of domains and dynamics of domain walls by the magneto-optical Kerr-effect,” *Handbook of magnetism and advanced magnetic materials*, 2007. [xiii](#), [39](#), [40](#)
- [10] Q. Design, “Magnetic property measurement system squid vsm evercool option user’s manual,” *Quantum Des. Appl. Note*, pp. 1–42, 2007. [xiii](#), [47](#)
- [11] K.-W. Moon, J.-C. Lee, S.-B. Choe, and K.-H. Shin, “Determination of perpendicular magnetic anisotropy in ultrathin ferromagnetic films by extraordinary hall voltage measurement,” *Review of Scientific Instruments*, vol. 80, no. 11, p. 113904, 2009. [xiii](#), [47](#), [48](#), [50](#)
- [12] T. Kawahara, K. Ito, R. Takemura, and H. Ohno, “Spin-transfer torque ram technology: Review and prospect,” *Microelectronics Reliability*, vol. 52, no. 4, pp. 613–627, 2012. [2](#)
- [13] W. G. Wang, M. Li, S. Hageman, and C. Chien, “Electric-field-assisted switching in magnetic tunnel junctions,” *Nature materials*, vol. 11, no. 1, pp. 64–68, 2012. [2](#)
- [14] T. Nozaki, Y. Shiota, M. Shiraishi, T. Shinjo, and Y. Suzuki, “Voltage-induced perpendicular magnetic anisotropy change in magnetic tunnel junctions,” *Applied Physics Letters*, vol. 96, no. 2, p. 022506, 2010. [2](#)
- [15] S. Tehrani, J. M. Slaughter, M. Deherrera, B. N. Engel, N. D. Rizzo, J. Salter, M. Durlam, R. W. Dave, J. Janesky, B. Butcher, *et al.*, “Magnetoresistive random access memory using magnetic tunnel junctions,” *Proceedings of the IEEE*, vol. 91, no. 5, pp. 703–714, 2003. [2](#)
- [16] S. S. Parkin, M. Hayashi, and L. Thomas, “Magnetic domain-wall racetrack memory,” *Science*, vol. 320, no. 5873, pp. 190–194, 2008. [2](#), [3](#), [19](#), [23](#)
- [17] A. Mardana, S. Ducharme, and S. Adenwalla, “Ferroelectric control of magnetic anisotropy,” *Nano letters*, vol. 11, no. 9, pp. 3862–3867, 2011. [2](#)

-
- [18] J. Heron, M. Trassin, K. Ashraf, M. Gajek, Q. He, S. Yang, D. Nikonov, Y. Chu, S. Salahuddin, and R. Ramesh, “Electric-field-induced magnetization reversal in a ferromagnet-multiferroic heterostructure,” *Physical review letters*, vol. 107, no. 21, p. 217202, 2011. [2](#)
- [19] D. Chiba, M. Sawicki, Y. Nishitani, Y. Nakatani, F. Matsukura, and H. Ohno, “Magnetization vector manipulation by electric fields,” *Nature*, vol. 455, no. 7212, pp. 515–518, 2008. [2](#)
- [20] P. Balestrière, T. Devolder, J.-V. Kim, P. Lecoeur, J. Wunderlich, V. Novák, T. Jungwirth, and C. Chappert, “Fast magnetization switching in gamnas induced by electrical fields,” *Applied Physics Letters*, vol. 99, no. 24, p. 242505, 2011. [2](#)
- [21] N. Lei, T. Devolder, G. Agnus, P. Aubert, L. Daniel, J.-V. Kim, W. Zhao, C. Chappert, D. Ravelosona, and P. Lecoeur, “Electric field control of domain wall logic in piezoelectric/ferromagnetic nanodevices,” *arXiv preprint arXiv:1201.4939*, 2012. [2](#)
- [22] A. Schellekens, A. Van den Brink, J. Franken, H. Swagten, and B. Koopmans, “Electric-field control of domain wall motion in perpendicularly magnetized materials,” *Nature communications*, vol. 3, no. 1, pp. 1–5, 2012. [2](#), [3](#), [20](#), [25](#)
- [23] J.-H. Kim, K.-S. Ryu, J.-W. Jeong, and S.-C. Shin, “Large converse magnetoelectric coupling effect at room temperature in copd/pmn-pt (001) heterostructure,” *Applied Physics Letters*, vol. 97, no. 25, p. 252508, 2010. [2](#), [23](#), [127](#)
- [24] F. Bonell, S. Murakami, Y. Shiota, T. Nozaki, T. Shinjo, and Y. Suzuki, “Large change in perpendicular magnetic anisotropy induced by an electric field in fepd ultrathin films,” *Applied Physics Letters*, vol. 98, no. 23, p. 232510, 2011. [2](#)
- [25] C. Chappert, A. Fert, and F. N. Van Dau, “The emergence of spin electronics in data storage,” in *Nanoscience And Technology: A Collection of Reviews from Nature Journals*, pp. 147–157, World Scientific, 2010. [3](#), [19](#)

REFERENCES

- [26] S.-W. Jung, W. Kim, T.-D. Lee, K.-J. Lee, and H.-W. Lee, “Current-induced domain wall motion in a nanowire with perpendicular magnetic anisotropy,” *Applied Physics Letters*, vol. 92, no. 20, p. 202508, 2008. [3](#)
- [27] O. Boulle, G. Malinowski, and M. Kläui, “Current-induced domain wall motion in nanoscale ferromagnetic elements,” *Materials Science and Engineering: R: Reports*, vol. 72, no. 9, pp. 159–187, 2011. [3](#)
- [28] K. Wang, J. Alzate, and P. K. Amiri, “Low-power non-volatile spintronic memory: Stt-ram and beyond,” *Journal of Physics D: Applied Physics*, vol. 46, no. 7, p. 074003, 2013. [3](#), [20](#)
- [29] J.-M. Hu, Z. Li, L.-Q. Chen, and C.-W. Nan, “High-density magnetoresistive random access memory operating at ultralow voltage at room temperature,” *Nature communications*, vol. 2, no. 1, pp. 1–8, 2011. [3](#)
- [30] P. Shepley, A. Rushforth, M. Wang, G. Burnell, and T. Moore, “Modification of perpendicular magnetic anisotropy and domain wall velocity in pt/co/pt by voltage-induced strain,” *Scientific reports*, vol. 5, no. 1, pp. 1–5, 2015. [3](#), [25](#), [130](#)
- [31] J. M. Coey, *Magnetism and magnetic materials*. Cambridge university press, 2010. [6](#), [8](#), [10](#), [15](#), [18](#), [25](#)
- [32] G. Spavieri and M. Mansuripur, “Origin of the spin–orbit interaction,” *Physica Scripta*, vol. 90, no. 8, p. 085501, 2015. [6](#)
- [33] D. Sander, “The correlation between mechanical stress and magnetic anisotropy in ultrathin films,” *Reports on Progress in Physics*, vol. 62, no. 5, p. 809, 1999. [8](#)
- [34] B. Tudu and A. Tiwari, “Recent developments in perpendicular magnetic anisotropy thin films for data storage applications,” *Vacuum*, vol. 146, pp. 329–341, 2017. [11](#)
- [35] H. Meng and J.-P. Wang, “Spin transfer in nanomagnetic devices with perpendicular anisotropy,” *Applied physics letters*, vol. 88, no. 17, p. 172506, 2006. [11](#)

REFERENCES

- [36] R. Sbiaa, H. Meng, and S. Piramanayagam, “Materials with perpendicular magnetic anisotropy for magnetic random access memory,” *physica status solidi (RRL)–Rapid Research Letters*, vol. 5, no. 12, pp. 413–419, 2011. [11](#)
- [37] S. IKEDA, H. Sato, M. Yamanouchi, H. Gan, K. Miura, K. Mizunuma, S. Kanai, S. Fukami, F. Matsukura, N. Kasai, *et al.*, “Recent progress of perpendicular anisotropy magnetic tunnel junctions for nonvolatile vlsi,” in *Spin*, vol. 2, p. 1240003, World Scientific, 2012. [11](#)
- [38] N. Nakajima, T. Koide, T. Shidara, H. Miyauchi, H. Fukutani, A. Fujimori, K. Iio, T. Katayama, M. Nývlt, and Y. Suzuki, “Perpendicular magnetic anisotropy caused by interfacial hybridization via enhanced orbital moment in co/pt multilayers: Magnetic circular x-ray dichroism study,” *Physical Review Letters*, vol. 81, no. 23, p. 5229, 1998. [11](#), [19](#), [130](#)
- [39] D. Weller, Y. Wu, J. Stöhr, M. Samant, B. Hermsmeier, and C. Chappert, “Orbital magnetic moments of co in multilayers with perpendicular magnetic anisotropy,” *Physical review B*, vol. 49, no. 18, p. 12888, 1994. [11](#)
- [40] D. Weller, J. Stöhr, R. Nakajima, A. Carl, M. Samant, C. Chappert, R. Mégy, P. Beauvillain, P. Veillet, and G. Held, “Microscopic origin of magnetic anisotropy in au/co/au probed with x-ray magnetic circular dichroism,” *Physical Review Letters*, vol. 75, no. 20, p. 3752, 1995. [11](#)
- [41] S. Huang, T. Chen, and C. Chien, “Spin polarization of amorphous cofeb determined by point-contact andreev reflection,” *Applied Physics Letters*, vol. 92, no. 24, p. 242509, 2008. [11](#)
- [42] S. Ikeda, K. Miura, H. Yamamoto, K. Mizunuma, H. Gan, M. Endo, S. Kanai, J. Hayakawa, F. Matsukura, and H. Ohno, “A perpendicular-anisotropy cofeb–mgo magnetic tunnel junction,” *Nature materials*, vol. 9, no. 9, pp. 721–724, 2010. [11](#)
- [43] M. Endo, S. Kanai, S. Ikeda, F. Matsukura, and H. Ohno, “Electric-field effects on thickness dependent magnetic anisotropy of sputtered mgo/co 40 fe 40 b 20/ta structures,” *Applied Physics Letters*, vol. 96, no. 21, p. 212503, 2010. [11](#)

-
- [44] S. Fukami, T. Suzuki, Y. Nakatani, N. Ishiwata, M. Yamanouchi, S. Ikeda, N. Kasai, and H. Ohno, “Current-induced domain wall motion in perpendicularly magnetized c0feb nanowire,” *Applied Physics Letters*, vol. 98, no. 8, p. 082504, 2011. [11](#)
- [45] F. Bloch, “Zur theorie des austauschproblems und der remanenzerscheinung der ferromagnetika,” in *Zur Theorie des Austauschproblems und der Remanenzerscheinung der Ferromagnetika*, pp. 295–335, Springer, 1932. [12](#)
- [46] C. Kooy, “Experimental and theoretical study of the domain configuration in thin layers of bafe₂o₄,” *Philips Res. Repts*, vol. 15, no. 7, 1960. [13](#)
- [47] I. Lemesh, F. Büttner, and G. S. Beach, “Accurate model of the stripe domain phase of perpendicularly magnetized multilayers,” *Physical Review B*, vol. 95, no. 17, p. 174423, 2017. [13](#), [67](#), [80](#), [83](#), [85](#)
- [48] T. Meier, M. Kronseder, and C. Back, “Domain-width model for perpendicularly magnetized systems with dzyaloshinskii-moriya interaction,” *Physical Review B*, vol. 96, no. 14, p. 144408, 2017. [13](#)
- [49] I. Lemesh and G. S. Beach, “Twisted domain walls and skyrmions in perpendicularly magnetized multilayers,” *Physical Review B*, vol. 98, no. 10, p. 104402, 2018. [14](#)
- [50] Q. Wong, W. Gan, F. Luo, G. Lim, C. Ang, F. Tan, W. Law, and W. Lew, “In situ kerr and harmonic measurement in determining current-induced effective fields in mgo/cofeb/ta,” *Journal of Physics D: Applied Physics*, vol. 51, no. 11, p. 115004, 2018. [14](#)
- [51] S. Woo, K. Litzius, B. Krüger, M.-Y. Im, L. Caretta, K. Richter, M. Mann, A. Krone, R. M. Reeve, M. Weigand, *et al.*, “Observation of room-temperature magnetic skyrmions and their current-driven dynamics in ultrathin metallic ferromagnets,” *Nature materials*, vol. 15, no. 5, pp. 501–506, 2016. [14](#), [85](#), [86](#)

-
- [52] S. Woo, K. M. Song, H.-S. Han, M.-S. Jung, M.-Y. Im, K.-S. Lee, K. S. Song, P. Fischer, J.-I. Hong, J. W. Choi, *et al.*, “Spin-orbit torque-driven skyrmion dynamics revealed by time-resolved x-ray microscopy,” *Nature communications*, vol. 8, no. 1, pp. 1–8, 2017. [14](#)
- [53] G. Yu, P. Upadhyaya, Q. Shao, H. Wu, G. Yin, X. Li, C. He, W. Jiang, X. Han, P. K. Amiri, *et al.*, “Room-temperature skyrmion shift device for memory application,” *Nano letters*, vol. 17, no. 1, pp. 261–268, 2017. [14](#)
- [54] W. Legrand, D. Maccariello, F. Ajejas, S. Collin, A. Vecchiola, K. Bouzehouane, N. Reyren, V. Cros, and A. Fert, “Room-temperature stabilization of antiferromagnetic skyrmions in synthetic antiferromagnets,” *Nature materials*, vol. 19, no. 1, pp. 34–42, 2020. [14](#)
- [55] C. Moreau-Luchaire, C. Moutafis, N. Reyren, J. Sampaio, C. Vaz, N. Van Horne, K. Bouzehouane, K. Garcia, C. Deranlot, P. Warnicke, *et al.*, “Additive interfacial chiral interaction in multilayers for stabilization of small individual skyrmions at room temperature,” *Nature nanotechnology*, vol. 11, no. 5, pp. 444–448, 2016. [14](#)
- [56] M. Baćani, M. A. Marioni, J. Schwenk, and H. J. Hug, “How to measure the local dzyaloshinskii-moriya interaction in skyrmion thin-film multilayers,” *Scientific reports*, vol. 9, no. 1, pp. 1–12, 2019. [14](#)
- [57] C. Kittel, P. McEuen, and P. McEuen, *Introduction to solid state physics*, vol. 8. Wiley New York, 1996. [15](#), [16](#), [17](#)
- [58] H. T. Nembach, J. M. Shaw, M. Weiler, E. Jué, and T. J. Silva, “Linear relation between heisenberg exchange and interfacial dzyaloshinskii–moriya interaction in metal films,” *Nature Physics*, vol. 11, no. 10, pp. 825–829, 2015. [17](#), [18](#), [101](#), [117](#)
- [59] J. B. Mohammadi, B. Kardasz, G. Wolf, Y. Chen, M. Pinarbasi, and A. D. Kent, “Reduced exchange interactions in magnetic tunnel junction free layers with insertion layers,” *ACS Applied Electronic Materials*, vol. 1, no. 10, pp. 2025–2029, 2019. [17](#), [18](#), [79](#)

REFERENCES

- [60] W. Heisenberg, “Mehrkörperproblem und resonanz in der quantenmechanik,” *Zeitschrift für Physik*, vol. 38, no. 6-7, pp. 411–426, 1926. [18](#)
- [61] P. A. M. Dirac, “On the theory of quantum mechanics,” *Proceedings of the Royal Society of London. Series A, Containing Papers of a Mathematical and Physical Character*, vol. 112, no. 762, pp. 661–677, 1926. [18](#)
- [62] I. Dzyaloshinsky, “A thermodynamic theory of “weak” ferromagnetism of antiferromagnetics,” *Journal of Physics and Chemistry of Solids*, vol. 4, no. 4, pp. 241–255, 1958. [18](#)
- [63] T. Moriya, “Anisotropic superexchange interaction and weak ferromagnetism,” *Physical review*, vol. 120, no. 1, p. 91, 1960. [18](#)
- [64] M. Uchida, Y. Onose, Y. Matsui, and Y. Tokura, “Real-space observation of helical spin order,” *Science*, vol. 311, no. 5759, pp. 359–361, 2006. [18](#)
- [65] U. K. Roessler, A. Bogdanov, and C. Pfleiderer, “Spontaneous skyrmion ground states in magnetic metals,” *Nature*, vol. 442, no. 7104, pp. 797–801, 2006. [18](#)
- [66] S. Mühlbauer, B. Binz, F. Jonietz, C. Pfleiderer, A. Rosch, A. Neubauer, R. Georgii, and P. Böni, “Skyrmion lattice in a chiral magnet,” *Science*, vol. 323, no. 5916, pp. 915–919, 2009. [18](#)
- [67] X. Yu, Y. Onose, N. Kanazawa, J. Park, J. Han, Y. Matsui, N. Nagaosa, and Y. Tokura, “Real-space observation of a two-dimensional skyrmion crystal,” *Nature*, vol. 465, no. 7300, pp. 901–904, 2010. [18](#)
- [68] A. Fert and P. M. Levy, “Role of anisotropic exchange interactions in determining the properties of spin-glasses,” *Physical review letters*, vol. 44, no. 23, p. 1538, 1980. [18](#), [19](#)
- [69] A. Fert, “Magnetic and transport properties of metallic multilayers,” in *Materials Science Forum*, vol. 59, pp. 439–480, Trans Tech Publ, 1990. [19](#)

REFERENCES

- [70] M. Bode, M. Heide, K. Von Bergmann, P. Ferriani, S. Heinze, G. Bihlmayer, A. Kubetzka, O. Pietzsch, S. Blügel, and R. Wiesendanger, “Chiral magnetic order at surfaces driven by inversion asymmetry,” *Nature*, vol. 447, no. 7141, pp. 190–193, 2007. [19](#)
- [71] S. Meckler, N. Mikuszeit, A. Preßler, E. Vedmedenko, O. Pietzsch, and R. Wiesendanger, “Real-space observation of a right-rotating inhomogeneous cycloidal spin spiral by spin-polarized scanning tunneling microscopy in a triple axes vector magnet,” *Physical review letters*, vol. 103, no. 15, p. 157201, 2009. [19](#)
- [72] G. Chen, J. Zhu, A. Quesada, J. Li, A. N’Diaye, Y. Huo, T. Ma, Y. Chen, H. Kwon, C. Won, *et al.*, “Novel chiral magnetic domain wall structure in fe/ni/cu (001) films,” *Physical review letters*, vol. 110, no. 17, p. 177204, 2013. [19](#)
- [73] H. Schmid, “Multi-ferroic magnetoelectrics,” *Ferroelectrics*, vol. 162, no. 1, pp. 317–338, 1994. [20](#)
- [74] Y. Huai *et al.*, “Spin-transfer torque mram (stt-mram): Challenges and prospects,” *AAPPS bulletin*, vol. 18, no. 6, pp. 33–40, 2008. [20](#)
- [75] K. Lee and S. H. Kang, “Development of embedded stt-mram for mobile system-on-chips,” *IEEE Transactions on Magnetism*, vol. 47, no. 1, pp. 131–136, 2010. [20](#)
- [76] M. Gajek, M. Bibes, S. Fusil, K. Bouzehouane, J. Fontcuberta, A. Barthélémy, and A. Fert, “Multiferroic tunnel junctions,” *arXiv preprint cond-mat/0606444*, 2006. [20](#)
- [77] E. Ascher, H. Rieder, H. Schmid, and H. Stössel, “Some properties of ferromagnetoelectric nickel-iodine boracite, ni₃b₇o₁₃i,” *Journal of Applied Physics*, vol. 37, no. 3, pp. 1404–1405, 1966. [20](#)
- [78] H. Schmid, “On a magnetoelectric classification of materials,” *International Journal of Magnetism*, vol. 4, no. 4, pp. 337–361, 1973. [20](#)

-
- [79] D. Damjanovic, “Ferroelectric, dielectric and piezoelectric properties of ferroelectric thin films and ceramics,” *Reports on Progress in Physics*, vol. 61, no. 9, p. 1267, 1998. [21](#)
- [80] M. Lines and A. Glass, “Chap. 3,” 1979. [21](#)
- [81] R. Vasudevan, S. Jesse, Y. Kim, A. Kumar, and S. Kalinin, “Spectroscopic imaging in piezoresponse force microscopy: New opportunities for studying polarization dynamics in ferroelectrics and multiferroics,” *Mrs Communications*, vol. 2, no. 3, pp. 61–73, 2012. [21](#), [28](#)
- [82] R. Ramesh and N. A. Spaldin, “Multiferroics: progress and prospects in thin films,” *Nanoscience And Technology: A Collection of Reviews from Nature Journals*, pp. 20–28, 2010. [22](#)
- [83] C. A. Vaz, “Electric field control of magnetism in multiferroic heterostructures,” *Journal of Physics: Condensed Matter*, vol. 24, no. 33, p. 333201, 2012. [22](#)
- [84] R. Streubel, D. Köhler, R. Schäfer, and L. M. Eng, “Strain-mediated elastic coupling in magnetoelectric nickel/barium-titanate heterostructures,” *Physical Review B*, vol. 87, no. 5, p. 054410, 2013. [22](#), [29](#)
- [85] T. H. Lahtinen, K. J. Franke, and S. Van Dijken, “Electric-field control of magnetic domain wall motion and local magnetization reversal,” *Scientific reports*, vol. 2, p. 258, 2012. [22](#), [114](#)
- [86] D. Parkes, L. Shelford, P. Wadley, V. Holý, M. Wang, A. Hindmarch, G. Van Der Laan, R. P. Campion, K. Edmonds, S. Cavill, *et al.*, “Magnetostrictive thin films for microwave spintronics,” *Scientific reports*, vol. 3, p. 2220, 2013. [23](#)
- [87] T. Brintlinger, S.-H. Lim, K. H. Baloch, P. Alexander, Y. Qi, J. Barry, J. Melngailis, L. Salamanca-Riba, I. Takeuchi, and J. Cumings, “In situ observation of reversible nanomagnetic switching induced by electric fields,” *Nano letters*, vol. 10, no. 4, pp. 1219–1223, 2010. [23](#)

-
- [88] N. Lei, T. Devolder, G. Agnus, P. Aubert, L. Daniel, J.-V. Kim, W. Zhao, T. Trypiniotis, R. P. Cowburn, C. Chappert, *et al.*, “Strain-controlled magnetic domain wall propagation in hybrid piezoelectric/ferromagnetic structures,” *Nature communications*, vol. 4, no. 1, pp. 1–7, 2013. [23](#)
- [89] V. Novosad, Y. Otani, A. Ohsawa, S. Kim, K. Fukamichi, J. Koike, K. Maruyama, O. Kitakami, and Y. Shimada, “Novel magnetostrictive memory device,” *Journal of applied physics*, vol. 87, no. 9, pp. 6400–6402, 2000. [23](#)
- [90] M. Buzzi, R. V. Chopdekar, J. L. Hockel, A. Bur, T. Wu, N. Pilet, P. Warnicke, G. P. Carman, L. J. Heyderman, and F. Nolting, “Single domain spin manipulation by electric fields in strain coupled artificial multiferroic nanostructures,” *Physical review letters*, vol. 111, no. 2, p. 027204, 2013. [23](#)
- [91] C. Zhang, T. Ma, and M. Yan, “Induced additional anisotropy influences on magnetostriction of giant magnetostrictive materials,” *Journal of Applied Physics*, vol. 112, no. 10, p. 103908, 2012. [23](#)
- [92] T. Wu, A. Bur, P. Zhao, K. P. Mohanchandra, K. Wong, K. L. Wang, C. S. Lynch, and G. P. Carman, “Giant electric-field-induced reversible and permanent magnetization reorientation on magnetoelectric ni/(011)[pb (mg 1/3 nb 2/3) o 3](1-x)–[pbtio 3] x heterostructure,” *Applied Physics Letters*, vol. 98, no. 1, p. 012504, 2011. [23](#)
- [93] E. De Ranieri, P. Roy, D. Fang, E. Vehstedt, A. Irvine, D. Heiss, A. Casiraghi, R. Campion, B. Gallagher, T. Jungwirth, *et al.*, “Piezoelectric control of the mobility of a domain wall driven by adiabatic and non-adiabatic torques,” *Nature materials*, vol. 12, no. 9, pp. 808–814, 2013. [24](#), [31](#)
- [94] R. P. del Real, V. Raposo, E. Martinez, and M. Hayashi, “Current-induced generation and synchronous motion of highly packed coupled chiral domain walls,” *Nano Letters*, vol. 17, no. 3, pp. 1814–1818, 2017. [25](#)

-
- [95] P. G. Gowtham, G. M. Stiehl, D. C. Ralph, and R. A. Buhrman, “Thickness-dependent magnetoelasticity and its effects on perpendicular magnetic anisotropy in ta/cofeb/mgo thin films,” *Physical Review B*, vol. 93, no. 2, p. 024404, 2016. [26](#)
- [96] C. Kittel, “Physical theory of ferromagnetic domains,” *Reviews of modern Physics*, vol. 21, no. 4, p. 541, 1949. [27](#)
- [97] J. Fousek, “Ferroelectric domains: some recent advances,” in *Ferroelectric Ceramics*, pp. 87–105, Springer, 1993. [27](#)
- [98] A. Vlooswijk, B. Noheda, G. Catalan, A. Janssens, B. Barcones, G. Rijnders, D. Blank, S. Venkatesan, B. Kooi, and J. De Hosson, “Smallest 90 domains in epitaxial ferroelectric films,” *Applied physics letters*, vol. 91, no. 11, p. 112901, 2007. [27](#)
- [99] P. W. Forsbergh Jr, “Domain structures and phase transitions in barium titanate,” *Physical Review*, vol. 76, no. 8, p. 1187, 1949. [27](#)
- [100] I. Luk’yanchuk, A. Schilling, J. Gregg, G. Catalan, and J. Scott, “Origin of ferroelastic domains in free-standing single-crystal ferroelectric films,” *Physical Review B*, vol. 79, no. 14, p. 144111, 2009. [27](#)
- [101] V. Garcia, M. Bibes, and A. Barthélémy, “Artificial multiferroic heterostructures for an electric control of magnetic properties,” *Comptes Rendus Physique*, vol. 16, no. 2, pp. 168–181, 2015. [28](#), [29](#)
- [102] D. Dale, A. Fleet, J. Brock, and Y. Suzuki, “Dynamically tuning properties of epitaxial colossal magnetoresistance thin films,” *Applied physics letters*, vol. 82, no. 21, pp. 3725–3727, 2003. [28](#)
- [103] C. Vaz, F. Walker, C. Ahn, and S. Ismail-Beigi, “Intrinsic interfacial phenomena in manganite heterostructures,” *Journal of Physics: Condensed Matter*, vol. 27, no. 12, p. 123001, 2015. [28](#)
- [104] S. Geprägs, A. Brandlmaier, M. Opel, R. Gross, and S. Goennenwein, “Electric field controlled manipulation of the magnetization in ni/batio 3 hybrid structures,” *Applied Physics Letters*, vol. 96, no. 14, p. 142509, 2010. [28](#)

REFERENCES

- [105] S. Geprägs, D. Mannix, M. Opel, S. T. Goennenwein, and R. Gross, “Converse magnetoelectric effects in $\text{Fe}_3\text{O}_4/\text{BaTiO}_3$ multiferroic hybrids,” *Physical Review B*, vol. 88, no. 5, p. 054412, 2013. [28](#)
- [106] S. T. Goennenwein, “Voltage-controlled spin mechanics,” *Europhysics News*, vol. 41, no. 4, pp. 17–20, 2010. [28](#)
- [107] S. Sahoo, S. Polisetty, C.-G. Duan, S. S. Jaswal, E. Y. Tsymlal, and C. Binek, “Ferroelectric control of magnetism in BaTiO_3/Fe heterostructures via interface strain coupling,” *Physical Review B*, vol. 76, no. 9, p. 092108, 2007. [28](#), [29](#)
- [108] G. Venkataiah, E. Wada, H. Taniguchi, M. Itoh, and T. Taniyama, “Electric-voltage control of magnetism in Fe/BaTiO_3 heterostructured multiferroics,” *Journal of Applied Physics*, vol. 113, no. 17, p. 17C701, 2013. [28](#)
- [109] C. A. Vaz, J. Hoffman, C. H. Ahn, and R. Ramesh, “Magnetoelectric coupling effects in multiferroic complex oxide composite structures,” *Advanced Materials*, vol. 22, no. 26-27, pp. 2900–2918, 2010. [29](#)
- [110] S. Geprägs, M. Opel, S. T. Goennenwein, and R. Gross, “Giant magnetoelastic effects in BaTiO_3 -based extrinsic multiferroic hybrids,” *Physical Review B*, vol. 86, no. 13, p. 134432, 2012. [29](#)
- [111] G. Venkataiah, Y. Shirahata, M. Itoh, and T. Taniyama, “Manipulation of magnetic coercivity of Fe film in Fe/BaTiO_3 heterostructure by electric field,” *Applied Physics Letters*, vol. 99, no. 10, p. 102506, 2011. [29](#)
- [112] R. Chopdekar and Y. Suzuki, “Magnetoelectric coupling in epitaxial CoFe_2O_4 on BaTiO_3 ,” *Applied physics letters*, vol. 89, no. 18, p. 182506, 2006. [29](#)
- [113] Y. Shirahata, T. Nozaki, G. Venkataiah, H. Taniguchi, M. Itoh, and T. Taniyama, “Switching of the symmetry of magnetic anisotropy in Fe/BaTiO_3 heterostructures,” *Applied Physics Letters*, vol. 99, no. 2, p. 022501, 2011. [29](#)

-
- [114] G. Venkataiah, Y. Shirahata, I. Suzuki, M. Itoh, and T. Taniyama, “Strain-induced reversible and irreversible magnetization switching in fe/batio3 heterostructures,” *Journal of Applied Physics*, vol. 111, no. 3, p. 033921, 2012. [29](#)
- [115] M. Ghidini, F. Maccherozzi, X. Moya, L. C. Phillips, W. Yan, J. Soussi, N. Métallier, M. E. Vickers, N.-J. Steinke, R. Mansell, *et al.*, “Perpendicular local magnetization under voltage control in ni films on ferroelectric batio3 substrates,” *Advanced Materials*, vol. 27, no. 8, pp. 1460–1465, 2015. [29](#)
- [116] F. Brandl, K. Franke, T. Lahtinen, S. van Dijken, and D. Grundler, “Spin waves in cofeb on ferroelectric domains combining spin mechanics and magnonics,” *Solid state communications*, vol. 198, pp. 13–17, 2014. [29](#)
- [117] S. W. Fackler, M. J. Donahue, T. Gao, P. N. Nero, S.-W. Cheong, J. Cummings, and I. Takeuchi, “Local control of magnetic anisotropy in transcritical permalloy thin films using ferroelectric batio3 domains,” *Applied Physics Letters*, vol. 105, no. 21, p. 212905, 2014. [29](#)
- [118] M. Liu, S. Li, O. Obi, J. Lou, S. Rand, and N. X. Sun, “Electric field modulation of magnetoresistance in multiferroic heterostructures for ultralow power electronics,” *Applied Physics Letters*, vol. 98, no. 22, p. 222509, 2011. [31](#)
- [119] R. Cherifi, V. Ivanovskaya, L. Phillips, A. Zobelli, I. Infante, E. Jacquet, V. Garcia, S. Fusil, P. Briddon, N. Guiblin, *et al.*, “Electric-field control of magnetic order above room temperature,” *Nature materials*, vol. 13, no. 4, pp. 345–351, 2014. [31](#)
- [120] E. Williams, “An introduction to sputtering of magnetic and magneto-optic thin films for data recording,” *Journal of magnetism and magnetic materials*, vol. 95, no. 3, pp. 356–364, 1991. [32](#)
- [121] J. Kerr and E. London, “Dublin philos. mag,” *J. Sci*, vol. 5, no. 30, pp. 161–177, 1878. [36](#)

REFERENCES

- [122] A. Hubert and R. Schäfer, *Magnetic domains: the analysis of magnetic microstructures*. Springer Science & Business Media, 2008. 36, 38
- [123] P. Kasiraj, R. Shelby, J. Best, and D. Horne, “Magnetic domain imaging with a scanning kerr effect microscope,” *IEEE Transactions on Magnetics*, vol. 22, no. 5, pp. 837–839, 1986. 39
- [124] T. Nozaki, R. Imai, M. Tanbo, R. Nagashima, S. Tamura, T. Tani, Y. Joti, M. Tomita, K. Hibino, M. T. Kanemaki, *et al.*, “Dynamic organization of chromatin domains revealed by super-resolution live-cell imaging,” *Molecular cell*, vol. 67, no. 2, pp. 282–293, 2017. 42
- [125] R. Fagaly, “Superconducting quantum interference device instruments and applications,” *Review of scientific instruments*, vol. 77, no. 10, p. 101101, 2006. 46
- [126] E. H. Hall *et al.*, “On a new action of the magnet on electric currents,” *American Journal of Mathematics*, vol. 2, no. 3, pp. 287–292, 1879. 49
- [127] T. Miyasato, N. Abe, T. Fujii, A. Asamitsu, S. Onoda, Y. Onose, N. Nagaosa, and Y. Tokura, “Crossover behavior of the anomalous hall effect and anomalous nernst effect in itinerant ferromagnets,” *Physical review letters*, vol. 99, no. 8, p. 086602, 2007. 49
- [128] D. Rosenblatt, M. Karpovskii, and A. Gerber, “Monitoring magnetization reversal and perpendicular anisotropy by the extraordinary hall effect and anisotropic magnetoresistance,” *Journal of Applied Physics*, vol. 108, no. 4, p. 043924, 2010. 50
- [129] T. Ikeda, *Fundamentals of piezoelectricity*. Oxford university press, 1996. 52
- [130] G. Kuczynski, “Effect of elastic strain on the electrical resistance of metals,” *Physical review*, vol. 94, no. 1, p. 61, 1954. 55

REFERENCES

- [131] D. Wang, C. Nordman, Z. Qian, J. M. Daughton, and J. Myers, “Magnetostriction effect of amorphous cofeb thin films and application in spin-dependent tunnel junctions,” *Journal of applied physics*, vol. 97, no. 10, p. 10C906, 2005. [56](#)
- [132] A. Fert, V. Cros, and J. Sampaio, “Skyrmions on the track,” *Nature nanotechnology*, vol. 8, no. 3, pp. 152–156, 2013. [60](#)
- [133] G. Giannopoulos, R. Salikhov, B. Zingsem, A. Markou, I. Panagiotopoulos, V. Psycharis, M. Farle, and D. Niarchos, “Large magnetic anisotropy in strained fe/co multilayers on auctu and the effect of carbon doping,” *APL Materials*, vol. 3, no. 4, p. 041103, 2015. [61](#)
- [134] T. Osaka, T. Homma, K. Saito, A. Takekoshi, Y. Yamazaki, and T. Namikawa, “Co-based soft magnetic films produced by electroless deposition,” *Journal of the Electrochemical Society*, vol. 139, no. 5, p. 1311, 1992. [62](#)
- [135] C.-J. Lin, G. Gorman, C. Lee, R. Farrow, E. Marinero, H. Do, H. Notarys, and C. Chien, “Magnetic and structural properties of co/pt multilayers,” *Journal of Magnetism and Magnetic Materials*, vol. 93, pp. 194–206, 1991. [64](#)
- [136] J. Qiu, Z. Meng, Y. Yang, J. F. Ying, Q. J. Yap, and G. Han, “Effect of roughness on perpendicular magnetic anisotropy in (co₉₀fe₁₀/pt) *n* superlattices,” *AIP Advances*, vol. 6, no. 5, p. 056123, 2016. [64](#), [76](#), [77](#), [124](#)
- [137] J.-H. Park, C. Park, T. Jeong, M. T. Moneck, N. T. Nufer, and J.-G. Zhu, “Co/ pt multilayer based magnetic tunnel junctions using perpendicular magnetic anisotropy,” *Journal of Applied Physics*, vol. 103, no. 7, p. 07A917, 2008. [65](#)
- [138] M. Anhalt, “Systematic investigation of particle size dependence of magnetic properties in soft magnetic composites,” *Journal of Magnetism and Magnetic Materials*, vol. 320, no. 14, pp. e366–e369, 2008. [65](#), [81](#)

REFERENCES

- [139] P. Agrawal, F. Büttner, I. Lemesh, S. Schlotter, and G. S. Beach, “Measurement of interfacial dzyaloshinskii-moriya interaction from static domain imaging,” *Physical Review B*, vol. 100, no. 10, p. 104430, 2019. [66](#), [67](#), [80](#), [85](#), [86](#), [93](#), [108](#)
- [140] E. W. Lee, “Magnetostriction and magnetomechanical effects,” *Reports on progress in physics*, vol. 18, no. 1, p. 184, 1955. [71](#), [124](#)
- [141] H. Ishibashi, K. Harada, M. Kogachi, and S. Noguchi, “Magnetic properties and long range order parameter in b2-type coFe alloys,” *Journal of magnetism and magnetic materials*, vol. 272, pp. 774–775, 2004. [74](#)
- [142] A. Rozatian, C. Marrows, T. Hase, and B. Tanner, “The relationship between interface structure, conformality and perpendicular anisotropy in copd multilayers,” *Journal of Physics: Condensed Matter*, vol. 17, no. 25, p. 3759, 2005. [76](#)
- [143] R. Moreno, R. Evans, S. Khmelevskyi, M. Muñoz, R. Chantrell, and O. Chubykalo-Fesenko, “Temperature-dependent exchange stiffness and domain wall width in co,” *Physical Review B*, vol. 94, no. 10, p. 104433, 2016. [78](#), [90](#), [92](#), [100](#), [105](#), [107](#), [108](#), [116](#)
- [144] K. Zeissler, M. Mruczkiewicz, S. Finizio, J. Raabe, P. Shepley, A. Sadovnikov, S. Nikitov, K. Fallon, S. McFadzean, S. McVitie, *et al.*, “Pinning and hysteresis in the field dependent diameter evolution of skyrmions in pt/co/ir superlattice stacks,” *Scientific reports*, vol. 7, no. 1, pp. 1–9, 2017. [78](#)
- [145] Y. Zhou, R. Mansell, S. Valencia, F. Kronast, and S. van Dijken, “Temperature dependence of the dzyaloshinskii-moriya interaction in ultrathin films,” *Physical Review B*, vol. 101, no. 5, p. 054433, 2020. [79](#), [101](#), [117](#)
- [146] C. Eylich, A. Zamani, W. Huttema, M. Arora, D. Harrison, F. Rashidi, D. Broun, B. Heinrich, O. Mryasov, M. Ahlberg, *et al.*, “Effects of substitution on the exchange stiffness and magnetization of co films,” *Physical Review B*, vol. 90, no. 23, p. 235408, 2014. [79](#)

-
- [147] S. T. Lim, M. Tran, J. W. Chenchen, J. F. Ying, and G. Han, “Effect of different seed layers with varying co and pt thicknesses on the magnetic properties of co/pt multilayers,” *Journal of Applied Physics*, vol. 117, no. 17, p. 17A731, 2015. [79](#)
- [148] K. Toyoki, T. Nishimura, S. Harimoto, Y. Shiratsuchi, and R. Nakatani, “Magnetic domain wall energy in ni/co superlattices,” *Journal of magnetism and magnetic materials*, vol. 372, pp. 41–46, 2014. [84](#)
- [149] Y. Ishikuro, M. Kawaguchi, N. Kato, Y.-C. Lau, and M. Hayashi, “Dzyaloshinskii-moriya interaction and spin-orbit torque at the ir/co interface,” *Physical Review B*, vol. 99, no. 13, p. 134421, 2019. [85](#), [97](#)
- [150] Y. Chen, Q. Zhang, J. Jia, Y. Zheng, Y. Wang, X. Fan, and J. Cao, “Tuning slonczewski-like torque and dzyaloshinskii–moriya interaction by inserting a pt spacer layer in ta/cofeb/mgo structures,” *Applied Physics Letters*, vol. 112, no. 23, p. 232402, 2018. [86](#)
- [151] A. Thiaville, S. Rohart, É. Jué, V. Cros, and A. Fert, “Dynamics of dzyaloshinskii domain walls in ultrathin magnetic films,” *EPL (Europhysics Letters)*, vol. 100, no. 5, p. 57002, 2012. [86](#), [97](#), [111](#)
- [152] J. Lucassen, M. J. Meijer, O. Kurnosikov, H. J. Swagten, B. Koopmans, R. Lavrijsen, F. Kloodt-Twesten, R. Frömter, and R. A. Duine, “Tuning magnetic chirality by dipolar interactions,” *Physical review letters*, vol. 123, no. 15, p. 157201, 2019. [86](#), [98](#), [112](#)
- [153] S. Meyer, B. Dupé, P. Ferriani, and S. Heinze, “Dzyaloshinskii-moriya interaction at an antiferromagnetic interface: First-principles study of fe/ir bilayers on rh (001),” *Physical Review B*, vol. 96, no. 9, p. 094408, 2017. [86](#)
- [154] A. Belabbes, G. Bihlmayer, S. Blügel, and A. Manchon, “Oxygen-enabled control of dzyaloshinskii-moriya interaction in ultra-thin magnetic films,” *Scientific Reports*, vol. 6, no. 1, pp. 1–9, 2016. [86](#)

-
- [155] M. Hoffmann, J. Weischenberg, B. Dupé, F. Freimuth, P. Ferriani, Y. Mokrousov, and S. Heinze, “Topological orbital magnetization and emergent hall effect of an atomic-scale spin lattice at a surface,” *Physical Review B*, vol. 92, no. 2, p. 020401, 2015. [86](#)
- [156] K. Shahbazi, J.-V. Kim, H. T. Nembach, J. M. Shaw, A. Bischof, M. D. Rossell, V. Jeudy, T. A. Moore, and C. H. Marrows, “Domain-wall motion and interfacial dzyaloshinskii-moriya interactions in pt/co/ir (t ir)/ta multilayers,” *Physical Review B*, vol. 99, no. 9, p. 094409, 2019. [90](#), [105](#)
- [157] M. Belmeguenai, H. Bouloussa, Y. Roussigné, M. Gabor, T. Petrisor Jr, C. Tiusan, H. Yang, A. Stashkevich, and S. Chérif, “Interface dzyaloshinskii-moriya interaction in the interlayer antiferromagnetic-exchange coupled pt/cofeb/ru/cofeb systems,” *Physical Review B*, vol. 96, no. 14, p. 144402, 2017. [92](#)
- [158] C. Kittel and C.-y. Fong, *Quantum theory of solids*, vol. 5. Wiley New York, 1963. [92](#), [108](#)
- [159] R. Bastardis, U. Atxitia, O. Chubykalo-Fesenko, and H. Kachkachi, “Unified decoupling scheme for exchange and anisotropy contributions and temperature-dependent spectral properties of anisotropic spin systems,” *Physical Review B*, vol. 86, no. 9, p. 094415, 2012. [93](#), [100](#), [108](#), [116](#)
- [160] H. B. Callen and E. Callen, “The present status of the temperature dependence of magnetocrystalline anisotropy, and the $1/(1 + T)^2$ power law,” *Journal of Physics and Chemistry of Solids*, vol. 27, no. 8, pp. 1271–1285, 1966. [98](#)
- [161] U. Atxitia, D. Hinzke, O. Chubykalo-Fesenko, U. Nowak, H. Kachkachi, O. N. Mryasov, R. Evans, and R. W. Chantrell, “Multiscale modeling of magnetic materials: Temperature dependence of the exchange stiffness,” *Physical Review B*, vol. 82, no. 13, p. 134440, 2010. [100](#), [116](#)
- [162] S. Schlotter, P. Agrawal, and G. S. Beach, “Temperature dependence of the dzyaloshinskii-moriya interaction in pt/co/cu thin film heterostructures,” *Applied Physics Letters*, vol. 113, no. 9, p. 092402, 2018. [101](#)

REFERENCES

- [163] J.-W. Lee, S.-C. Shin, and S.-K. Kim, “Spin engineering of copd alloy films via the inverse piezoelectric effect,” *Applied physics letters*, vol. 82, no. 15, pp. 2458–2460, 2003. [127](#)
- [164] N. Lei, S. Park, P. Lecoeur, D. Ravelosona, C. Chappert, O. Stelmakhovych, and V. Holý, “Magnetization reversal assisted by the inverse piezoelectric effect in co-fe-b/ferroelectric multilayers,” *Physical Review B*, vol. 84, no. 1, p. 012404, 2011. [127](#)
- [165] S. Hashimoto, Y. Ochiai, and K. Aso, “Perpendicular magnetic anisotropy and magnetostriction of sputtered co/pd and co/pt multilayered films,” *Journal of applied physics*, vol. 66, no. 10, pp. 4909–4916, 1989. [127](#), [128](#), [130](#)
- [166] Y.-T. Chen, S. Jen, Y. Yao, J.-M. Wu, and A.-C. Sun, “Interfacial effects on magnetostriction of co fe b/ al o x/ co junction,” *Applied physics letters*, vol. 88, no. 22, p. 222509, 2006. [130](#)
- [167] J. Aboaf, S. Herd, and E. Klokholm, “Magnetic properties and structure of cobalt-platinum thin films,” *IEEE transactions on magnetics*, vol. 19, no. 4, pp. 1514–1519, 1983. [130](#)
- [number]natbib